Modeling the cometary environment using a fluid approach

by

Yinsi Shou

A dissertation submitted in partial fulfillment
of the requirements for the degree of
Doctor of Philosophy
(Atmospheric, Oceanic and Space Sciences)
in The University of Michigan
2017

Doctoral Committee:

Research Professor Michael Combi, Chair
Professor Tamas Gombosi
Associate Professor Xianzhe Jia
Professor Kenneth Powell
Research Professor Gabor Tóth

ACKNOWLEDGEMENTS

I would like to thank my dissertation committee chair and academic advisor Research Professor Michael R. Combi for his continuous guidance and support, without which I would not have been able to complete this thesis. I am also grateful for the experience of working with him on a topic that is both interesting and challenging. In the process, I not only learned how to work as a scientist, but also experienced the uncertainties and the frustrations scientists have to face. I am sure the valuable experience can benefit me in the future, whether in career or in life. In addition, I would also like to thank him for generously supporting me to attend many academic conferences.

I would like to thank my dissertation committee Research Professor Michael R. Combi (chair), Professor Tamas I. Gombosi, Associate Professor Xianzhe Jia, Professor Kenneth Powell, and Research Professor Gabor Toth for their knowledge and advice that significantly improved this thesis.

I would like to express my gratitude to Research Professor Gabor Toth for his expert support with the code development and the numerical simulations, without which the thesis would not have been possible. I would also like to thank Dr. Martin Rubin, Dr. Kenneth Hansen, Dr. Zhenguang Huang and Yuxi Chen for their help, valuable discussions and collaboration.

TABLE OF CONTENTS

LIST OF FIGURES

Figure

LIST OF TABLES

Table

ABSTRACT

Modeling the complicated cometary environment using a fluid approach

by

Yinsi Shou

Chair: Michael Combi

Comets are believed to have preserved the building material of the early solar system and to hold clues to the origin of life on Earth. Abundant remote observations of comets by telescopes and the in-situ measurements by a handful of space missions reveal that the cometary environments are complicated by various physical and chemical processes among the neutral gases and dust grains released from comets, cometary ions, and the solar wind in the interplanetary space. Therefore, physics-based numerical models are in demand to interpret the observational data and to deepen our understanding of the cometary environment.

In this thesis, three models using a fluid approach, which include important physical and chemical processes underlying the cometary environment, have been developed to study the plasma, neutral gas, and the dust grains, respectively. Although models based on the fluid approach have limitations in capturing all of the correct physics for certain applications, especially for very low gas density environment, they are computationally much more efficient than alternatives. In the simulations of comet 67P/Churyumov-Gerasimenko at various heliocentric distances with a wide range of production rates, our multi-fluid cometary neutral gas model and multi-fluid cometary

dust model have achieved comparable results to the Direct Simulation Monte Carlo (DSMC) model, which is based on a kinetic approach that is valid in all collisional regimes. Therefore, our model is a powerful alternative to the particle-based model, especially for some computationally intensive simulations.

Capable of accounting for the varying heating efficiency under various physical conditions in a self-consistent way, the multi-fluid cometary neutral gas model is a good tool to study the dynamics of the cometary coma with different production rates and heliocentric distances. The modeled H_2O expansion speeds reproduce the general trend and the speed's nonlinear dependencies of production rate and heliocentric distance, which are found in remote observations.

In the multi-fluid dust model, we use a newly developed numerical mesh to resolve the real shaped nucleus in the center and to facilitate prescription of the outer boundary conditions that accommodate the rotating frame. The model studies the effects of the rotating nucleus and the cometary activity in time-dependent simulations for the first time. The result also suggests that the rotation of the nucleus explains why there is no clear dust speed dependence on size in some of the dust observations.

We developed a new multi-species comet MHD model to simulate the plasma environment of comet C/2006 P1 (McNaught) over a wide range of heliocentric distances from 0.17 AU to 1.75 AU, with the constraints provided by remote and in situ observations. Typical subsolar standoff distances of bow shock and contact surface are modeled and presented to characterize the solar wind interaction of the comet at various heliocentric distances. In addition, the model is also the first one to be used to study the composition and dynamics in the distant cometary tail. The results agree well with the measured water group ion abundances from the Ulysses/SWICS 1.7 AU down-tail from the comet and the velocity and temperature measured by Ulysses/SWOOPS.

CHAPTER I

Introduction

Comets are fascinating planetary objects that have been observed since ancient times. Featured by their bright heads and tails, they can be observed with the naked eye and easily stands out from numerous planets and stars in the night sky. In addition to the amazing and mysterious natural phenomena, comets may also provide the clues to the most fundamental questions in planetary science: How did the solar system and planets form and what is the origin of pre-biotic chemistry?

The importance of comets lies in their formation around 4.5 billion years ago when the solar system was formed. Though several hypotheses exist on the origin of the formation of comets, it is widely believed to that they were formed at the same time and from the same material as our solar system. But unlike other planets, the sizes of comets, most of which are less than 50 km in radius, prevent them from undergoing the geological processes that can greatly alter the composition and the structure of a planet. In addition, they have remained far away from the Sun for most of the time, so the solar radiation should only affect the cometary material within the first few meters from their surfaces. Therefore, they are regarded as fossils, which preserved the primordial building material of our solar system.

Most of comets originate from two reservoirs in the solar system: The Kuiper belt and the Oort cloud. Fig. 1.1 shows a schematic of the Kuiper belt and the Oort

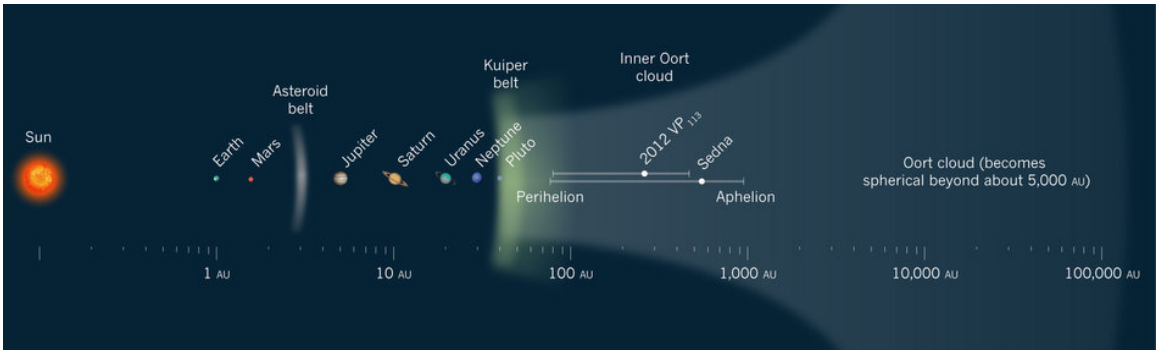

Figure 1.1: A schematic showing the locations of the Kuiper belt and the Oort cloud in solar system from *Schwamb* (2014).

cloud. The Kuiper belt is a torus extending from Neptune's orbit at 30 AU to about 50 AU and is the home to the short period comets. Once their orbits are perturbed into the inner solar system they have periods less than 20 years, and inclinations lower than 30 degrees. The Oort cloud is shell at approximately 50000 AU from the Sun, populated with long period comets, whose periods are longer than 200 years and whose orientations are random. In these two reservoirs reside numerous comets. The estimated population for the Oort cloud is on the order of trillions.

Perturbed by other planets or stars, a comet can get kicked out from the reservoir and start its journey to the inner solar system. In the beginning, the comet may not be active and is not outgassing just like an asteroid. As it gets closer than about 3 AU to the Sun, the surface of the "dirty snowball" (*Whipple*, 1950) is heated by the solar radiation. Once the surface temperature exceeds the sublimation temperature of a certain volatile, the volatile, for example CO, begins sublimating and the comet starts outgassing. As the surface temperature gets higher, more volatiles can begin outgassing from the nucleus, resulting in a cometary atmosphere, which is also called the coma. Because of the lack of a significant gravitational force, the size of a coma can reach several million kilometers. In addition, the coma is able to absorb solar photons and emit photons itself. A large coma and a relatively high brightness allow a comet to distinguish itself from an asteroid, which also enables the detection of

comets by the naked eye and telescopes.

Atoms and molecules in the coma are subject to various other interactions with the sun. The solar photon flux can exert a radiation pressure force on the hydrogen coma and accelerate the atoms and molecules, resulting in a prolonged neutral coma envelope in the anti-sunward direction. Induced by solar photons, photo-chemical reactions are able to alter the coma composition and deposit energy in the coma. One typical example is the dissociation of H_2O into one OH radical and one H atom. In the meantime, the energy carried by the photon is transformed into the kinetic energy of the photo-dissociation products.

In addition to photo-dissociation, photo-ionization transforms neutral molecules and atoms into various ions, which again have to interact with the solar wind, the magnetized ion flow from the sun. The solar wind mainly consists of protons and electrons and carries the magnetic fields of the sun, which varies continuously depending on the activity on the Sun and the location of the solar wind. The interaction between the expanding cometary coma and the incoming solar wind leads to a unique cometary plasma environment and many interesting physical phenomenon, such as the cometary plasma tails. As the solar wind flows toward the comet, the cometary ions act as an obstacle, slowing the solar wind and bending the magnetic field. The resulting magnetic field lines are draped around the obstacle, with the ends of the lines pointing away from the sun, creating a channel for the solar wind ions and cometary ions to leave the comet. As some emission lines of H_2O^+ and CO^+ are at the visible wavelengths, a plasma tail pointing away from the sun can be seen. If the tail is dominated by H_2O^+, it appears more reddish; if there are more CO^+ ions, a more blue tail can be seen. The existence of the solar wind was predicted based on the cometary plasma tails before the space era (*Biermann*, 1951).

As the "dirty snowball" approaches the sun, strong gas sublimation is able to drag the dust grains into space, which are greatly affected by the gravity of the sun. As

they may also contain refractories, a dust tail, which is distinct from the plasma tail sometimes can be observed by the naked eye. Because dust grains are also believed to hold clues to the origin of the solar system, spectroscopic observations have been made to measure the composition of dust grains and their production rates. So far silicates of iron and magnesium and some other organic material have been detected. Dust grains may also have an impact on the neutral coma and the cometary plasma environment. The dust drag force can slow down the gas expansion, if a significant amount of dust grains are present. Some dust grains made of water ice can form an extended source, which sublimates at a higher temperature than the temperature of the expanding coma and thus heats the coma. The dust grains can get charged as well as a result of photochemistry and are subject to interaction with the electromagnetic force there. Considering their porous surface, dust grains may get many electrons attached and become a major charge carrier in the cometary plasma environment, creating a fascinating laboratory to study topics related to dusty-plasma problems.

Due to the tremendous reservoir of comets, at least two or three comets can be observed by ground-based telescopes annually. The composition, expansion speed, isotopic abundances of the coma and the dust grains can be readily obtained, which enables taxonomy based on these parameters. These kinds of taxonomy may characterize comets with different origins and may also provide clues to the history of the evolution of comets and the solar system. In addition, occasional emergences of special comets also appeal to researchers and general public. Comet Hale-Bopp is one of the brightest comets in many decades and was visible to the naked eye for a record 18 months. It was so big and bright that the observations were made from a large heliocentric distance to perihelion, facilitating the monitoring of the evolution of coma and detections of previously unknown compositions. Comets traveling very close to the sun and other planets, such as Comet ISON and Comet Shoemaker-Levy 9 may also offer opportunities to study not only comet but also the atmosphere of

the Sun and other planets.

In addition to plenty of observations by ground-based telescopes, several space missions and observational campaigns have deepened our knowledge of comets in many aspects. In 1986, several spacecrafts, i.e. VEGA1, VEGA2, Susei, Giotto, Sakigake and International Cometary Explorer, made their visits to Comet Halley and measured the neutral gases, the ions and the magnetic fields at different region of the cometary environment. Giotto obtained the images of the cometary nucleus from a distance of less than 600 km, which showed the nucleus shape and the active regions firing gas and dust jets. The bow shock, the diamagnetic cavity and other structures in the cometary environment were also detected, establishing the foundations of the theories and models of cometary plasma environment. In 2002, the spacecraft of the mission Stardust collected dust particles within 240 km of Comet Wild 2 and delivered the sample back to the Earth. The laboratory analysis of the sample detected some refractory materials, which can only be formed at a high temperature, indicating mixing and transportation of material in the early solar nebula. In 2005, two spacecrafts of the Deep Impact mission approached Comet Tempel 1. One of the spacecraft served as the impactor, which collided into the comet's nucleus and excavated the interior material below the surface. The other one recorded images and data to analyze the composition of the material released by the impact. The impact generated a very large and bright dust cloud, the analysis of which indicated there was more rocky and dusty material than the icy one. Another major result was that the composition of the ejected plume material was the same as the ambient coma so by inference the composition of the normally produced coma was very similar to that of the nucleus at some depth.

To closely monitor the evolution of the coma and the nucleus, the more ambitious Rosetta mission has been carried out. It sent the first spacecraft orbiting the comet's nucleus from a heliocentric distance of 3.3 AU through perihelion at 1.24 AU. The

environment of the inner coma and the nucleus surface were continuously measured in-situ and remotely by the instrumentation on board within 200 km to the nucleus, so that the transformation of the frozen comet by the solar heating and the response of coma can be revealed. The spacecraft also dispatched a robotic lander, Philae, for a touchdown on the nucleus surface, attempting to sample the surface and the subsurface material. However, during the touchdown, the anchoring harpoons of the lander failed to deploy and cling to the surface. Some images of the surface where it eventually rested on the nucleus were taken closely and sent back for analysis. Despite the partly failure of the lander, the abundant observational data from the orbiter can still contribute to our knowledge of comets.

To interpret the observational data and understand the complicated cometary plasma and neutral environment, many numerical models have been developed. Though most of the models are based on first principles, they differ in the underlying approximations, assumptions and physical and chemical processes. For example, fluid models treat neutral gases and ions as one or several fluids, the dynamics of which are governed by a set of fluid equations. In kinetic or hybrid models, neutral molecules and ions are treated as macro-particles, and the motion of each particle obeys the equation of the particle's motion. The differences in assumptions of various models often lead to specialized applications of each model. A cometary environment model should be selected and tailored, according to the length scale, the time scale, and the physical and chemical processes of the problem of interest. In addition, due to the limitation of the computational resources, computational time and complexity should also be taken into considerations for the model selections.

In this thesis, I focus on modeling the neutral coma, the interaction between the comet and the solar wind, and the dust grains in the cometary environment all by the fluid approach. Chapter 2 will provide the general background on the neutral coma with important physical and chemical processes in the coma. The description of the

multi-fluid coma model will be detailed with a brief introduction to existing models. Chapter 3 will first review the knowledge on classical plasma cometary environment, which was mostly obtained from the missions to comet Halley. Then following a review of current fluid models and hybrid models, the multi-species cometary plasma model is described. Chapter 4 will discuss the dust grains' behavior and the underlying physical processes, before introducing the equations and assumptions of the dust fluid model. Chapter 5 will be devoted to the implementation of numerical methods used in this work. Chapter 6 to Chapter 8 will detail the applications of the multi-fluid neutral coma model, the multi-species plasma model and the multi-fluid dust fluid model. Chapter 9 concludes the thesis and discusses the possible future work.

CHAPTER II

The neutral gas environment and models

Most cometary observations are made of the cometary atmosphere, which provide parameters and constraints to theories and models of cometary environments. On the other hand, a better understanding of the cometary structure and a physics-based model can also help improving the analysis and interpretations of observations. This chapter will first detail the important physical and chemical processes in the cometary neutral gas environment, i.e., the sublimation of volatiles from the nucleus surface, photo-chemistry, intermolecular collisions and radiative cooling in the coma. Several existing models will be introduced and discussed in terms of their validity and applicability.

2.1 Physical processes in the coma

2.1.1 Sublimation of volatiles from the nucleus surface

According to our current understanding of comets, the major source of the coma for most comets is the gas sublimated from the nucleus. *Whipple* (1950) proposed a "dirty snowball" model to describe the nature of the cometary nucleus and the source of coma and tail. In the dirty snowball model, the cometary nucleus is a conglomerate of volatile ices and refractory materials and is able to supply gases and dust grains for the formations of coma and tail after several revolutions around the sun. As the

nucleus approaches the sun, the increasing solar radiation heats the nucleus to enable larger amount of sublimation of various volatiles, which leads to increasing production rates in the observations. Though a recent finding by the Rosetta mission shows that rocky materials dominate most of the nucleus surface (*Capaccioni et al.*, 2015), this simple model is still consistent with diurnal variations of the activity on the surface.

A more complete model of the nucleus gas production should also include the absorption of solar energy, thermal radiation of the nucleus, recondensation of gas in the coma and various processes inside the nucleus, such as heat conduction in the rocky material, mass and energy transportation caused by the sublimation and recondensation of ice under the surface. An example of the thermo-physical model can be found in (*Davidsson and Gutiérrez*, 2005, 2006). Our gas model in this thesis needs the gas flux and gas temperature on the surface given by such models to supply the inner boundary conditions.

In the process of sublimating, the initially stationary gas molecules start accelerating right at the surface and expand into the coma. The gas is subsonic at first and is accelerated to become supersonic due to the pressure gradient. The transonic process can introduce an undefined singular point for a fluid or hydrodynamic model. *Marconi and Mendis* (1983) and *Gombosi et al.* (1985) used various techniques to solve the issue. In addition to the sonic point, a thin Knudson layer of several mean free paths thick forms close to the nucleus surface. In that layer, the gas may not be in an equilibrium state and therefore the fluid approach may not be valid. Therefore, recent fluid models (e.g., *Crifo et al.* (2003)) and the model in this thesis prescribe the inner boundary conditions above the Knudson layer with a supersonic initial velocity for the gas sublimated from the surface.

2.1.2 Photochemistry

Photochemical reactions, including photo-dissociation and photo-ionization, play an important role in the cometary coma, since they not only alter the composition, but also fuel the coma with their released excess energies (*Combi et al.*, 2004). One typical example of photo-dissociation reaction of H_2O is

$$H_2O + hv \rightarrow H + OH + \Delta E$$

. When one H_2O molecule dissociates, its energetic daughter species H and OH are born, with average speeds of 17.5 km/s and 1 km/s, respectively. The additional kinetic energy is provided by the excess energy ΔE= 1.7 eV. Because of collisions in the coma, the kinetic energy is partially redistributed among nearby gas molecules and also used to heat the coma. Via different reactions taking place at different wavelengths, H_2O can be converted to various daughter and granddaughter species with different kinetic energies, such as OH, H, H_2, O and other ion species. Increasingly accurate measurements of the photochemical reaction rates at different wavelengths, exothermic velocities of the products have enabled us to better understand the dynamics and composition in the coma. *Huebner et al.* (1992) contains abundant information on the numerous photo-chemical reactions in the coma. The updated wavelength-dependent photo-destructions for H_2O and corresponding branching ratios and exothermic velocities can also be found in Table 1 of *Combi et al.* (2004).

In addition, numerous photochemical reactions also provide abundant opportunities to measure the coma. For instance, a lack of visible band signatures and the effect of telluric water make the water in the coma difficult to observe. However, the products of photo-dissociation of H_2O facilitate various observational techniques at different wavelengths, which can also reveal the production rate, temperature, and expansion speed of H_2O. To name a few, *Bockelee-Morvan et al.* (1990) developed

a "trapezoid method" to measure the average radial outflow velocity in 18-cm OH emissions. *Combi et al.* (2011) used series of images of Lyman-α emissions of extended H coma to derive the time varying H_2O production rate.

2.1.3 Collisions

Collision plays an important role in the gas dynamics of the cometary coma, as it is the major micro-mechanism responsible for many physical processes in the coma, i.e., gas diffusion, heat conduction, momentum and energy exchange between different particles, and redistribution of excess energies deposited by photo-chemical reactions. Every collision takes place between two particles, accompanied by momentum and energy exchange. In the process, the total momentum and energy are conserved, while the conservation of total kinetic energy does not necessarily hold. Depending on whether the kinetic energy is conserved or not, collisions can be classified into two types: elastic or inelastic. Generally, for low kinetic energies, elastic collisions dominate. As the relative kinetic energy increases, the inelastic collisions become more important, because they are more likely to trigger rotational, vibrational and electron excitations and ionization (*Schunk and Nagy*, 2009).

Collisions in the inner coma have a higher frequency than the outer coma, for the collision frequency is proportional to the gas densities. Since the collision frequency is higher than the frequency of radiative processes, a local thermal dynamic equilibrium (LTE) can be reached in the inner coma. In addition, collisions also thermalize the energetic particles of daughter species produced by photo-dissociation, accelerate the parent species and redistribute the excess energies. We will use the major photo-dissociation reaction for H_2O to illustrate.

$$H_2O + h\nu \rightarrow H + OH + \Delta E$$

Due to the conservation of momentum, the H atom has a speed 17 times that of OH molecules. If the gas density is high, these superthermal H atoms will be thermalized after plenty of collisions with other atoms and molecules. In this process, the kinetic energy of the superthermal H atoms will be transformed to thermal energies and will be redistributed among all species. If the gas density is low, the superthermal H atom escapes before enough collisions take place, resulting in a lower heating efficiency.

As the cometocentric distance increases, the gas density decreases and the collision frequency becomes lower than the frequency of the radiative processes. As a result, the outer coma is in a non-LTE condition and dominated by the fluorescence equilibrium or radiative equilibrium, in which the rotational temperature and the kinetic temperature are not the same. Also the kinetic distributions of different species are different and in general non-Maxwellian (*Bockelee-Morvan and Crovisier*, 1987).

The important effects of collisions should be taken into account whether in interpreting the observational data or in modeling the dynamics of the coma. However, different models have different implementations of the collisions and corresponding effects, which will be discussed in the section on models later.

2.1.4 Radiative cooling effect

While photo-chemical reactions provide energy to fuel and heat the coma, the radiative cooling effect is the most important mechanism to reduce the energies of neutral and ionized gases in the inner coma. This effect cannot only impede the acceleration of the expansion speed of coma, but is also able to alter the temperatures of neutral gases, ions, and electrons in the coma, which controls the chemical reactions and thus may affect the composition as well. Water has a major role in the radiative cooling effect of the coma, because of its abundance and the high cooling efficiency. The coma can be effectively cooled down by the emission of rotational lines of H_2O molecules at the infrared wavelength. *Shimizu* (1976) first proposed an empirical

formula for the cooling rate of H_2O in both LTE and non-LTE conditions. The cooling rate L is expressed as follows:

$$L = \frac{8.5 \times 10^{-19} T_{H_2O}^2 n_{H_2O}^2}{n_{H_2O} + 2.7 \times 10^7 T_{H_2O}} \text{erg cm}^{-3}\text{s}^{-1}. \tag{2.1}$$

However, for active comets with a production rate higher than 10^{30}s^{-1}, the cooling rate tends to be overestimated, due to the high optical thickness preventing the photons from escaping from the inner coma. It is confirmed by an analytical analysis based on the GEISA spectroscopic data in *Crovisier* (1984). *Gombosi et al.* (1986) provided a better formula taking into account the effect of infrared optical depth τ_{IR}.

$$L = \begin{cases} -4.4 \times 10^{-22} T_{H_2O}^{3.35} n_{H_2O} \exp(-\tau_{IR}), & \text{if } T_{H_2O} < 52K \\ -2.0 \times 10^{-20} T_{H_2O}^{2.47} n_{H_2O} \exp(-\tau_{IR}), & \text{otherwise} \end{cases} \tag{2.2}$$

The cooling term from *Shimizu* (1976) is probably outdated, but in practice the effect of using a better approach on normal comets are small.

2.2 Coma models

In this section, we will introduce three widely used coma models. The first one is the Haser model, which provides the analytical solutions of the number density of certain species based on the most simplified assumptions but has various applications in observational and modeling work. The other two are physics-based models, representing two approaches of tackling such problems: the kinetic or particle approach and the fluid approach. We will use the Direct Simulation Monte Carlo method as an example of the kinetic approach as the standard for our comparison and then detail the multi-fluid model, which is used for applications in Chapter 5.

2.2.1 Haser model

Assuming the coma is expanding at a constant radial speed v, *Haser* (1957) derived the function of the number density of certain coma species at a distance r to the nucleus, which can be written as follows:

$$n(r) = \frac{Q}{4\pi r^2 v} \exp(-r/\gamma_p) \tag{2.3}$$

Q is the production rate of the comet, γ_p is the scale length of that species, which can be computed by $\gamma_p = v/\nu_{ph}$ and ν_{ph} is the photo-destruction frequency. $4\pi r^2$ is the factor accounting for the spherical expansion, $\exp(-r/\gamma_p)$ represents the decay caused by the photo-destruction processes. Under similar assumptions, Haser model also gives the density distribution of the daughter species, which is produced by the parent species in the coma. The density distribution of the daughter species can be written as

$$n_d(r) = \frac{Q}{4\pi r^2 v} \frac{\gamma_d}{\gamma_p - \gamma_d} (\exp(-r/\gamma_p) - \exp(-r/\gamma_d)), \tag{2.4}$$

where γ_p and γ_d are the scale length of the parent species and daughter species, respectively. The Haser model neglects the complicated variations in the speed and temperature, but captures the fundamental photo-destruction and spherical expansion processes in the coma by simple expressions. Therefore, it is still widely used today, especially with observed intensity spatial profiles, which are approximately proportional to the column density profiles. For the daughter species version the Haser model also neglects the important effect of the excess energy imparted to the daughter fragment when the parent is photodissociated (*Combi and Delsemme*, 1980; *Festou*, 1981).

2.2.2 Direct Simulation Monte Carlo method

The kinetic approach uses a probability distribution function defined in phase space $(\mathbf{r}, \mathbf{v})$ to describe the physical state of an ensemble of gas particles. $f(\mathbf{r}, \mathbf{v}, t)$ is the normalized phase-space distribution function, which gives the probability density of finding a particle at the space position $\mathbf{r}$ has a velocity $\mathbf{v}$. If the number density at r is also given, the number density of particles near $\mathbf{v_0}$ in the velocity space can be calculated by $f(\mathbf{r}, \mathbf{v_0}, t)dv^3n(r)$. Since the integration of $f(\mathbf{r}, \mathbf{v}, t)$ over the whole velocity space is unity, the average macroscopic properties can be derived from the normalized phase-space distribution function,

$$\overline{Q}(\mathbf{r}, \mathbf{v}, t) = \int Q(\mathbf{r}, \mathbf{v}, t) f(\mathbf{r}, \mathbf{v}, t) d^3v, \tag{2.5}$$

Q can be any microscopic quantities and $\overline{Q}$ is the macroscopic quantity or the statistical average of microscopic quantity Q. For example, the bulk velocity $\mathbf{u}$ at $\mathbf{r}$ is

$$\mathbf{u}(\mathbf{r}, t) = \int \mathbf{v}(\mathbf{r}, t) f(\mathbf{r}, \mathbf{v}, t) d^3v. \tag{2.6}$$

The temperature can also be derived by taking integration of moments of velocity v with the phase-space function:

$$\frac{3}{2}kT = \int \frac{m}{2} f(\mathbf{r}, \mathbf{v})(\mathbf{v} - \mathbf{u})^2 dv^3, \tag{2.7}$$

where k is the Boltzmann constant and m is the molecular mass.

The evolution of the phase space distribution function is determined by the external forces and the net effects of collisions between the particles. The rate of change of f can be calculated by

$$\frac{df(\mathbf{r}, \mathbf{v}, t)}{dt} = \lim_{dt \to 0} \frac{f(\mathbf{r} + d\mathbf{r}, \mathbf{v} + d\mathbf{v}, t + dt) - f(\mathbf{r}, \mathbf{v}, t)}{dt} \tag{2.8}$$

The term $f(\mathbf{r}+d\mathbf{r}, \mathbf{v}+d\mathbf{v}, t+dt)$ can be expanded in a Taylor series to the first order.

$$f(\mathbf{r}+d\mathbf{r}, \mathbf{v}+d\mathbf{v}, t+dt) = f(\mathbf{r}, \mathbf{v}, t) + \frac{\partial f}{\partial t}dt + \nabla_{\mathbf{r}} f \cdot d\mathbf{r} + \nabla_{\mathbf{v}} f \cdot d\mathbf{v} \tag{2.9}$$

Because $\mathbf{v} = \frac{d\mathbf{r}}{dt}$ and $\mathbf{a} = \frac{d\mathbf{v}}{dt}$, the rate of change of $f(\mathbf{r}, \mathbf{v}, t)$ can be written as

$$\frac{d\, f(\mathbf{r}, \mathbf{v}, t)}{dt} = \frac{\partial f(\mathbf{r}, \mathbf{v}, t)}{\partial t} + \mathbf{v} \cdot \nabla_{\mathbf{r}} f(\mathbf{r}, \mathbf{v}, t) + \mathbf{a} \cdot \nabla_{\mathbf{v}} f(\mathbf{r}, \mathbf{v}, t). \tag{2.10}$$

If collisions and external forces are negligible, the left hand side is equal to zero and the equation becomes the Vlasov equation. If the collisions are important, this equation becomes the Boltzmann equation shown below, which is the appropriate description of the physical state of gases, whether rarefied or not.

$$\frac{\delta\, f(\mathbf{r}, \mathbf{v}, t)}{\delta t} = \frac{\partial f(\mathbf{r}, \mathbf{v}, t)}{\partial t} + \mathbf{v} \cdot \nabla_{\mathbf{r}} f(\mathbf{r}, \mathbf{v}, t) + \mathbf{a} \cdot \nabla_{\mathbf{v}} f(\mathbf{r}, \mathbf{v}, t), \tag{2.11}$$

where $\frac{\delta\, f(\mathbf{r}, \mathbf{v}, t)}{\delta t}$ is the integral of collisions that account for inter-particle interaction. The Boltzmann equation does not make any assumptions or restrictions on the form of the distribution function or the integral of collisions, which leads to a wide range of validity and applicability.

However, even with simplified collisional terms and reduced spatial and velocity dimensions, few Boltzmann equations can be solved analytically. It is even more difficult to obtain analytical solutions in the context of complicated cometary environments. Therefore, numerical models have to be utilized to implement the kinetic approach in the coma modeling work.

The Direct Simulation Monte Carlo (DSMC) method (*Bird*, 1994) is one of the widely used numerical models to solve the multi-species and multi-dimensional Boltzmann equations in applications of the planetary atmosphere and the cometary atmosphere (*Combi*, 1996). In direct simulation methods, the distribution function is

approximated by a set of delta functions in velocity space and the phase space is divided into a regular network of cells. The most important feature of the DSMC method is that because it is based on the Monte Carlo methodology, it is able to avoid the formation of integro-differential equations and to solve the Boltzmann equation with a complicated collision integral accounting for complex chemical reactions and various types of collisions. In addition to the generality of the kinetic approach, the DSMC method makes solving the Boltzmann equation under various physical conditions of the cometary atmosphere possible and practical.

The general scheme of Monte Carlo methods can be described by Markov Chains for a discrete distribution or by Markov process for a continuous distribution function. The evolution of the distribution function $f(\mathbf{v}, t)$ is modeled as a Markov process, which is expressed as follows,

$$f(\mathbf{v}, t) = \int f(\mathbf{v} - \Delta\mathbf{v}, t) P(\mathbf{v} - \Delta\mathbf{v}, \Delta\mathbf{v}) d(\Delta\mathbf{v}), \tag{2.12}$$

where $P(\mathbf{v}, \Delta\mathbf{v})$ is the transition probability function, which gives the probability of a particle with a velocity $\mathbf{v}$ at time t having the velocity $\mathbf{v} + \Delta\mathbf{v}$ at time $t + \Delta t$. The transition probability function only depends on the current state and is not affected by the history, so it does not depend on time. In addition, the transition probability function is normalized,

$$\int P(\mathbf{v}, \Delta\mathbf{v}) d(\Delta\mathbf{v}) = 1. \tag{2.13}$$

Then the DSMC method incorporates the transition probability function, which is defined explicitly or implicitly by the microphysical processes in the coma and provides the foundation for the evolution and the relaxation of the modeled distribution function, allowing the distribution function to converge to the solution of the Boltzmann equation regardless of the initial conditions. The procedure of running a DSMC model is as follows. First, the initial condition is set by distributing a certain num-

ber of particles all over the computational domain. For every time step, boundaries eject new particles with specific number density, velocity and a certain distribution function into the computational domain, according to the physics of the problem concerned. The boundaries can also reflect or eliminate the particles leaving the domain. The time step is limited by the mean free path so that only a fraction of particles undergo collisions and the trajectories of particles can be more accurately approximated by discrete segments. In every time step, particles will do a free-molecular motion with current velocities and their locations are changed accordingly. Based on the frequency or probability of the collisions and chemical reactions, corresponding operations are computed for a set of representative particles. For example, the collision probability is proportional to the product of cross-sections of particles and relative velocities and the probability gives the number of collisions that should occur locally. Then randomly selected pairs of particles exchange momentum and energy based on how the collision is modeled. During the process, the rotational, vibrational, and translational energies can be redistributed. Repeating the process for sufficient time, the final steady state can be reached. The interested macroscopic quantities such as density, velocity and temperature can be sampled or averaged in every cell.

However, the finite number of modeled particles can introduce a correlation between them. A significant correlation (statistical dependence) can prevent a DSMC solution from converging to the solution of the Boltzmann equation. Because of the statistical nature of the DSMC method, a large number of particles are needed to minimize the noise and reduce the effect of the correlation. Due to the tradeoff between accuracy and the number of particles, the DSMC method can be extremely computationally expensive, especially in time-dependent models where a gigantic amount of particles are needed to build statistics for time-varying conditions.

2.2.3 Fluid models

Grad (1949) first showed that a set of generalized transport equations of an arbitrary size can be derived by taking velocity moments of the Boltzmann equation, since every order of velocity moments can produce one equation. However, the equations are not closed, since the transport equation for the moment of order l contains the moment of order l+1. In order to have a closed system of transport equations and to evaluate the velocity moments of the collision terms, assumptions on the distribution function have to be made. The Maxwellian distribution function is often used as the zeroth order of approximation of the distribution function in the Boltzmann equation. Assuming the distribution function does not deviate too far from the Maxwellian distribution, it can be approximated in terms of the physically significant moments of the distribution function (density n_s, velocity $\mathbf{u}_s$, temperature T_s, pressure tensor $\mathbf{P}_s$, viscosity tensor τ_s, heat flux $\mathbf{q}_s$). Depending on how many velocity moments are used in the description of the distribution function, the same number of equations can form a closed system. For example, the 13-moment approximation is shown below, which leads to 13-moment transport equations.

$$f_s = f_{s0}\left[1 + \frac{m_s}{2kT_s p_s}\tau_s \colon \mathbf{c}_s\mathbf{c}_s - (1 - \frac{m_s c_s^2}{5kT_s}\frac{m_s}{kT_s p_s})\mathbf{q}_s \cdot \mathbf{c}_s,\right], \tag{2.14}$$

where random velocity $\mathbf{c}_s = \mathbf{v}_s - \mathbf{u}_s$ and f_{s0} is the Maxwellian distribution function.

If the 5-moment approximation is used, the Navier-Stokes equations, the governing equations in some fluid models can be obtained (*Crifo et al.*, 2003). The zeroth order, first order and second order velocity moments of the Boltzmann equation lead to the continuity, momentum, and energy equations, respectively. Therefore, we can see the fluid approach is linked to the kinetic approach by the Boltzmann equation with additional assumptions of the distribution function.

The kinetic approach does not make any assumption on the distribution function

which the Boltzmann equation solves, while the fluid approach is derived by taking moments of the Boltzmann equation and is often under the assumption that the distribution function does not deviate too far from the Maxwellian distribution, which assumes a collisional regime and may impose limitations to the fluid approach. While the coma may be dense and highly collisional near the nucleus, by thousands to millions of kilometers away it becomes rarefied and almost collisionless.

The Knudsen number serves as a criterion to check the validity or the applicability of a fluid model. It is the ratio of the mean free path λ to the minimum scale length of all fluid quantities, which can be expressed as follows in a single species gas,

$$K_n = \frac{\lambda}{\rho/|\nabla\rho|}. \tag{2.15}$$

If K_n is less than 0.1, collisions are frequent enough so that the distribution function can be still approximated by a Maxwellian (*Marconi et al.*, 1996). *Crifo et al.* (2003) also showed excellent agreement between their single-fluid gas dynamic model based on Navier–Stokes equations and their DSMC model for a low production rate of about $10^{23}\,\mathrm{s}^{-1}$ and a Knudsen number up to 1. As the Knudsen number in a real cometary environment may have a wide range, the fluid approach is only physically correct in a limited region, while the kinetic approach can be applied to the whole domain. However, when it comes to modeling a bright comet or a time-dependent phenomenon, it is computationally expensive to simulate a large number of particles, because the small mean free path severely limits the time step.

In the thesis, we develop a 3D multi-fluid model, which treats H_2O, OH, H_2, O, and H as separate fluids and each fluid has its own density, velocity, and temperature. Photo-chemical reactions and collisions are included. Collisions between fluids allow different gases to exchange momentum and energy. The collision frequency is proportional to the gas densities of both interacting species, so the model is able to

address the heating efficiency issue in a self-consistent way.

Our multi-fluid model solves a set of hydrodynamic Euler equations for each species, which also represent the lowest order closure of the general Boltzmann equation and are shown in Equations 2.16-2.18. They are the continuity equation, the momentum equation, and the pressure equation. ρ_s, $\mathbf{u}_s$, p_s are the mass density, the velocity vector, and the scalar pressure of the neutral species s. γ_s denotes the specific heat ratio of species s. The terms on the right hand sides of the equations represent the source terms, which are specified for each species and include collisions, chemical reactions, radiative cooling, and photo-dissociations.

$$\frac{\partial \rho_s}{\partial t} + \nabla \cdot (\rho_s \mathbf{u}_s) = \frac{\delta \rho_s}{\delta t} \tag{2.16}$$

$$\frac{\partial \rho_s \mathbf{u}_s}{\partial t} + \nabla \cdot (\rho_s \mathbf{u}_s \mathbf{u}_s + p_s \mathcal{I}) = \frac{\delta \rho_s \mathbf{u}_s}{\delta t} \tag{2.17}$$

$$\frac{\partial p_s}{\partial t} + \nabla \cdot (p_s \mathbf{u}_s) + (\gamma_s - 1) p_s (\nabla \cdot \mathbf{u_s}) = \frac{\delta p_s}{\delta t} \tag{2.18}$$

The source terms are described in Equations 2.19-2.22. Those source terms with chemical reaction frequencies $\nu_{s \to t}$ are related to photo-chemical reactions. In the pressure source term, the excess energies are partitioned under the restriction that the momenta of the daughter species should be conserved and thus are inversely proportional to the mass. The source terms involving momentum transfer coefficients $\overline{\nu}_{s,t}$ between species s and t are terms accounting for collisions. The collision frequency is linearly proportional to the density of each involved gas species, and the relative speed of the colliding gas molecules or atoms, which is calculated from the thermal

and bulk velocities of both species. To account for the infrared cooling effect of H_2O, a cooling function L is added to the pressure source term of H_2O. L is expressed as, $L = \frac{8.5\times10^{-19}T_{H_2O}^2 n_{H_2O}^2}{n_{H_2O}+2.7\times10^7 T_{H_2O}}$ erg cm^{-3}s^{-1}, which was first proposed by *Shimizu* (1976), and work well for the normal comets discussed in Chapter 5. But it needs additional adjustment involving optical depth for production rates higher than 10^{30}s^{-1}, since the inner coma under such circumstances are optically thick, preventing efficient radiative cooling. The adjusted cooling rate can be found in *Gombosi et al.* (1986), which for the cases shown here gives similar results as the more complex approaches that account for the non-LTE effects between kinetic and rotational temperature (*Combi*, 1996; *Tenishev et al.*, 2008). However, the DSMC model can account for rotational excitation in collisions. In the fluid model we implicitly assume that T_{rot}=T_{kin} at least in the cooling term. It could be handled better in the fluid code using a different gamma for each species appropriate for monatomic, diatomic, triatomic, and even having a temperature dependent gamma for very low temperatures. But as the comparison of the new multi-fluid results with the full kinetic DSMC model in Chapter 5 shows the effects of these complications are not large.

$$\frac{\delta\rho_s}{\delta t} = \sum_{n=\text{neutrals}} \nu_{n\to s} n_n m_s - \sum_{t=\text{other species}} \nu_{s\to t} n_s m_s \tag{2.19}$$

$$\frac{\delta\rho_s \mathbf{u}_s}{\delta t} = \sum_{n=\text{neutrals}} \nu_{n\to s} n_n (\mathbf{u}_n - \mathbf{u}_s) m_s + \frac{\delta\rho_s}{\delta t}\mathbf{u}_s + \sum_{t=\text{other species}} \overline{\nu}_{s,t} n_s m_s (\mathbf{u}_t - \mathbf{u}_s) \tag{2.20}$$

$$\overline{\nu}_{s,t} = \frac{m_t}{m_t + m_s} n_t \sigma_{s,t} \sqrt{\frac{8k}{\pi}\left(\frac{T_t}{m_t} + \frac{T_s}{m_s}\right) + (\mathbf{u}_t - \mathbf{u}_n)^2} \tag{2.21}$$

$$\frac{\delta p_s}{\delta t} = (\gamma_s - 1)\frac{m_s}{m_n}\nu_{n\to s} n_n \Delta E_{n\to s} + \frac{1}{2}\nu_{n\to s} p_n + \frac{1}{3}\nu_{n\to s} n_n (\mathbf{u}_s - \mathbf{u}_t)^2 m_s$$
$$- \sum_{t=\text{other species}} \nu_{s\to t} p_s + \sum_{t=\text{other species}} \overline{\nu}_{s,t} \frac{m_t m_s}{m_t + m_s} n_s \left[\frac{2}{3}(\mathbf{u}_s - \mathbf{u}_t)^2 + \frac{2k(T_t - T_s)}{m_t}\right] \tag{2.22}$$

We note here that collisions in our model conserve momentum and energy. The sums of the collisional sources of momentum and energy of two colliding fluids are zero. However, the pressure sources rather than the energy sources are presented here, because the collisional terms in pressure equations are more concise and clear.

CHAPTER III

The cometary plasma environment and the models

Photo-ionization and electron impact can ionize neutral particles in the expanding cometary coma and the resulting cometary ions start to be subject to the effect of the interplanetary magnetic field (IMF) embedded in the solar wind, which is mainly composed of protons and electrons originating from the sun. The chemical and physical processes among the cometary neutral and charged particles, the magnetized and super-superalfvenic solar wind, are often referred to as the comet-solar wind interaction, which creates the unique cometary plasma environment. This chapter will first introduce the pre-Rosetta knowledge of the cometary plasma environment, which is accumulated mainly by the observations from a handful of space missions. The physics underlying the ion tails, the diamagnetic cavity and the cometary bow shock will be discussed. Then a brief introduction to current cometary plasma models is presented and the multi-species model developed and used in this thesis will be detailed.

3.1 The pre-Rosetta understanding of the cometary plasma environment

The first study of the comet-solar wind interaction in history is Ludwig Biermann's statistical study of the pointing direction of the cometary ions tails (*Biermann*, 1951).

Biermann found that the thin and long ion tails always pointed away from the sun within a few degrees, which led him to suggest the existences of a solar corpuscular radiation (i.e., a continuous flux of charged particles or the solar wind) in space to sweep away the cometary ions. Assuming the momentum transfer between the solar wind and the cometary ions were solely caused by the collisional Coulomb interaction, *Biermann* (1951) inferred that the solar wind velocity should be a few hundred kilometers per second and the solar wind density was about 1000 cm^{-3}. Later *Alfvén* (1957) pointed out that the solar wind density was about 500 times larger than the observed coronal densities and offered a new model for the formation of the cometary ion tails, which is shown in Fig 3.1. In the model, he suggested the interplanetary

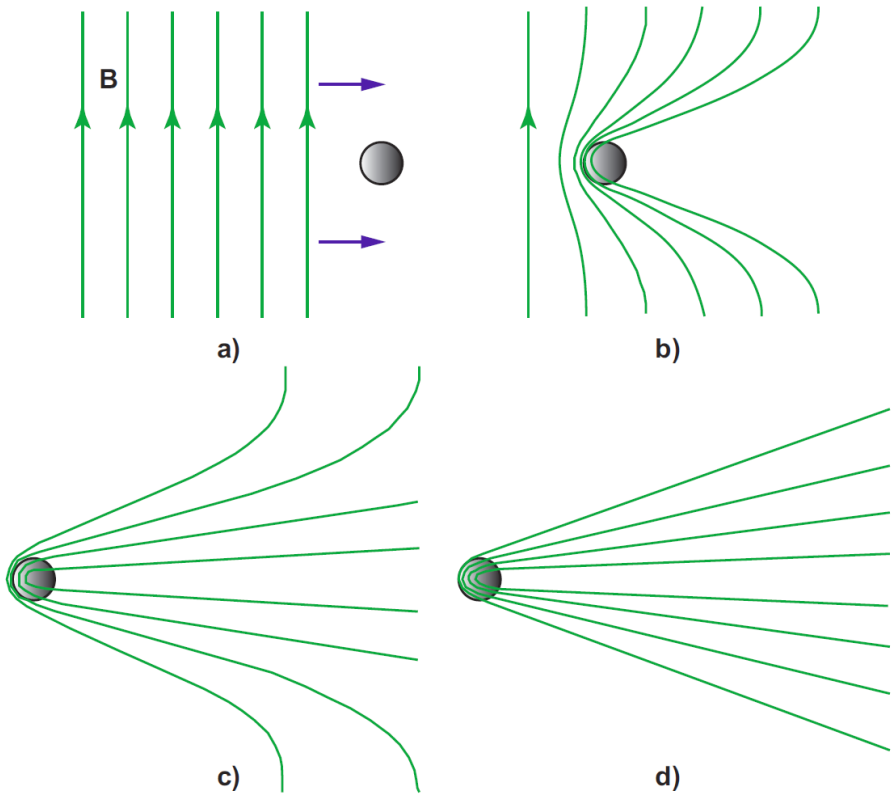

Figure 3.1: A scenario of the cometary ion tail formation proposed by *Alfvén* (1957).

space was filled with the solar wind flow carrying the "frozen in" magnetic field of solar origin. When the solar wind encountered the obstacle imposed by the cometary

atmosphere, the flow slowed down and the magnetic field started draping around the comet. The resulting straight magnetic field in the anti-sunward direction facilitated the momentum transfer between cometary ions and the solar wind and also led to the formation of an extremely long ion tail.

The study of the cometary ion tail predicted the existence of the solar wind and the interplanetary magnetic field before any spacecraft was sent to space, which suggests the potential of comets to reveal more knowledge about the sun and the heliosphere. In addition, the observations from several space missions to comets also show that comets can be perfect laboratories to study plasma physics from microscopic to macroscopic scales.

The ion pick-up is the most important physical process among the interactions between the solar wind and the unbounded and extended cometary atmosphere. Detailed discussion of this topic can be found in several nice review papers, e.g., *Galeev et al.* (1985) and *Szegö et al.* (2000). The process incorporates the cold and heavy cometary ions into the fast and hot solar wind. As the cometary ions are continuously produced by photo-ionization, electron impact ionization and charge exchange reactions in the coma, more mass is added to the solar wind flow. Due to the conservation of momentum, the solar wind flow is decelerated by the process, which is often referred to as the "massloading effect".

As soon as a cometary ion is born, its motion is controlled by the Lorentz force. The ion has a cycloidal trajectory, which is the combination of gyration around the magnetic field and the $\mathbf{E} \times \mathbf{B}$ drift. Assuming the ion has a zero initial velocity in space and the angle between the solar wind flow and the IMF is α, the velocity of the ion in the solar wind frame can be decomposed in two components: one is the beam velocity parallel to the magnetic field and the other is the gyration speed perpendicular to the magnetic field. Two components form a ring-beam distribution in the velocity space as shown in Fig. 3.2.

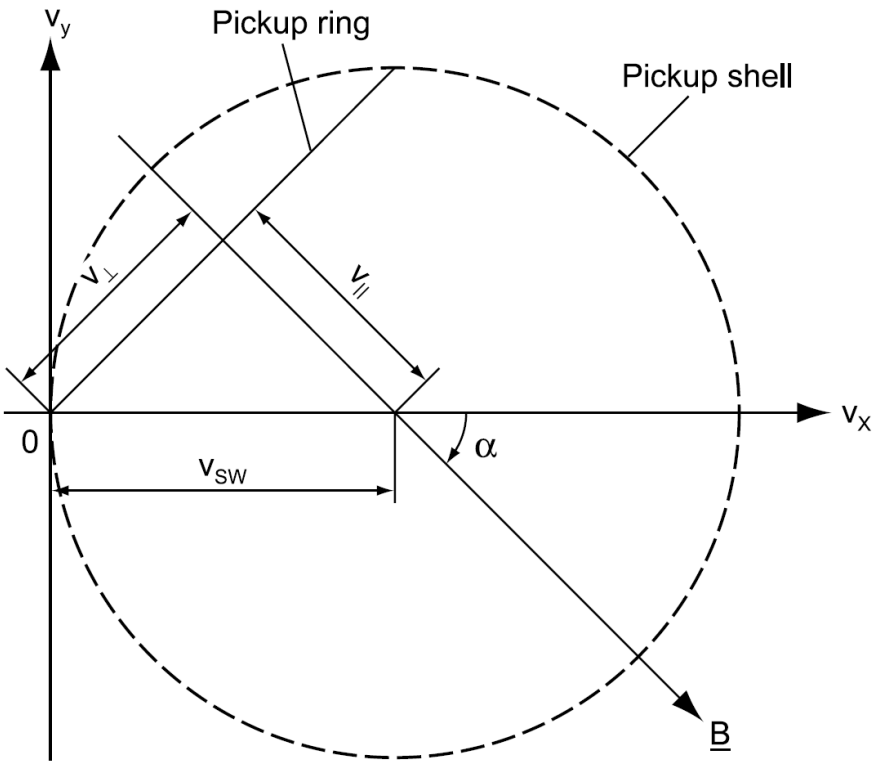

Figure 3.2: The two initial velocity components of the newborn cometary ion from *Ip* (2004).

The ring-beam distribution is highly unstable against the growth of ultra-low frequency (ULF) electromagnetic waves (i.e., frequencies near the heavy ion gyrofrequency, or 10 mHz). For less active comets or at large cometocentric distances, the wave spectrum tends to have a strong monochromatic component (e.g., comet Giacobini-Zinner far upstream) but tends to be turbulent-like for regions close to the comet (*Lee*, 1989). The magnetic field turbulence pitch-angle scatters the ions from the pickup ring to a spherical shell with a radius close to the solar wind speed, the process of which is illustrated in Fig. 3.3. We can see from the shell velocity distribution of the pick-up ions, one pickup ion contributes approximately $\frac{m_i}{3} v_{sw}^2$ to the plasma pressure, where m_i is the mass of the pickup ion and v_{sw} is the solar wind velocity.

Unlike the interaction between the solar wind and other solar system bodies with

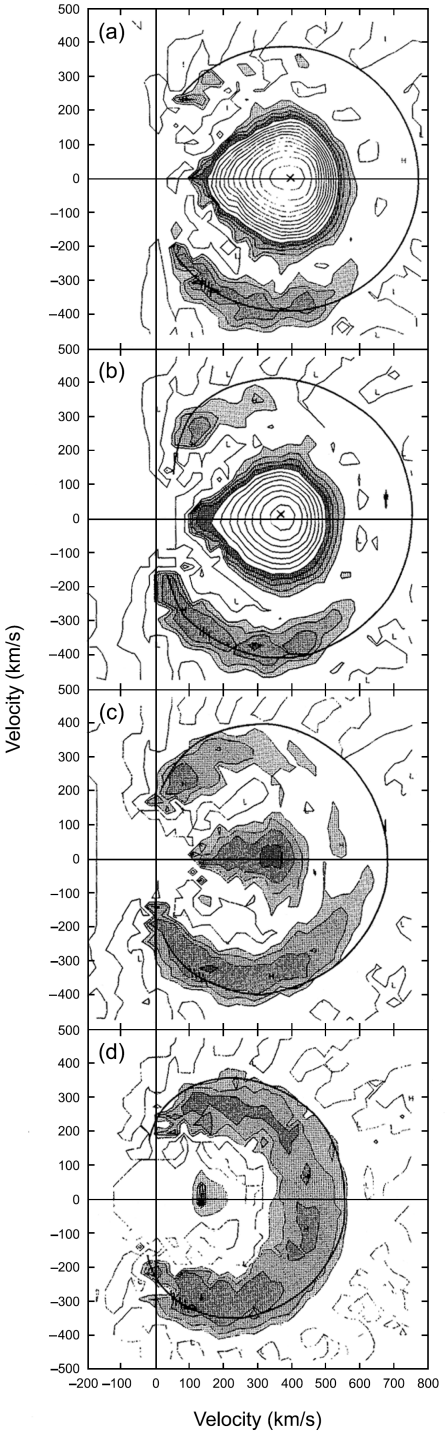

Figure 3.3: The phase space density distributions of pickup hydrogen ions upstream of the bow shock of comet Halley as observed by Giotto, which shows the evolution from a ring-beam distribution to a partially filled shell. From *Neugebauer et al.* (1987).

intrinsic magnetic fields or gravity-bounded atmospheres, the comet-solar wind interaction featured by the ion pickup process and the extended cometary atmosphere results in a unique cometary plasma structures. Fig. 3.4 shows the schematic of the

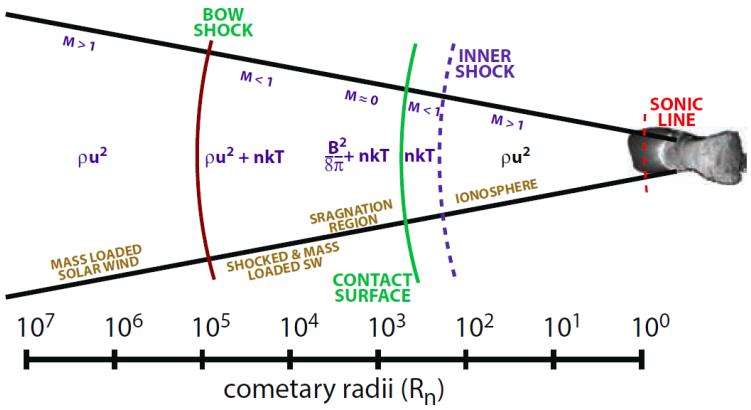

Figure 3.4: A schematic of the plasma environment on the day side of an active comet, from *Gombosi* (2015).

plasma environment on the day side of an active comet. We can see from the figure the characteristic length scales of the bow shock is about two orders of magnitude larger than that of the contact surface. The cometary tail, which is not shown in the figure, can be as long as several astronomical units. In-situ observations made by spacecrafts at various distances relative to comets have provided foundations to theories and models on these structures. The observations and theories of cometary bow shock, contact surface and the ion tail will be introduced and discussed in next sections. More detailed discussions on all cometary plasma structures can be found in review papers by *Ip* (2004) and *Gombosi* (2015).

3.1.1 Bow shock

Biermann et al. (1967) took the massloading effect into account and predicted that a cometary bow shock could be weak with a Mach number of 2, if it existed. The physical argument is that the gradual deceleration and heating of the supersonic and super-alfvenic solar wind plasma due to the effect of pick-up ions start at very

large cometocentric distances, which can be more than 1 million kilometers. As it gets closer to the comet, the Mach number keeps decreasing until a critical Mach number is reached and the flow velocity jumps to become subsonic. The evolution of the Mach number of the solar wind flow is quite different from that at planets, which tend to have a sharper transition of the Mach number across the bow shock. In addition, the presence of the cometary pick-up ions, the enhanced energetic particles and the associated large wave amplitude in the IMF enable a comet to be felt upstream of the shock in the supersonic plasma flow, which also makes the comet-solar wind interaction unique. Mars and Venus, without intrinsic magnetic fields but with somewhat extended coronae have been described as have a comet-like interaction with the solar wind. But their shocks are much sharper.

The predicted characteristics were confirmed by the observations of Giotto, VEGA and Suisei, during several encounters with comet Halley *Mukai et al.* (1986); *Huddleston et al.* (1992). Fig. 3.5 shows the solar wind flow vectors during the shock-crossing of spacecraft Suisei. The deflection and the deceleration of the solar wind flow can be clearly seen in the figure. However, the bow shock structure is not so well defined at comet 21P/Giacobini-Zinner in the observations of magnetometer and electron detectors on the spacecraft ICE, which is weaker than comet Halley. The magnetic field and the solar wind profile did not display clear jumps as expected in classical bow shocks(*Smith et al.*, 1986; *Bame et al.*, 1986). *Omidi and Winske* (1991) offered an interesting explanation the comet 21P/Giacobini-Zinner had multiple shocks instead of a single standing bow shock so that the solar wind could be decelerated more gradually and over a larger length scale than a few gyroradii of the cometary ions.

3.1.2 Contact surface

The shocked solar wind downstream of the bow shock flows towards the comet with a decreasing velocity as it approaches the comet, while the cometary ions in the

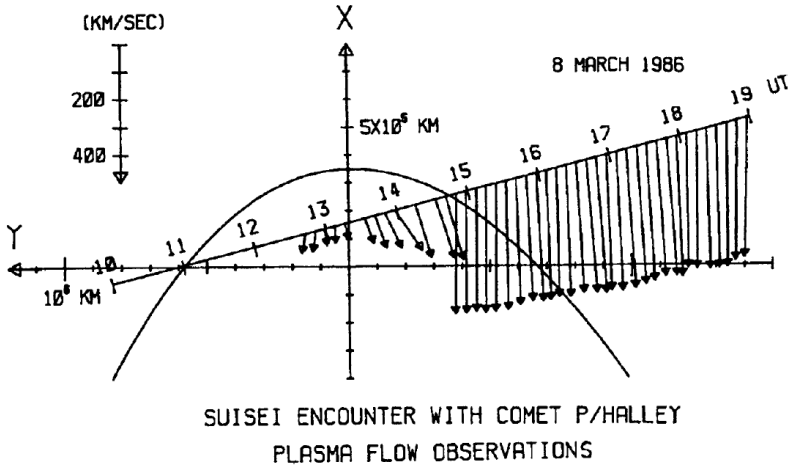

Figure 3.5: Solar wind flow vectors measured by the plasma analyzer on Suisei during its encounter with comet Halley, from *Mukai et al.* (1986).

innermost region are expanding in the radial direction as they are strongly coupled with the outflowing neutral gases by collisions. It can be expected that along the comet-sun line both the shocked and contaminated solar wind and the cometary ion flow should reach a stagnation point. In addition, *Wallis and Dryer* (1976) first predicted that a 2D boundary, namely the contact surface existed to separate these flows of two different origins. The shocked solar wind and the magnetic field frozen in the solar wind could not penetrate into the contact surface and the pure cometary ions should be decelerated and diverted tail-toward near the contact surface. This theory was confirmed by measurement of the magnetometer on Giotto at comet Halley, which detected a magnetic field free region at a cometocentric distance of 4700 km (*Neubauer et al.*, 1986).

Ip and Axford (1982) suggested that the position of the contact surface could be determined by the balance between the inward $\mathbf{j}\times\mathbf{B}$ force and the outward ion-neutral friction force. Right in front of the contact surface, the solar wind speed is very low and the magnetic field piles up. The magnetic pressure can be approximated by the dynamic pressure of the solar wind far from the comet, if the solar wind condition is given. The neutral gas density can be estimated by the Haser model without the

exponential decay term, while the ion population is mainly controlled by the chemistry equilibrium and is proportional to the inverse of the cometocentric distance. With some additional assumptions, *Cravens* (1986); *Ip and Axford* (1987); *Gombosi* (2015) developed analytic solutions to the size of the contact surface based on the underlying physics.

Chemical reactions also play an important role inside the contact surface and in front of it as it is able to alter the composition and affect the density profiles. Because of the large density of H_2O close to the comet, a proton exchange reaction

$$H_2O + H_2O^+ = H_3O^+ + OH$$

makes the H_3O^+ the dominant ion species inside of the contact surface by converting most of the H_2O^+ into H_3O^+. Chemical equilibrium is also the major mechanism of controlling the ion density profile as mentioned before. The production of ions by photo-ionization is balanced by the loss caused by electron recombination. The steady state equation describing the ion density in spherical coordinate system can be written as

$$\frac{1}{r^2}\frac{\partial}{\partial r}(r^2 n_i u_i) = \nu_{ph}\frac{Q}{4\pi r^2 u_n} - \alpha n_i^2. \tag{3.1}$$

Assuming $u_i = u_n$, we can find that the solution of n_i is proportional to the inverse of the cometocentric distance, differing from the neutral gas density profile mainly controlled by the transport effect. The reaction rate constant of electron recombination is sensitive to the electron temperature; therefore the electron temperature profile is important in modeling and data analysis. In the highly collisional domain, the electron temperature and the neutral temperature are in equilibrium. However, the collisions between the electrons and water molecules are able to cool the electrons and heat the water molecules initially and then trigger the rotational and vibrational excitations of water, which can effectively cool the neutral gas radiatively in the in-

frared. More detailed resources of all constants and reactions can be found in *Schunk and Nagy* (2009). As a result of rotational cooling and the almost stagnation of solar wind flow, an ion pile-up region or an enhanced ion density can be observed in front of the contact surface.

The sound speed of the ionospheric plasma inside the contact surface is about 0.35 km/s generally, and thus the cometary ions are also expanding supersonically. As a result, an inner shock exists just inside the contact surface to terminate the cometary ion flow. Once the flow reaches the inner shock, the normal component of the flow speed relative to the shock is decreased to zero and the flow is deflected toward the tail. Using MHD models, *Gombosi et al.* (1996) were able to produce a 3D structure of the contact surface, which has a tadpole shape as shown in Fig. 3.6.

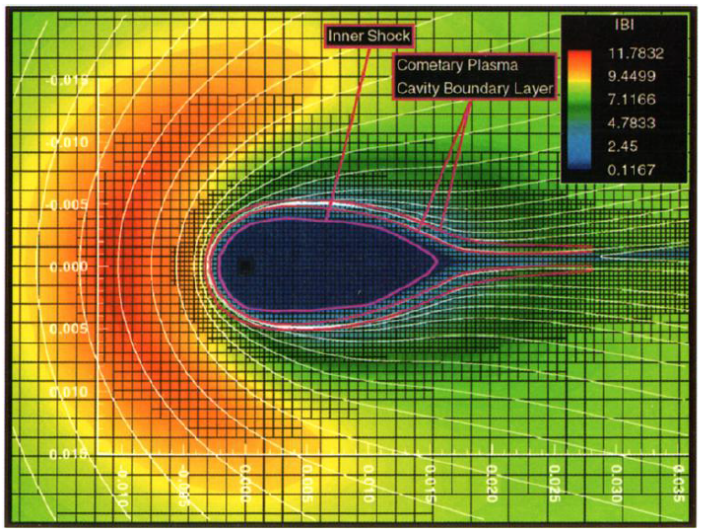

Figure 3.6: The modeled magnetic field lines and the magnitude of magnetic field around the contact surface. (*Gombosi et al.*, 1996).

3.1.3 The ion tail

The theory of ion tail formation was proposed by *Alfvén* (1957) and is illustrated in Fig. 3.1. The interplanetary magnetic field is draped around the contact surface and channels the cometary ions produced in the contact surface and the shocked solar

wind in the anti-sunward direction. Because of the resonance fluorescence processes of the cometary ions, a thin and narrow ion tail can be observed. The volume of the ion tail expands and the ion density drops at large distances from the nucleus. The magnetometer observations on the Ulysses spacecraft found that the ion tail of Comet Hyakutake (C/1996 B2) extended to a distance of more than 3.8 AU from the nucleus and the ion tail diameter is about 7×10^6 km (*Jones et al.*, 2000).

The structure of the ion tail has been confirmed by the in-situ measurements of a couple of tail crossings. In September 1985, the ICE spacecraft crossed the tail of comet 21P/Giacobini-Zinner and detected enhanced energetic ion flux and enhanced wave activity associated with the cometary pick-up ions.(*Bame et al.*, 1986; *Hynds et al.*, 1986) The Ulysses spacecraft had two interceptions of cometary ion tails at large distances. One is the tail crossing of comet Hyakutake (C/1996 B2) and the other one is at Comet C/2006 P1 (McNaught). From two tail crossings, The Solar Wind Ion Composition Spectrometer (SWICS) obtained two similar mass per charge spectrums, which are shown in Fig. 3.7 and Fig.3.8.

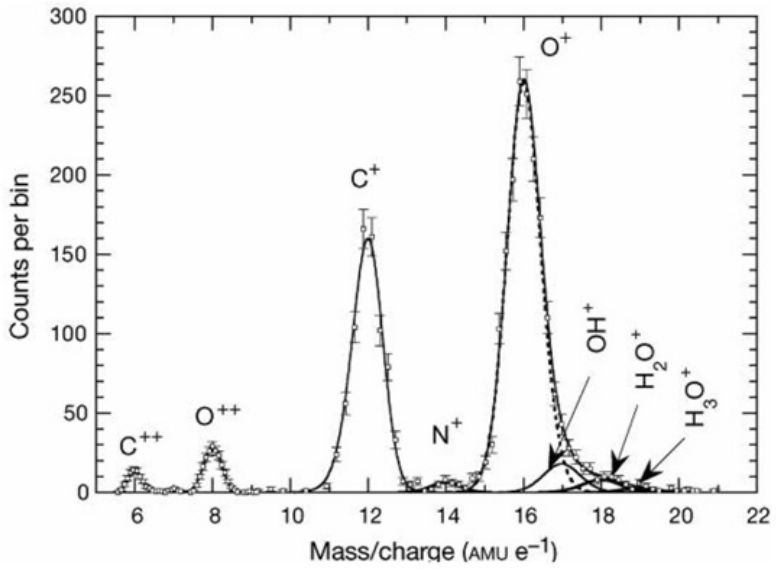

Figure 3.7: Mass/charge spectrum measured by Ulysses/SWICS during its encounter with the tail of comet Hyakutake. (*Gloeckler et al.*, 2000).

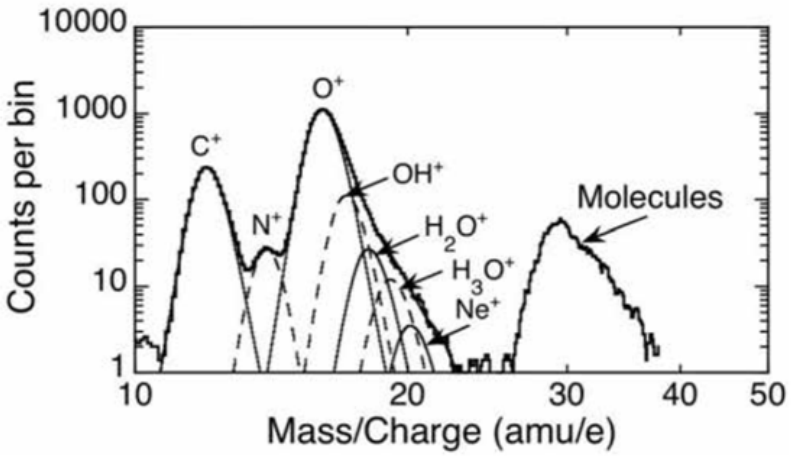

Figure 3.8: Mass/charge spectrum measured by Ulysses/SWICS during its encounter with the tail of comet McNaught. (*Neugebauer et al.*, 2007).

Water group ions (H_2O^+, H_3O^+, OH^+, O^+) are detected as the evidence of presence of a comet upstream, as the heavy minor ions of O, C, Ne, etc. in the normal solar wind are often highly ionized, like O^{6+}, O^{7+}, because of the high temperatures in the solar corona. The ratios between the counts of the water group ions are also similar in the figures, which may indicate that water is likely the dominant parent species on both comets. Fig. 3.9 shows the speed, density, and kinetic temperature of protons detected by SWOOPS and the magnitude and direction of magnetic field. Although relatively large wave activity seems to smear the signature of the magnetic field in the ion tail, we can still find dropouts of the proton density and velocity and an increase of proton temperature in the figure, which can also serve as the evidence of an ion tail crossing.

3.2 The plasma models

As more observational data are obtained, interesting cometary physics problems can arise at any scale lengths and at any positions in the cometary environment. Because of the interplay of all important and complicated physical and chemical processes which may occur everywhere, it can be oversimplified if any of them is

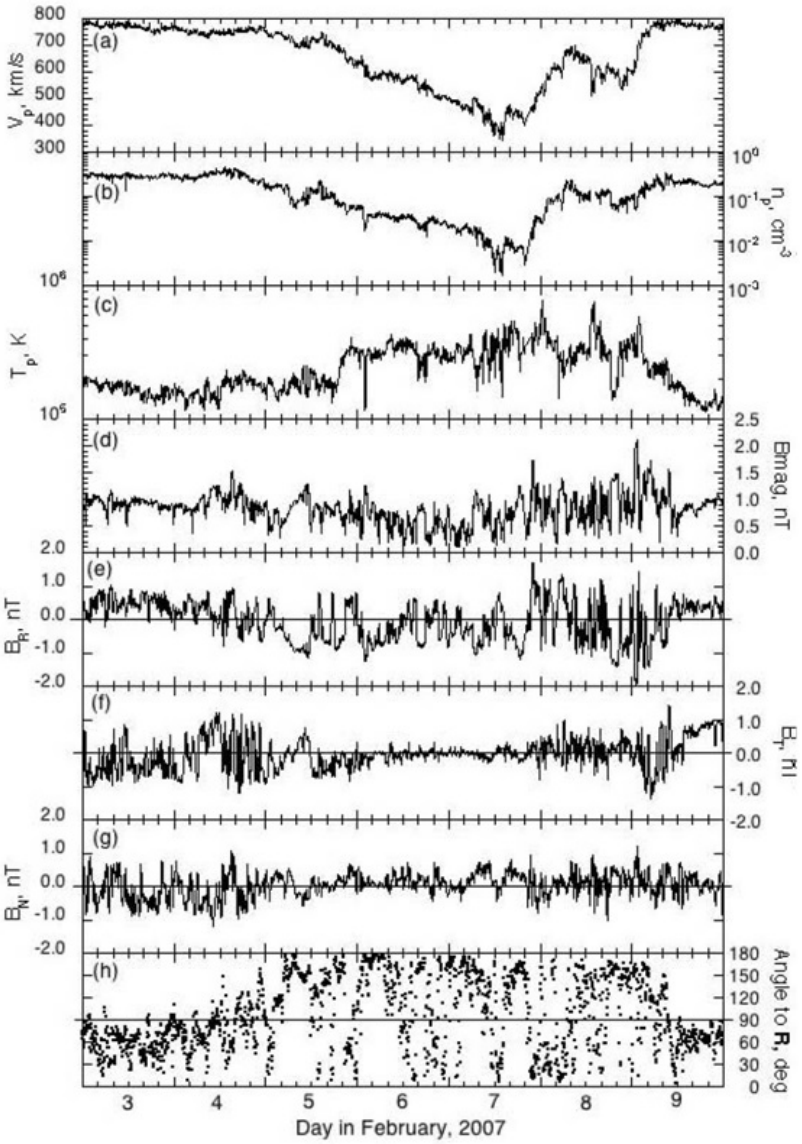

Figure 3.9: The three top panels show the speed, density, and kinetic temperature of protons detected by SWOOPS. The time resolution is 4 or 8 minutes, depending on the spacecraft data rate. Panel d shows the magnitude of the magnetic field, followed by the three components of the vector field, all at 5 minute resolution. The bottom panel displays the angle between the direction of the magnetic field and the outward radius vector from the Sun. From (*Neugebauer et al.*, 2007).

neglected in a model, whether analytical or numerical. In addition, some problems need to consider a realistic comet or solar wind condition or involve plasma instability, rendering it almost impossible to reach an analytic solution. Therefore, 3D global physics-based numerical models have been in demand to study the comet-solar wind

interactions. This section will mainly introduce two types of widely used cometary plasma models: the magnetohydrodynamics (MHD) models and hybrid models.

3.2.1 The single species and single fluid MHD model

The MHD models and many MHD theories are built on the set of equations describing the states of basic physical quantities, i.e., mass density, velocity, pressure/energy and magnetic field in a single species and single fluid plasma shown in Equation. 3.2-Equation. 3.9. The single species and single fluid MHD equations assume that there is only one species of ions and electrons, which can be treated as one quasi-neutral fluid. Other complicated MHD models are generally based on variants of these equations but with fewer assumptions and including more physics.

$$\frac{\partial \rho}{\partial t} + \nabla \cdot (\rho \mathbf{u}) = \frac{\delta \rho}{\delta t} \tag{3.2}$$

$$\rho \frac{d\,\mathbf{u}}{d\,t} - \mathbf{J} \times \mathbf{B} + \nabla P = \frac{\delta \rho \mathbf{u}}{\delta t} \tag{3.3}$$

$$\frac{\partial p}{\partial t} + (\mathbf{u} \cdot \nabla) p + \gamma p (\nabla \cdot \mathbf{u}) = \frac{\delta p}{\delta t} \tag{3.4}$$

$$\nabla \times \mathbf{B} = \mu_0 \mathbf{J} \tag{3.5}$$

$$\nabla \cdot \mathbf{B} = 0 \tag{3.6}$$

$$\frac{\partial \mathbf{B}}{\partial t} = -\nabla \times \mathbf{E} \tag{3.7}$$

$$\nabla \cdot \mathbf{E} = 0 \tag{3.8}$$

$$\mathbf{J} = \sigma(\mathbf{E} + \mathbf{u} \times \mathbf{B}) \tag{3.9}$$

The first three equations are continuity, momentum and pressure/energy equations, which are similar to the equations underlying the neutral gas fluid models but take into account of the effect of the electromagnetic forces. The transportation equa-

tions can also be derived from velocity moments of Boltzmann equations. ρ is the mass density of the ion speices, $\mathbf{U}$ is the velocity vector, and p is the total pressure. $\mathbf{E}$ and $\mathbf{B}$ represent the electric field and the magnetic field respectively. The right hand side of these equations denotes the source terms related to specific chemical or physical processes in the fluid.

The next four equations are the modified Maxwell equations describing the evolution of the electric and magnetic field in the plasma. The temporal variations are assumed to be slow, so the displacement current in the Ampere's law (Equation. 3.5) is neglected. Because the charge neutrality assumption holds for most applications of MHD theory, the net charge density is taken to be 0 and the right hand side of the Gauss' law (Equation. 3.8) is 0. It is not true, if there is a reversal in the magnetic field or a thin layer of current sheet. The last equation is Ohm's law, which is used to complete the system. σ is the electric conductivity, which is assumed to be infinite in ideal MHD. As a result, the Ohm's law can be written as

$$\mathbf{E} + \mathbf{u} \times \mathbf{B} = 0,$$

which gives the profound insight that the magnetic field is frozen in the moving plasma. Detailed derivation can be found in plasma textbooks(e.g., *Gombosi* (1999)).

In arriving at these simplified equations, several assumptions and approximations have been made, many of which also apply to other MHD models we will discuss later. (1) The global length scales should be larger than the ion gyro-radius in order to make the fluid approach valid. (2) The system should be varying slowly so that the high frequency component of electric field can be neglected. (3) The plasma should be quasi-neutral. (4) Viscosity and heat conduction are not considered.

After some manipulation, E and J can be eliminated and the equations can be

written in the conservative form, which are shown in the following equations.

$$\frac{\partial \rho}{\partial t} + \nabla \cdot (\rho \mathbf{u}) = \frac{\delta \rho}{\delta t} \tag{3.10}$$

$$\frac{\partial \rho \mathbf{u}}{\partial t} + \nabla \cdot (\rho \mathbf{u}\mathbf{u} + p\mathbf{I} + \frac{B^2}{2\mu_0}\mathbf{I} - \frac{1}{\mu_0}\mathbf{B}\mathbf{B}) = \frac{\delta \rho \mathbf{u}}{\delta t} \tag{3.11}$$

$$\frac{\partial \mathbf{B}}{\partial t} + \nabla \cdot (\mathbf{u}\mathbf{B} - \mathbf{B}\mathbf{u}) = 0 \tag{3.12}$$

$$\frac{\partial}{\partial t}\left(\frac{1}{2}\rho u^2 + \frac{p}{\gamma - 1} + \frac{B^2}{2\mu_0}\right) + \nabla \cdot \left[\left(\frac{1}{2}\rho u^2 + \frac{\gamma}{\gamma - 1}p + \frac{B^2}{\mu_0}\right)\mathbf{u} - \frac{1}{\mu_0}(\mathbf{B} \cdot \mathbf{u})\mathbf{B}\right] = \frac{\delta E}{\delta t} \tag{3.13}$$

3.2.2 The multi-species model

In this section, we will describe the multi-species MHD model and the source terms used for the cometary plasma simulations. The multi-species model is able to take into account of the chemical reactions occurring among several ion species, which have to share the same momentum and energy equation. The model is appropriate if the differences of ion velocities and ion temperatures are not very significant.

The MHD equations in conservative form for the multi-species model are as follows:

$$\frac{\partial \rho_s}{\partial t} + \nabla \cdot (\rho_s \mathbf{u}) = \mathcal{S}_s - \mathcal{L}_s \tag{3.14}$$

$$\begin{aligned} &\frac{\partial \rho \mathbf{u}}{\partial t} + \nabla \cdot (\rho \mathbf{u}\mathbf{u} + p\mathbf{I} + \frac{B^2}{2\mu_0}\mathbf{I} - \frac{1}{\mu_0}\mathbf{B}\mathbf{B}) = \\ &\sum_{s=ions} \mathcal{S}_s \mathbf{u_n} - \sum_{s=ions} \mathcal{L}_s \mathbf{u} + f_{in}\rho \sum_{t=neutrals} n_t(\mathbf{u_n} - \mathbf{u}) \end{aligned} \tag{3.15}$$

$$\frac{\partial \mathbf{B}}{\partial t} + \nabla \cdot (\mathbf{u}\mathbf{B} - \mathbf{B}\mathbf{u}) = 0 \tag{3.16}$$

$$\frac{\partial}{\partial t}\left(\frac{1}{2}\rho u^2+\frac{p}{\gamma-1}+\frac{B^2}{2\mu_0}\right)+\nabla\cdot\left[\left(\frac{1}{2}\rho u^2+\frac{\gamma}{\gamma-1}p+\frac{B^2}{\mu_0}\right)\mathbf{u}-\frac{1}{\mu_0}(\mathbf{B}\cdot\mathbf{u})\mathbf{B}\right]=$$
$$\frac{1}{2}\left(\sum_{s=ions}\mathcal{S}_s u_n^2-\sum_{s=ions}\mathcal{L}_s u^2\right)-\frac{1}{\gamma-1}\sum_{s=ions}\left(\frac{\mathcal{L}_s}{m_s}\frac{p_i}{n_i}+n_s\alpha_s p_e\right)$$
$$+\frac{1}{\gamma-1}f_{in}\rho\sum_{t=neutrals}n_t(\mathbf{u_n}-\mathbf{u})^2 \tag{3.17}$$

The first is the continuity equation, the second is the momentum equation, the third is the magnetic field induction equation, and the fourth is the energy equation. ρ_s is the mass density of species s, m_s is the mass of ion s, $\mathbf{u}$ the plasma velocity vector, $\mathbf{u_n}$ the neutral velocity vector, $\mathbf{B}$ the magnetic field vector, ρ is the total ion mass density and p is the plasma scalar pressure. $\mathcal{S}_s$ and $\mathcal{L}_s$ are production and loss rates for species s and include photo-ionization, ion-neutral reactions, and electron recombination. The production rate of species s, $\mathcal{S}_s$ can be written as

$$\mathcal{S}_s=\sum_n \nu_{n\to s}\rho_n+\sum_t k_{t+r\to s}n_t n_r m_s,$$

where $\nu_{n\to s}$ is the photo-ionization rate of transforming neutral gas n to ion s, $k_{t+r\to s}$ is the charge exchange reaction rate constant of producing ion s from charge exchange between neutral gas t and the ion r. The loss rate of species s

$$\mathcal{L}_s=\alpha_s n_e\rho_s+\sum_t k_{s+t\to r}n_t\rho_s,$$

where α_s represents (dissociative) ion-electron recombination coefficients for different ion species, n_e is the electron number density, and $k_{s+t\to r}$ represents the rate constant of the charge exchange reaction between the ion species s and the neutral species t. n_i is the total ion number density. f_{in} is the ion-neutral non-reactive friction rate coefficient, which takes the value of $1.7\times10^{-9}\mathrm{cm}^3/\mathrm{s}$ in the cometary plasma context (*Gombosi et al.*, 1996). p_i and p_e are the ion and electron pressures. Here we assume

p_i=p_e=$p/2$. γ=5/3 is the adiabatic index.

3.2.3 The multi-fluid model

The multi-fluid model has separate continuity, momentum, and energy equations for all ion species, so the model is able to resolve more features caused by the physical and chemical processes specific to each species.

The continuity, momenta, and pressure equations for each individual fluid in a multi-fluid model are as follows:

$$\frac{\partial \rho_s}{\partial t} + \nabla \cdot (\rho_s \mathbf{u}_s) = \frac{\delta \rho_s}{\delta t} \tag{3.18}$$

$$\frac{\partial \rho_s \mathbf{u}_s}{\partial t} + \nabla \cdot (\rho_s \mathbf{u}_s \mathbf{u}_s + p_s \mathbf{I}) - Z_s e \frac{\rho_s}{m_s} (\mathbf{E} + \mathbf{u}_s \times \mathbf{B}) = \frac{\delta \rho_s \mathbf{u}_s}{\delta t} \tag{3.19}$$

$$\frac{\partial p_s}{\partial t} + (\mathbf{u}_s \cdot \nabla) p_s + \gamma_s p_s (\nabla \cdot \mathbf{u}_s) = \frac{\delta p_s}{\delta t}, \tag{3.20}$$

where ρ_s,$\mathbf{u}_s$,p_s,γ_s and Z_s are the mass density, velocity, pressure, the adiabatic index, and charge state of ion species s, respectively. $\mathbf{I}$ is the identity matrix, e the unit charge. We can see from the momentum equation that unlike in the single fluid models, different ions species can have separate trajectories because of their decoupled velocities and the difference in the acceleration by the Lorentz force. The electric field can be derived from the electron momentum equation neglecting the inertial term and collisions with ions and neutrals:

$$\mathbf{E} = -\mathbf{u}_e \times \mathbf{B} - \frac{1}{n_e e} \nabla p_e, \tag{3.21}$$

where the electron velocity $\mathbf{u}_e = \mathbf{u}_+ + \mathbf{u}_H$, $\mathbf{u}_+$ is the charge averaged velocity, $\mathbf{u}_+ = \frac{\sum_{s=ions} Z_s n_s \mathbf{u}_s}{n_e}$, and $\mathbf{u}_H$ is the Hall velocity, $\mathbf{u}_H = -\frac{\mathbf{j}}{n_e e}$. The second term on the right hand side of the equation accounts for the effect of the electron pressure gradient ∇p_e. If the pressure gradient is neglected, we have $\mathbf{E} = -\mathbf{u}_e \times \mathbf{B}$, which is similar to

the expression for the "frozen-in" condition in the ideal MHD theory, but indicates the magnetic field is frozen in the electron fluid in this case. To complete the system, Ampere's law and Faraday's law are also needed and the displacement current is neglected in multi-fluid MHD as well as in other MHD models.

$$\mathbf{j} = \frac{1}{\mu_0} \nabla \times \mathbf{B} \tag{3.22}$$

$$\frac{\partial \mathbf{B}}{\partial t} = -\nabla \times \mathbf{E} \tag{3.23}$$

Comparing the number of equations and variables the three MHD models have to solve, the multi-fluid model is the most computationally expensive but has the best capacity of resolving distinguished features of each modeled ion species. The single species model is the most efficient to run but the applicability is limited by many approximations. The multi-species model is a compromise between the multi-fluid and the single-species model. Selection of an appropriate model should mainly depend on the physical problem we want to study. If we want to model the spatial distribution of various species, a multi-species model is necessary. If the target comet is weak and the gyro-motion of proton and heavy cometary ions should be considered, a multi-fluid model or a hybrid model is more appropriate than others. Chapter 7 of this thesis makes a complete study and comparison with comet observations with the multi-species MHD model , but first for completeness the thesis includes brief discussion of two other approaches to the study of cometary plasma: the hybrid model and the multi-fluid MHD model.

3.2.4 Hybrid model

Being able to model kinetic effects and arbitrary ion distributions in the velocity space, such as the pick-up ring distribution of the newborn cometary ions, the hybrid model has a wider applicability than MHD models. The hybrid model represents the

ions with macro-particles whereas the electrons are modeled as a massless fluid. For weak comets at large heliocentric distances, the cometary ion gyroradius is comparable to the length scale of the bow shock or bow wave, under which condition the fluid approximation may not be valid. A hybrid model has been developed by *Bagdonat and Motschmann* (2002) to study the cometary plasma interaction of the Rosetta target comet.

The hybrid code tracks each ion macro-particle in the whole simulation domain and solves the Newtonian equation of motion for each particle:

$$\frac{d}{dt}\mathbf{x}_i = \mathbf{v}_i \tag{3.24}$$

$$\frac{d}{dt}\mathbf{v}_i = \frac{q_i}{m_i}(\mathbf{E} + \mathbf{v}_i \times \mathbf{B}) + \frac{\mathbf{f}}{n_i m_i}. \tag{3.25}$$

q_i,m_i,$\mathbf{x}_i$ and $\mathbf{v}_i$ are the charge, mass, position and velocity of a particle i. $\mathbf{f}$ can be used to model additional physical and chemical process. In the cometary context, it represents the ion-neutral friction,

$$\mathbf{f} = -k_{ni} n_n n_i m_i (\mathbf{v}_i - \mathbf{u}_n), \tag{3.26}$$

where n_n is the neutral density, $\mathbf{u}_n$ is the neutral velocity, and k_{ni} is the ion-neutral friction rate constant between neutral species n and ion species i. The assumptions of massless electron fluid and quasi-neutrality lead to the same equation which can be implemented in the multi-fluid model:

$$\mathbf{E} = -\mathbf{u}_e \times \mathbf{B} - \frac{1}{n_e e}\nabla p_e. \tag{3.27}$$

In addition, the exactly same equations of the Ampere's law and Faraday's law as in the MHD models are used.

However, as other models based on kinetic approach, the hybrid model requires

much more computational resources for the billions of ion particles it has to model. *Rubin et al.* (2014b) found comparable results from the multi-fluid model and a hybrid model on a comet with a very low production rate. They showed that some major features obtained with a hybrid type approach like the gyration of the cometary heavy ions and the formation of the Mach cone can be partially reproduced with the multi-fluid model. The comparison of heavy ion densities and solar wind densities are shown in Fig. 3.10 and Fig. 3.11.

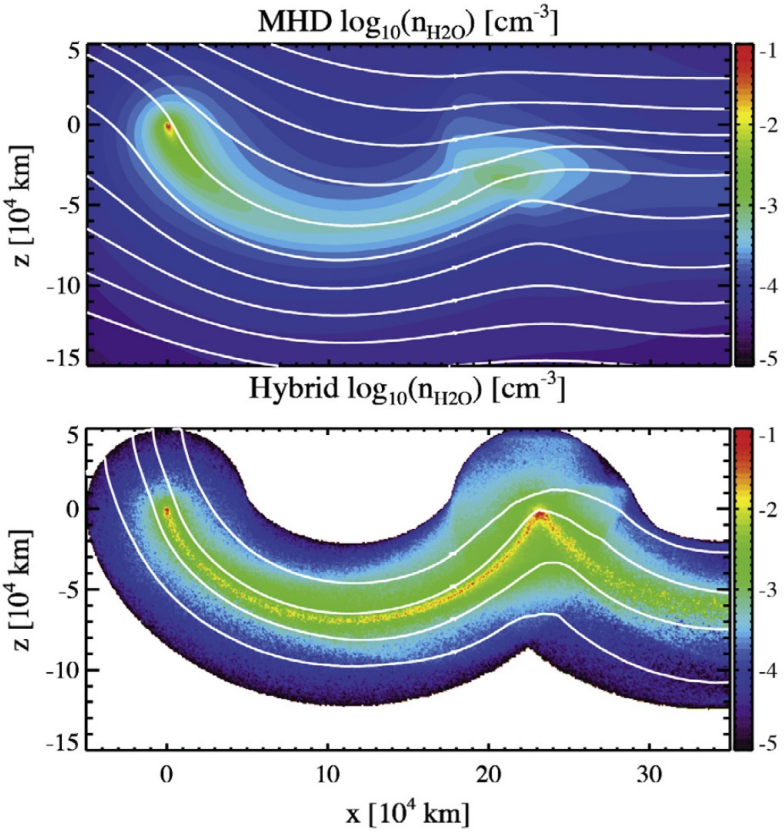

Figure 3.10: Comparison of cometary heavy ion densities and streamlines(white line) from the multi-fluid model (top panel) and the hybrid model (bottom panel). From *Rubin et al.* (2014b).

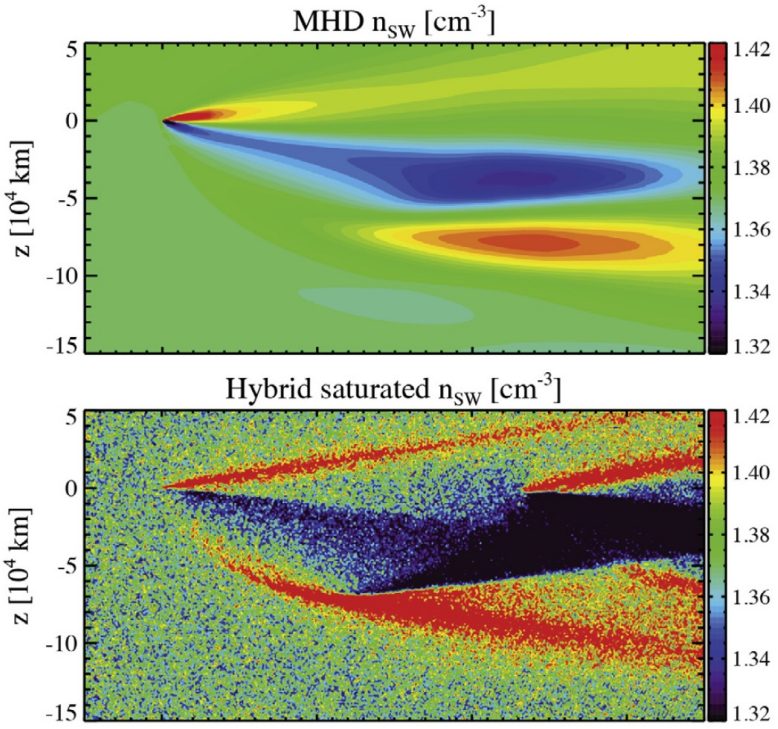

Figure 3.11: Comparison of solar wind densities from the multi-fluid model (top panel) and the hybrid model (bottom panel). From *Rubin et al.* (2014b).

CHAPTER IV

Introduction of cometary dust grains and models

This chapter briefly introduces the dust grain behavior in cometary environments and the important factors needed to interpret observations. The strength and weakness of existing dust models are discussed and the newly developed multi-fluid dust model is introduced as well.

4.1 Introduction

Dust and gas in comets are believed to have preserved the building material of the early solar system. Unfortunately, it is not feasible to study the composition of dust and gas in a large number of comets by remote observations. As the apparent dust-to-gas ratio is easier for remote and in-situ observations and is no less critical to our understanding of the formation of the solar system, models that are able to interpret the dust observations and can better constrain this quantity are desirable.

Dust grains prevail in cometary environments and have various compositions (i.e. water ice, SiO_2, Mg, Fe). The size of dust grains ranges from sub-micron to meters and affects the behavior of dust grains. For example, millimeter-sized grains reflect light more efficiently than the micron-sized. Smaller grains can be accelerated by gas more efficiently because of higher surface to mass ratio. Since one type of observation or one instrument covers only part of the size range, a reasonable estimation of the size

distribution is needed to obtain the total dust loss rate or the dust-to-gas production ratio. However, the problem can be more complicated, as grains' fragmentation and sublimation may also alter the size distribution.

When it comes to interpreting the dust observations, more factors come into play. Since dust grains are subjected to the gas drag, the gas activity must be taken into account. Therefore, heterogeneity on the rotating nucleus surface with the variation of solar illumination can lead to a complex dust behavior. Depending on the sum of the gas drag and the gravity of the comet, some dust grains may escape with the gas, some orbit around the nucleus, some fall back to the surface. When the escaping dust grains are far from the comet, they may encounter anti-sunward radiation pressure and get pushed back toward the nucleus. On comet 103P/Hartley 2, sublimating icy grains serve as an extended source, supplying most water gas in the coma (*Fougere et al.*, 2012). The initial velocity of the gas just sublimated from the grains tend to be slower than ambient gas which has already been accelerated. Since the dust grains often have a higher temperature than the ambient gas, the sublimated gas can also heat the coma. Consequently, the extended dust grains can greatly alter the velocity and temperature profile of the coma.

In addition, dust grains can also get charged by photo-electrons generated by solar radiation at the surface, impact from ions and electrons in the solar wind, and electron attachment. Charged dust grains are subject to an additional force caused by the electromagnetic field in the cometary plasma. In some cases, the electromagnetic force can become the dominant factor and thus the charged dust is more similar to ions in plasma than other neutral dust grains. The collective behavior of charged dust can be very complicated. As a result, all kinds of dust grains populate the cometary environment, making it challenging to understand the observational data.

In this thesis, we will focus on the neutral dust grains and the charged dust is not considered. Several models have been developed to study the neutral dust-

gas interaction, which can be divided into two groups. One group treats the gas and dust as fluids and solves Euler equations or Navier-Stokes equations for density, velocities and pressure (e.g. *Kitamura* (1986);*Crifo* (1995)); the other one represents them with particles and keeps track of velocities and locations of each particle, the statistics of which can also provide the same macro-quantities as fluid models. Direct Simulation Monte Carlo (DSMC) method is one example among the second group and has demonstrated its advantages over fluid models in studying dust grains' behavior (*Tenishev et al.* (2011), *Marschall et al.* (2016)), because (1) it is able to model a continuous spectrum of dust sizes, while fluid models can only do several discrete sizes; (2) it can model dust grain trajectories crossing each other but fluid models cannot. However, when it comes to simulating time-dependent three dimensional phenomena of large length scales, fluid models can be more computationally feasible than DSMC models.

In this chapter, we developed a cometary dust model, which not only has key features of fluid dust models, but also applies a newly developed numerical mesh to resolve the irregular shape of the nucleus and to accommodate the rotating nucleus.

4.2 General dust model

Given the same total mass production rate of dust grains, different number density distributions of the grain size can result in large differences in total number densities, total sublimation rate and other quantities that are sensitive to size. A power law is often used to describe the size distribution function in cometary dust grain observations and models:

$$f(a) \sim a^s \tag{4.1}$$

where a is the radius of the grain and s is the power-law index. We should also note here the size distribution function $f(a)$ is different from the number density as

a function of size $n(a)$, but

$$f(a) \sim \frac{d\,n(a)}{da}. \tag{4.2}$$

Therefore, $f(a) \sim a^s$ is identical to $n(a) \sim a^{s+1}$ if the total dust mass is fixed. s often takes a value less than -1, which indicates the smaller sized dust grains have a larger population.

In many models, dust grains are treated as spherical particles. Taking into account the gas drag, the gravitational force from the nucleus, and the radiation pressure, the governing equation of the particle motion can be written as follows (*Weigert*, 1959; *Gombosi et al.*, 1986):

$$\frac{4}{3}\pi a^3 \rho_d \frac{d\mathbf{v_d}}{dt} = \pi a^2 \frac{C_d}{2} \rho_g (\mathbf{v}_g - \mathbf{v}_d)|\mathbf{v}_g - \mathbf{v}_d| - \rho_d \mathbf{g}_n + \beta \frac{4}{3}\pi a^3 \rho_d \frac{GM_s}{r_h^2} \frac{\mathbf{r}_h}{r_h} \tag{4.3}$$

where ρ_d is the mass density of an individual dust grain, ρ_g is the gas mass density; $\mathbf{v}_g$ and $\mathbf{v}_d$ are the gas velocity and dust velocity, respectively; G is the gravitational constant, M_s is the mass of sun, $\mathbf{r}_h$ is the position vector with respect to the sun. The first term on the right hand side represents the gas drag effect. C_d is the drag coefficient that can be approximated by 2.(*Gombosi et al.*, 1986) The second term is the nucleus gravitational force, and $\mathbf{g}_n$ is the gravitational acceleration caused by the nucleus at the location of the particle. The third term gives the effect of the solar radiation pressure, and β is the ratio of the radiation pressure force to the solar gravitational force. The value of β can be found in *Burns et al.* (1979) and *Mukai et al.* (1989), which is often less than 1. If the particle equation is applied to the grains at the nucleus surface and the radiation pressure is neglected, we are able to obtain the size of the maximum liftable particles, which will be discussed in Chapter 7.

4.3 Multi-fluid dust model

Our multi-fluid dust model is based on the BATS-R-US (Block-Adaptive Tree Solar wind Roe-type Upwind Scheme) code (*Powell et al.*, 1999; *Tóth et al.*, 2012) in the Space Weather Modeling Framework (SWMF) developed by the University of Michigan. It treats H_2O gas and dust grains of 6 sizes ranging from 10^{-7}m to 10^{-2}m as different fluids. Each fluid has its own continuity equation and momentum equation, which are almost the same as the equations 2.16-2.18 in the multi-fluid neutral gas model. However, unlike gases, solid dust grains do not have energy equations, though they do have grain temperature normally calculated from thermal equilibrium with sun light. If the model is limited to the vicinity of the comet, within a distance less than 500 km to the nucleus, the photo-dissociation process of H_2O and the radiation pressure are neglected. Since our target, comet 67P/ChuryumovGerasimenko (CG) has a low production rate, the heating effect of dust grains on the gas energy balance is not included either (*Crifo et al.*, 2005). But the effect of gas drag is taken into account by introducing corresponding source terms to the momentum equations of dust grains. The source term can be expressed as $n_{dust}\pi a^2 \frac{C_d}{2}\rho_{H_2O}(\mathbf{u}_{H_2O} - \mathbf{u}_{dust})|\mathbf{u}_{H_2O} - \mathbf{u}_{dust}|$, It can be obtained by multiplying the gas drag term in the equation of the particle motion by the dust number density n_{dust}. Because of conservation of momentum, the same source term should be subtracted from the source term of H_2O. When the model is running in the co-rotating frame, the centrifugal and Coriolis forces are also included.

If the sublimating grains should be taken into account, the following source terms are needed:

$$R_{\rho_{d_i}} = -4\pi a_{d_i}^2 f_{d_i} n_{d_i} \tag{4.4}$$

$$L_{\rho_{d_i}} = -4\pi a_{d_i}^2 f_{d_i} n_{d_i} \frac{a_{d_i}^3}{a_{d_i}^3 - a_{d_{i-1}}^3} \tag{4.5}$$

$$L_{\rho_{d_1}} = -4\pi a_{d_1}^2 f_{d_1} n_{d_1} \tag{4.6}$$

$$S_{\rho_{d_i}} = 4\pi a_{d_{i+1}}^2 f_{d_{i+1}} n_{d_{i+1}} \frac{a_{d_i}^3}{a_{d_{i+1}}^3 - a_{d_i}^3} \tag{4.7}$$

$$\frac{\delta \rho_{d_i}}{\delta t} = S_{\rho_{d_i}} + L_{\rho_{d_i}} \tag{4.8}$$

$$\frac{\delta \rho_{H_2O}}{\delta t} = -\sum_i \frac{\delta \rho_{d_i}}{\delta t} \tag{4.9}$$

$$\frac{\delta \rho_{d_i} \mathbf{u}_{d_i}}{\delta t} = S_{\rho_{d_i}} (\mathbf{u}_{d_{i+1}} - \mathbf{u}_{d_{i+}}) + \frac{\delta \rho_{d_i}}{\delta t} \mathbf{u}_{d_i} \tag{4.10}$$

$$\frac{\delta \rho_{H_2O} \mathbf{u}_{H_2O}}{\delta t} = -\sum_i Sub_{\rho_{d_i}} \mathbf{u}_{d_i} \tag{4.11}$$

$$\frac{\delta p_{H_2O}}{\delta t} = -\sum_i R_{\rho_{d_i}} (\frac{kT_{d_i}}{m_{H_2O}} + \frac{1}{3}(\mathbf{u}_{H_2O} - \mathbf{u}_{d_i})^2) \tag{4.12}$$

where d_i represents the i-th dust fluid, and the dust with larger index has a larger size, i.e. radius $a_i < a_{i+1}$; ρ_{d_i}, $\mathbf{u}_{d_i}$, T_{d_i} are the mass density, velocity, temperature of dust fluid i, while m_{H_2O}, ρ_{H_2O}, p_{H_2O}, $\mathbf{u}_{H_2O}$ are the molecular mass, mass density, velocity, and pressure of H_2O. f_{d_i} is the sublimating rate of dust fluid i, and gives the mass of the sublimated gas produced per unit area in unit time. f_{d_i} and T_{d_i} only depend on the size of the particle and the heliocentric distance. An example of the sublimation rate and the equilibrium temperature is shown in Fig. 4.1. The first equation gives the dust mass density loss rate for the i-th dust $R_{\rho_{d_i}}$, which is proportional to the product of the sublimation rate times the surface area of dust particles. The second equation shows that the sublimation not only converts the icy grains into water, but also reduces the size of the original dust particle. Therefore, part of the i-th dust fluid becomes the (i-1)-th, which results in more loss for d_i than sublimation only can cause and generating more d_{i-1} particles. In the model there is an upper limit and a lower limit for the dust size. The mass loss rate for the smallest particle equals the sublimation rate. The largest particle cannot be produced by particles of other sizes

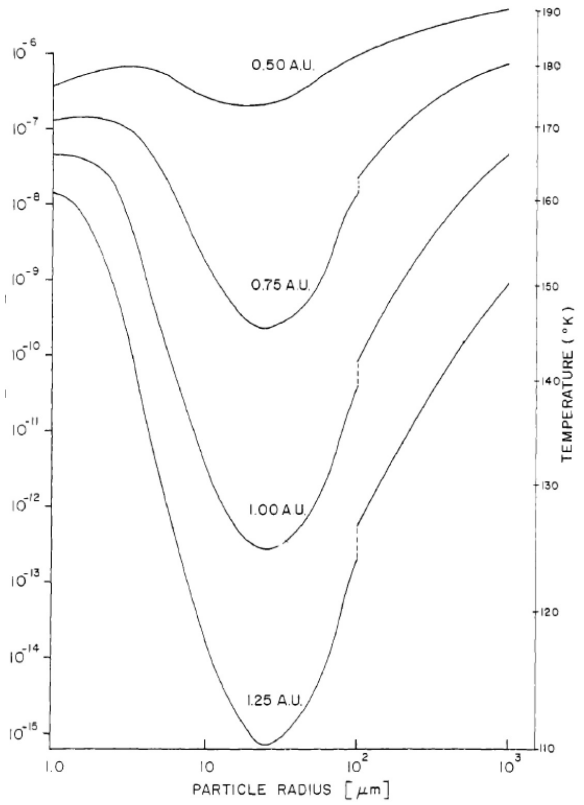

Figure 4.1: Sublimation rates and equilibrium temperatures of pure icy grains. From *Patashnick and Rupprecht* (1975).

and is generated by the nucleus. $\frac{\delta \rho_{d_i}}{\delta t}$ and $\frac{\delta \rho_{H_2O}}{\delta t}$ are the source terms for continuity equations of all fluids. We can also tell from the source terms for the momentum equations that though the water gains mass and momentum from sublimation, the average bulk water velocity decreases because of the slower moving dust.

4.3.1 The "roundcube" mesh

There are two ways to study the effect of cometary rotation in a numerical simulation. One way is running the model in the inertial frame and rotating the nucleus. However, every time when the nucleus is rotated, the location of the nucleus surface or the inner boundary has to be re-calculated, which is very time-consuming. So we choose to run the model in the cometary rotating frame so that the nucleus and the computational mesh is fixed relative to the grid, which is computationally efficient and convenient. The radial flow from the nucleus in the inertial frame should show a spiral pattern in the rotating frame. If a Cartesian computational domain was used, both outflow and inflow would occur at the outer boundary. The upstream of the inflow is out of the computational domain and the information exchange is cut off by the boundary, which can be seen near the edge of the inner box in Fig. 4.2. It is impossible to set the boundary condition appropriately without knowing the upstream condition of the inflow first. The issue can be solved if a spherical grid is used, in which there is only outflow at the outer boundary as Fig.4.2 shows and a floating boundary condition can be readily applied. However, spherical grid have very small cells near the axis and it is also more complicated to use for the real shaped nucleus than a Cartesian grid. Therefore, a new mesh named "roundcube" is developed, the inner part of which is a normal Cartesian cube and the outer surface is a smooth sphere. The cells between the spherical surface and the cube are stretched, which can be seen in the 2D cut of the mesh in Fig.4.2. A simple version of the "roundcube" grid was originally implemented into the Versatile Advection Code (*Tóth*, 1996), and

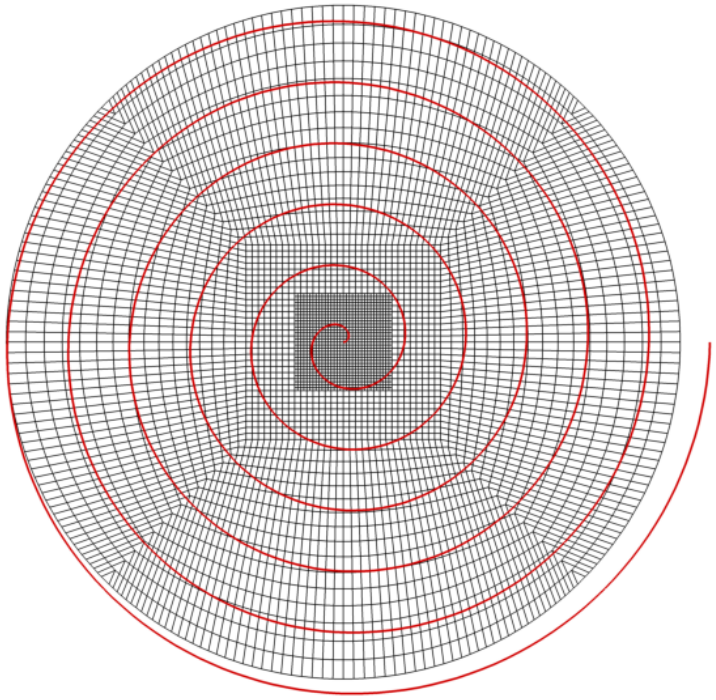

Figure 4.2: 2-D cuts of the "roundcube" mesh with the red line showing a spiral pattern of outflow

later it was independently discovered and extensively generalized by *Calhoun et al.* (2008).

A point (ξ, η, ζ) of generalized coordinates can be transformed to a point (x, y, z) of Cartesian coordinates on a roundcubed mesh by a multiplier W: $(x, y, z) = W(\xi, \eta, \zeta)$. Two parameters are needed to calculate the multiplier, r_0 and r_1, which are L1 distances of the inner box and outer box of the Cartesian grid from the origin, respectively. W can be calculated by the following process.

$$a = \frac{d_1 - r_0}{r_1 - r_0};$$

$$b = min(1, max(0, a));$$

$$W = 1 + b\left(\frac{d_1\sqrt{3}}{d_2} - 1\right),$$

where a and b are temporary variables, d_1 and d_2 are the L1 and L2 distance of (x, y, z), respectively. By inspecting the formula, we can find the cells inside the inner box are not stretched. The surface of the outer box is inflated into a spherical surface. For points along the principal axes on the surface, W is $\sqrt{3}$. For points along the diagonals, $W = 1$. It implies the radius of the sphere is $\sqrt{3}$ times of r_1. This mesh will be used in the application of the dust model in Chapter 8.

CHAPTER V

Implementation of the numerical models

The hydrodynamic models and MHD models developed in this work are based on the Block Adaptive-Tree Solar wind Roe-type Upwind Scheme (BATS-R-US) code (*Powell et al.*, 1999) of the Space Weather Modeling Framework (SWMF) of University of Michigan (*Tóth et al.*, 2005, 2012). The governing equations of the models are solved by the BATS-R-US code on an adaptive mesh, which is able to resolve the different length scales that cover orders of magnitude and avoid the waste of computing resource on some regions of little interest. An example of the adaptive mesh for cometary solar wind interaction is shown in Fig.5.1. The code can also be executed on parallel machines, which facilitate large scale simulations. This chapter will briefly introduce the time stepping approaches and the method often used to speed up the convergence of the code.

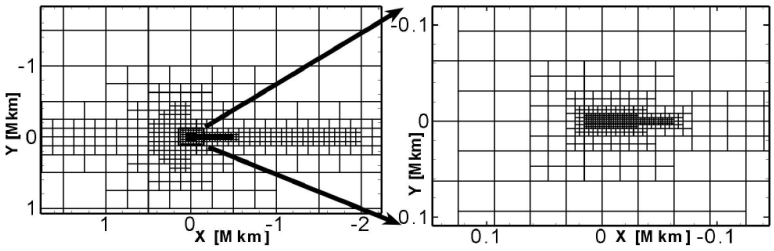

Figure 5.1: An example of the adaptive mesh for cometary solar wind interaction.

5.1 Time stepping approaches

Depending on the manner in which the time derivative in a partial diffrential equation (PDE) is discretized, there are mainly two types of time stepping approaches: explicit and implicit. The explicit time stepping scheme can be written as

$$\mathbf{U}_i^{n+1} = \mathbf{U}_i^n + \Delta t \mathbf{R_i}(U^n), \tag{5.1}$$

where $\mathbf{U}_i$ is the vector of state variables, Δt_i is the time step for grid cell i. $\mathbf{R}_i$ is the discretized right hand side of the PDE $\partial U/\partial t = \mathbf{R}(\mathbf{U})$. The time step of explicit scheme is limited by the Courant-Friedrichs-Lewy (CFL) condition that is necessary to achieve numerical stability. The CFL condition requires $\left(\frac{u_x}{\Delta x} + \frac{u_y}{\Delta y} + \frac{u_z}{\Delta z}\right)\Delta t < 1$ on a 3D Cartesian grid for instance, where $u_{x,y,z}$ is the fastest characteristic speed in x,y,z direction and $\Delta_{x,y,z}$ are the cell sizes in x,y,z directions.

In some applications, the explicit scheme is not appropriate if the equations contain stiff source terms, such as chemical reactions, photo-ionization, which may restrict the time step to be much smaller than what is practical in a simulation. If the stiff source does not contain spatial derivatives, the point-implicit scheme can be used. The point-implicit scheme uses a split approach and first does an explicit update without the stiff source terms.

$$\mathbf{U}^{n+1/2} = \mathbf{U}^n + \frac{\Delta t}{2}\mathbf{R}_{expl}(\mathbf{U}^n), \mathbf{U}^* = \mathbf{U}^n + \Delta t \mathbf{R}_{expl}(\mathbf{U}^{n+1/2}), \tag{5.2}$$

where $\mathbf{R}_{expl}$ is the non-stiff source term.

Then the source term $\mathbf{S}_{impl}^{n+1}$ is represented by $\mathbf{U}_{impl}^{n+1}$, the variables related to the stiff source terms and $\mathbf{U}_{expl}^*$, the variables that are not affected by the stiff terms. So

we have

$$\mathbf{U}_{impl}^{n+1} = \mathbf{U}_{impl}^{*} + (1-\beta)\Delta t \mathbf{S}_{impl}(\mathbf{U}^{*}) + \beta \Delta t \mathbf{S}_{impl}(\mathbf{U}_{expl}^{*}, \mathbf{U}_{impl}^{n+1}), \tag{5.3}$$

which is first order in time for β=1 and second order in time for $\beta = 1/2$. Expanding the source term around time level * and keeping the first order term, the last equation is linearized,

$$\mathbf{U}_{impl}^{n+1} = \mathbf{U}_{impl}^{*} + \Delta t \mathbf{S}_{impl}(\mathbf{U}^{*}) + \beta \Delta t \frac{\partial \mathbf{S}_{impl}}{\partial \mathbf{U}_{impl}} (\mathbf{U}_{impl}^{n+1} - \mathbf{U}_{impl}^{*}). \tag{5.4}$$

This equation can be solved for $\mathbf{U}_{impl}$ cell-by-cell by inverting an N_{impl} by N_{impl} matrix, where N_{impl} is the size of $\mathbf{U}_{impl}$. In the BATSRUS code, the Jacobian matrix $\frac{\partial \mathbf{S}_{impl}}{\partial \mathbf{U}_{impl}}$ can be calculated numerically, but it involves computing the source terms for N_{impl}+1 times, which may be costly for a large N_{impl} or complicated source terms. The analytic form of the matrix can also be entered by the developer for the sake of efficiency.

In some cases, the whole system is stiff and the time step is too small for a feasible simulation. For example in the magnetosphere simulations near the Earth, because the Alfven speed is order 30000 km/s, while the speed of the actual dynamics is about 10$\sim$100 km/s. The point-implicit scheme does not work for such a stiff system due to the spatial derivatives in the stiff terms, but the fully-implicit scheme can increase the time step significantly. The disadvantage of the fully-implicit scheme is that it needs to invert a large matrix, which makes it much more computationally expensive than other schemes for one time step. More details can be found in *Tóth et al.* (2012).

5.2 Time-accurate vs. steady-state

Time accurate simulations are able to study cometary problems of time varying nature, such as instabilities, dynamics caused by variations of the solar wind or activity on the comet or rotation of the nucleus. In time accurate simulations, every cell often takes the same step, which is determined by the minimum time step in the whole computational domain, if the explicit or point-implicit time stepping scheme is used. However, it is inefficient if the global time step is much too small compared with the local time step determined by the CFL condition in the cell. One way to speed up the code is subcycling, which enables different cells take a different number of time steps to get to the same time level.

In addition, if the boundary conditions are not changing, a system may have a steady-state solution, which will not vary after a period of relaxation time. If such a solution exists, a steady-state simulation can be run to achieve the final state in fewer steps than the time accurate simulations. In steady-state simulations, the local time stepping method is used, in which every cell can take the maximum possible local time step to speed up the convergence to the steady-state solution. Before the code reaches the final state, transient results are probably not physical.

In the simulations in Chapter 6, Chapter 7 and Section 8.2.1, as the boundary conditions are fixed and are not varying with time, the steady-state method is applied to achieve convergence to the solution faster. In Section 8.2.2, the boundary condition on the surface of the nucleus is governed by solar illumination and changes as the nucleus rotates. As a result, a steady-state solution is not likely to exist. Therefore, in order to study the effect of rotation and the activity of a comet, the time-accurate method has to be used.

CHAPTER VI

A study of kinetic effects and variations of physical conditions in the cometary coma

6.1 Introduction

In Chapter 2, we have introduced the new 3D multi-fluid model, which treats H_2O, OH, H_2, O, and H as separate fluids and each fluid has its own density, velocity, and temperature. Photo-chemical reactions and collisions are included. Collisions between fluids allow different gases to exchange momentum and energy. The collision frequency is proportional to the gas densities and and collision cross sections of both interacting species, so the model is able to address the heating efficiency issue in a self-consistent way that before was only able to do with particle kinetic models. In the following section, we compare our results on comet 67P/Churyumov-Gerasimenko with that from a DSMC model (*Tenishev et al.*, 2008). In addition, the fluid approach is computationally efficient enough to be able to be applied to more complicated time-dependent problems and not limited to steady-state solutions. We demonstrate that despite the various approximations, the multi-fluid model is able to produce generally similar results as the DSMC approach on a large length scale up to 10^6 km, which makes it a useful and computationally less demanding alternative to the particle approach. Finally, we present a more general study of the effects of the production

rate on the expansion speed and the temperature of H_2O, which we then compare with radio telescope observations of over 30 comets from *Tseng et al.* (2007).

6.2 Methodology

6.2.1 Model description

The underlying equations and source terms are described in Section 2.2.3. The photo-chemical reactions, reaction rates, and the corresponding excess energies used in this chapter are shown in Table 6.1.

Table 6.1: Chemical reactions and corresponding parameters

Wavelength(Å)	Reaction	Reaction rate (s^{-1})	Excess energy (eV)
1357-1860	$H_2O+h\nu \rightarrow H+OH$	8.0×10^{-6}	1.7
	$H_2O+h\nu \rightarrow H_2+O$	8.4×10^{-8}	1.7
1216	$H_2O+h\nu \rightarrow H+OH$	8.0×10^{-6}	4.5
	$H_2O+h\nu \rightarrow H_2+O$	2.8×10^{-7}	1.7
984-1357 (excluding 1216)	$H_2O+h\nu \rightarrow H+OH$	3.6×10^{-7}	4.5
	$H_2O+h\nu \rightarrow H_2+O$	4.8×10^{-8}	1.7
<984	$H_2O+h\nu \rightarrow$ ionization products	7.0×10^{-7}	
2160	$OH+h\nu \rightarrow H + O$	4.5×10^{-6}	0.36
2450		5.0×10^{-7}	0.67
1400-1800		1.4×10^{-6}	3.2
1216	OH ($1^2\Delta$)	3.0×10^{-7}	3.8
	OH ($B^2\Sigma^+$)	5.0×10^{-8}	1.6
	OH ($2^2\Pi - 3^2\Pi$)	5.0×10^{-8}	3.8
<1200	OH ($D^2\Sigma^-$)	1.0×10^{-8}	2.7
	$H_2+h\nu \rightarrow H+H$	1.1×10^{-7}	1.8

The cross sections for the modeled collisions are also listed in Table 6.2. We note here that cross-sections of self-collisions are not included, since fluid approaches

assume an approximately Maxwellian distribution for each fluid, implying plenty of self-collisions in the gas of the species.

Table 6.2: Cross Sections of Collisions for Major Components in the Comae

Component	Cross Section (cm^{-2})	Component	Cross Section (cm^{-2})
H_2O-OH	3.2×10^{-15}	H_2O-H_2	3.2×10^{-15}
H_2O-H	1.8×10^{-15}	H_2O-O	1.8×10^{-15}
OH-H_2	3.0×10^{-15}	OH-H	1.5×10^{-15}
OH-O	1.5×10^{-15}	H_2-H	1.5×10^{-15}
H_2-O	1.5×10^{-15}	H-O	1.2×10^{-15}

Our model is based on the BATS-R-US (Block-Adaptive Tree Solar wind Roe-type Upwind Scheme) code (*Powell et al.*, 1999; *Tóth et al.*, 2012), which is capable of solving the magnetohydrodynamics (MHD) and hydrodynamics equations efficiently on adaptive grids. The simulations are performed on a 3D spherical grid, the radius of which is 1.4×10^6 km for the comet 67P case. A spherical body with a radius of 2 km is placed at the origin to model the comet nucleus. We note here that a realistic nucleus radius of comets with a production rate higher than $10^{30}\,s^{-1}$ should be more than 20 km. However, as our model shows for comets with high production rates, a realistic radius does not change the results at cometocentric distances larger than 50 km. The resolution in the radial direction is about 370 meters near the nucleus and about 1.2×10^5 km near the outer boundary of the computing domain. The resolutions in the polar and azimuthal directions are about 0.7 and 1.4 degrees, respectively. This grid allows studying the coma in different length scales but without too heavy of a computational burden. In addition to the adaptive grid, two features in the BATS-R-US code also greatly improve the efficiency and accuracy of the model. The first is the steady state mode, where the time steps are different in every grid cell limited by

the local stability condition only, so that the time to the convergence is reduced. The second is the point-implicit scheme (*Tóth et al.*, 2012), which facilitates the calculation of the stiff source terms, which are mainly related to the photo-chemistry in the coma without spatial derivatives involved. For example, during a single computational time step, one minor species may have a density so tiny that it may be comparable to the incremental density added by the photochemical reactions. An explicit scheme cannot compute such terms efficiently and accurately, but the point-implicit scheme can handle them well.

6.2.2 Boundary conditions

To compare our results with the DSMC results (*Tenishev et al.*, 2008), we run the model to simulate comet 67P at four heliocentric distances with the same or as consistent a set of parameters as possible between fluid and kinetic models. The inner boundary condition on the surface of the nucleus for the only parent species, water, is fixed. H_2O flux F and H_2O temperature T are set as functions of the solar zenith angle, which is described by *Tenishev et al.* (2008). Following *Huebner and Markiewicz* (2000) and *Bieler et al.* (2015), the magnitude of the H_2O velocity u on the surface is $0.8257\sqrt{8kT/(\pi m)}$, where k is the Boltzmann constant and m is the molecular mass of H_2O. The velocity is normal to the surface. The number density is calculated by $F/|u|$. The pressure at the boundary is set to be $(F/u)k(0.9049T)$. For all other species, the photo-dissociation products of water, a floating boundary condition is set for all variables, in which a zero gradient is imposed. At the outer boundary, floating boundary conditions are also applied for all variables.

In section 6.3.2, we study the effects of production rates on the coma morphology, so the inner boundary conditions are slightly modified. The flux is set to be uniform on the surface and the temperature is fixed to 180 K. The heliocentric distances are fixed to 1.0 AU for all cases and we only vary the neutral gas production rate from 10^{27}

to $10^{30}\,s^{-1}$ in these simulations and results are compared with the hybrid-fluid-kinetic calculations of *Bockelee-Morvan and Crovisier* (1987).

To compare with remote observations of several comets, we run more cases with varying heliocentric distances and different production rates, and obtain the expansion speed of H_2O at about 10^5 km from the nucleus. The distance is chosen mainly because the expansion speeds reported by *Tseng et al.* (2007) were measured approximately at that distance.

6.3 Results and discussion

6.3.1 Comparison with the DSMC model

2-D cuts of densities, speeds, and temperatures of H_2O and H from the multi-fluid model results at 1.3 AU are shown in Fig. 6.1. The sun is in the direction of negative x-axis. The effect of solar illumination can be seen from the H_2O results. Density, speed, and temperature of H_2O are higher on the dayside than the nightside. But it is not true for H. Because of more collisions taking place on the dayside, the dayside speed and temperature of H are lower. Also, because of the large ejection speed when H atoms are produced from the photo-dissociation of H_2O and OH many H atoms are sprayed directly into the nightside hemisphere. The similar picture to H applies to other daughter species.

In this section, we will juxtapose our model results and the DSMC solution, and display the similarities and the differences between them. Specifically, the 1-D profiles of velocities, temperatures, and densities of modeled species extracted along the comet-sun line are compared. Such comparisons are made at four heliocentric distances: 1.3 AU, 2.0 AU, 2.7 AU, and 3.3 AU with production rates of 5×10^{27}, 8×10^{26}, 8×10^{25}, and $1\times10^{24}\,s^{-1}$, respectively.

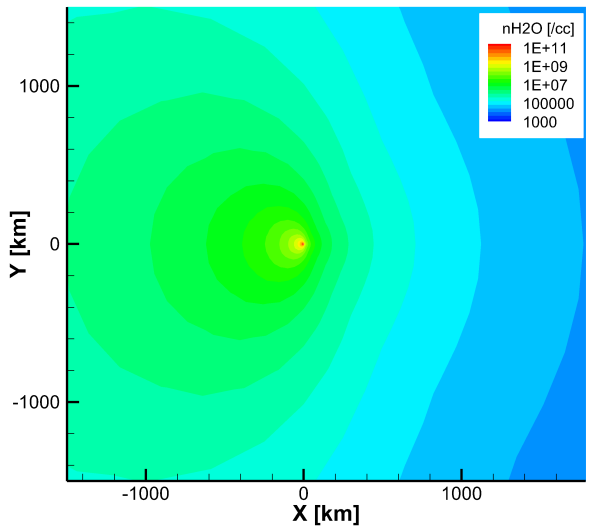
nH2O [/cc]
1E+11
1E+09
1E+07
100000
1000
1000
0
-1000
Y [km]
-1000
0
1000
X [km]

(a)

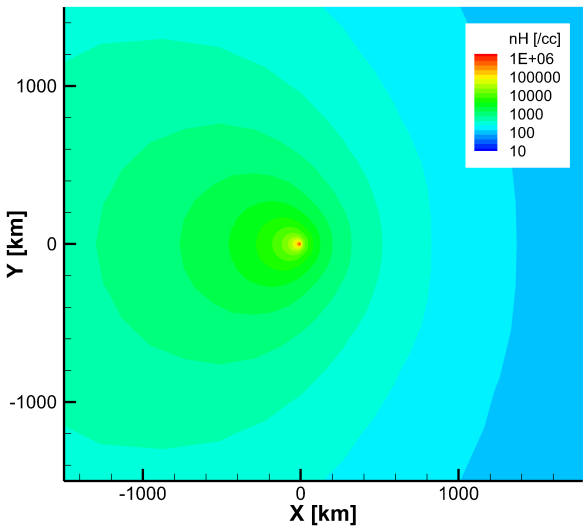
nH [/cc]
1E+06
100000
10000
1000
100
10
1000
0
-1000
Y [km]
-1000
0
1000
X [km]

(b)

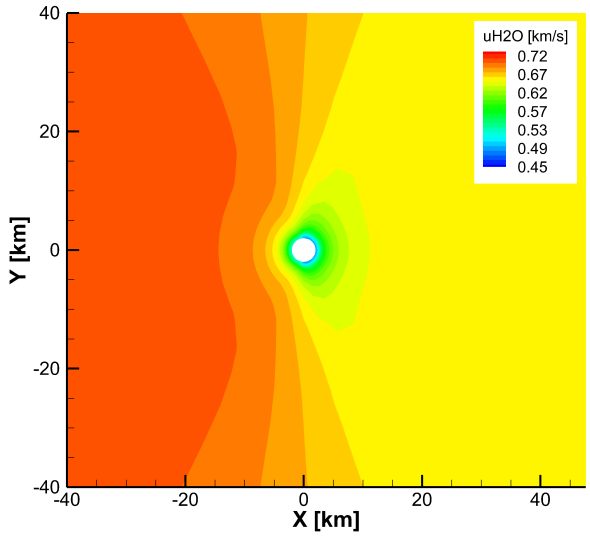
uH2O [km/s]
0.72
0.67
0.62
0.57
0.53
0.49
0.45
40
20
0
-20
-40
Y [km]
-40
-20
0
20
40
X [km]

(c)

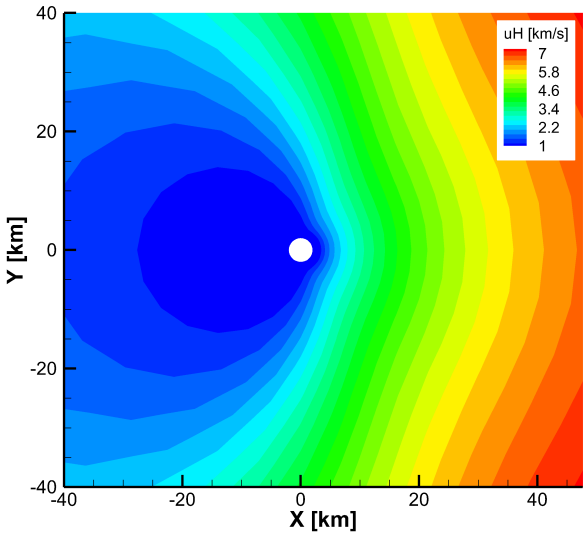
uH [km/s]
7
5.8
4.6
3.4
2.2
1
40
20
0
-20
-40
Y [km]
-40
-20
0
20
40
X [km]

(d)

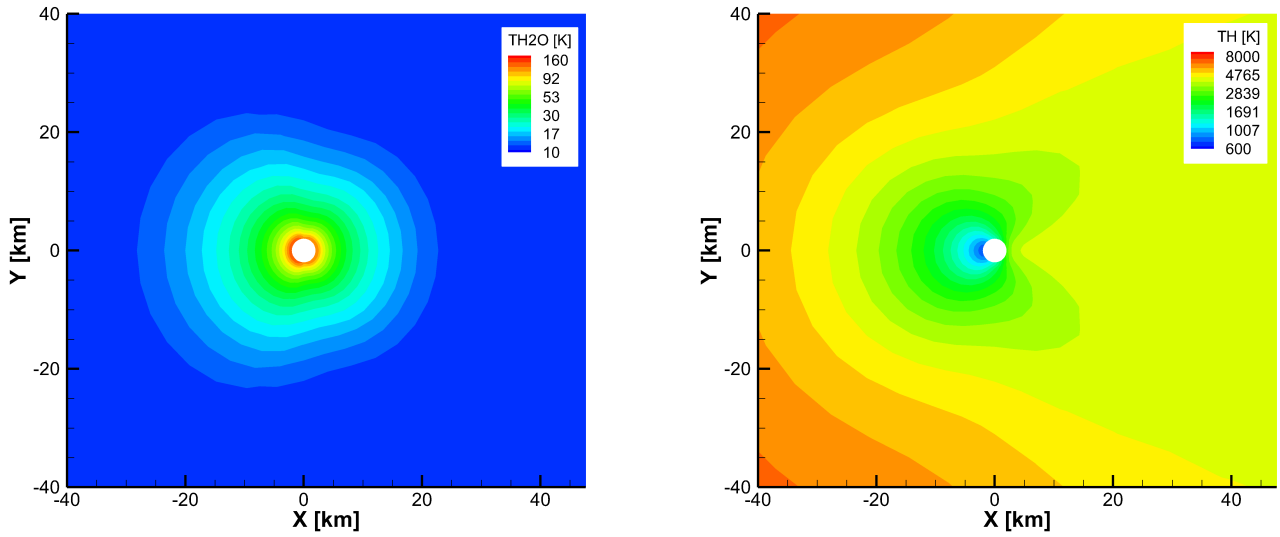

(e) (f)

Figure 6.1: 2-D cuts of the model results at 1.3 AU with a production rate of $5\times10^{27}\,s^{-1}$. Three rows represent densities, speeds, and temperatures of H_2O (left column) and H (right column). The sun is in the direction of the negative x-axis.

6.3.1.1 Velocity

Fig. 6.2 shows the speed of each species at four heliocentric distances, with the left column displaying our fluid model results and the right column the DSMC results from *Tenishev et al.* (2008). The following figures of temperatures and densities have the same format. We can spot three groups of lines in the four cases in both columns. H and H_2 behave as one group, while O and OH are another one. Each group has similar masses, and gains energy from the photo-dissociation. The group of H and H_2 has the highest speeds, the group of O and OH is the second. H_2O almost stays level after a short distance of acceleration, with collisions with daughter species as its only source for acceleration. The speeds of H and H_2 are decoupled from H_2O before O and OH diverge from H_2O at a larger distance. The decoupling distance decreases with lower production rates. This trend can be readily explained by fewer collisions in a thinner coma and more excess energy translated to the kinetic energy. Therefore,

as production rate decreases, H and H_2 reach the plateau of the bulk speed at about 5 km/s in a shorter distance, resulting in a steeper slope in the velocity profile.The new fluid and DSMC kinetic results are quite similar in all respects.

6.3.1.2 Temperature

Fig. 6.3 displays temperatures for all species at the selected four heliocentric distances. The temperature behavior can also be divided into the three groups mentioned in the previous section. H and H_2 have the highest temperatures. OH and O are intermediate. Without any excess energy input, H_2O is the coldest. The temperature of H_2O decreases due to the adiabatic expansion at distances less than 100 km, then remains at the level of around 10 K. For cases with larger production rates, the temperatures of H, H_2, O, and OH first drop slightly before increasing to high levels. As the drops are mainly caused by the collisions with the cold H_2O, the lack of collisions for the cases with low production rates leads to the disappearance of the dips.

We also notice that temperatures of all daughter species decline at large distances. This may be attributed to two possible reasons. The first is the cooling effect caused by adiabatic expansion. The second reason is that the relative abundance of the parent species to the daughter species decreases farther out. As a result, the percentage of newly born daughter species with a high photo-dissociation temperature drops in the population of the daughter species. Also, because of the heat exchange between the daughter species and the water gas, the bulk temperature of the daughter species is thus decreased. Later we will show the relative abundance of the parent species to the daughter species also decreases faster at smaller heliocentric distances due to the shorter photo lifetime of the parent species, which explains why in the 1.3 AU case the temperatures of daughter species drop most quickly.

The most obvious difference between our fluid model and the DSMC model is the decreasing rate of the water temperature. In the fluid model results, the water

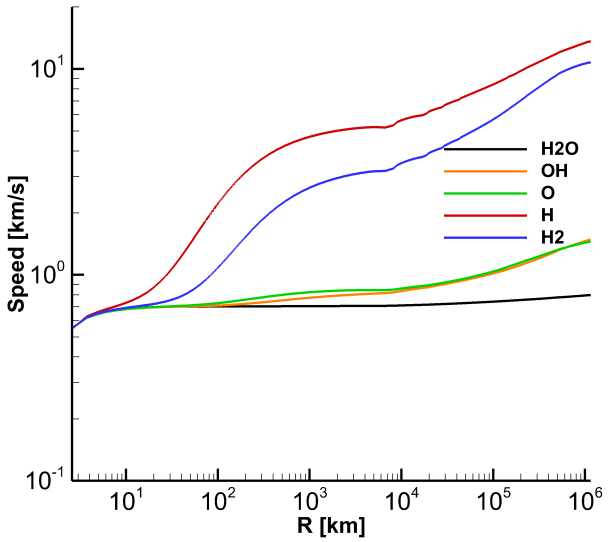
Speed [km/s]
R [km]
H2O
OH
O
H
H2

(a)

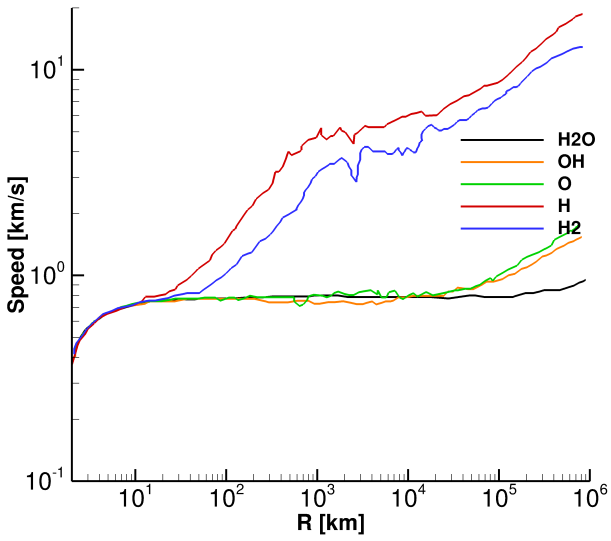
Speed [km/s]
R [km]
H2O
OH
O
H
H2

(b)

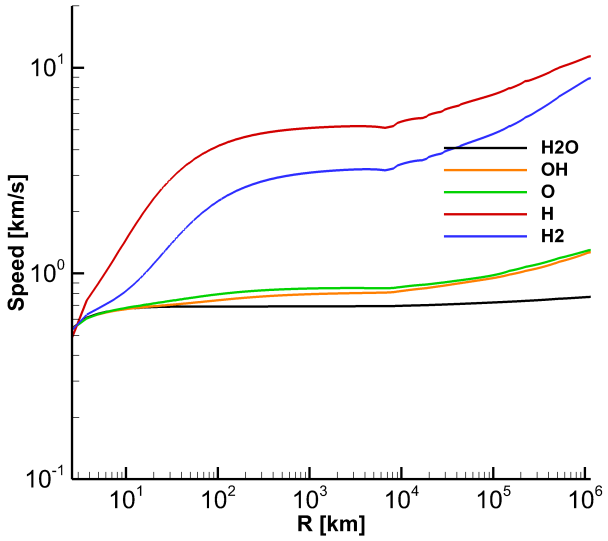
Speed [km/s]
R [km]
H2O
OH
O
H
H2

(c)

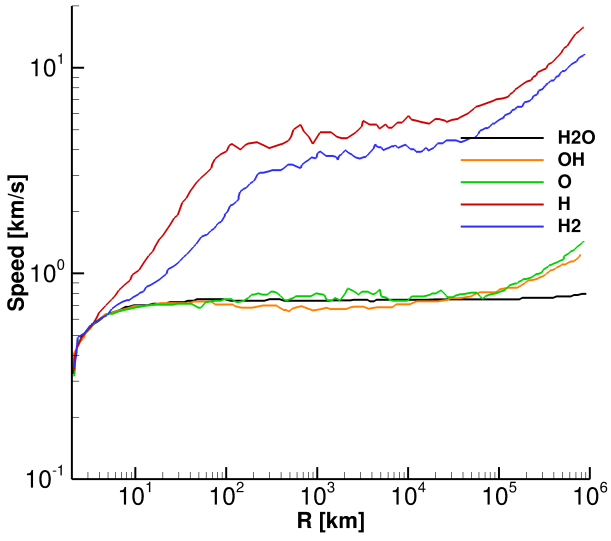
Speed [km/s]
R [km]
H2O
OH
O
H
H2

(d)

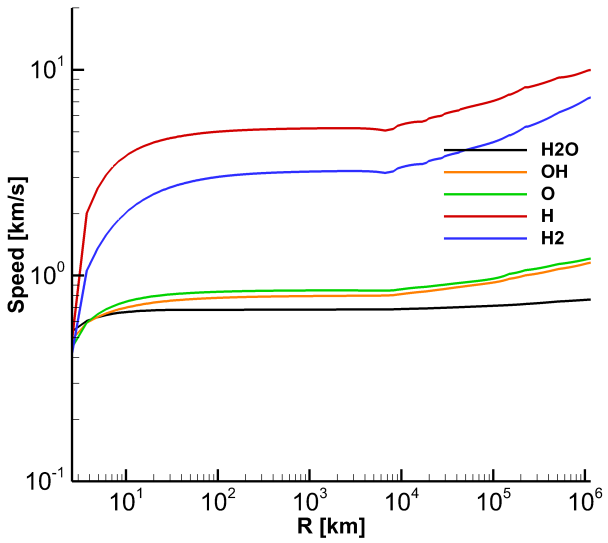

(e)

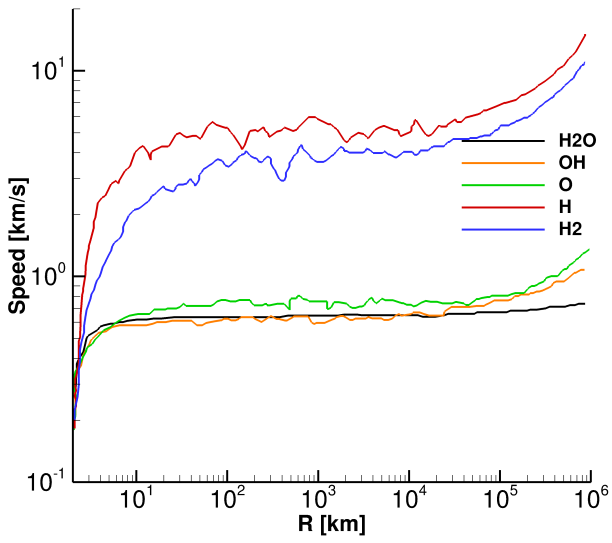

(f)

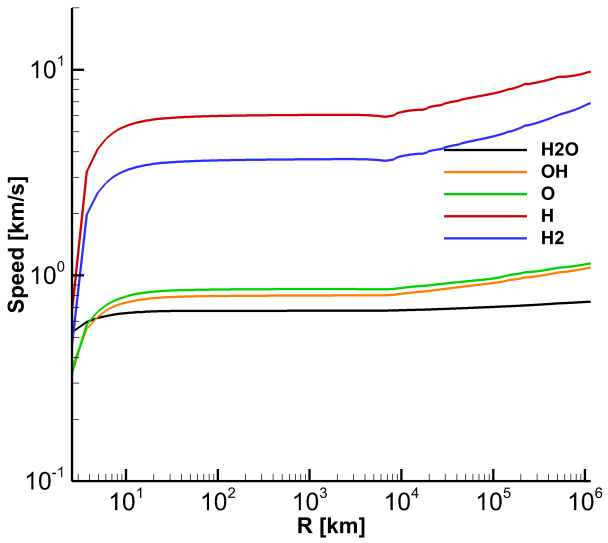

(g)

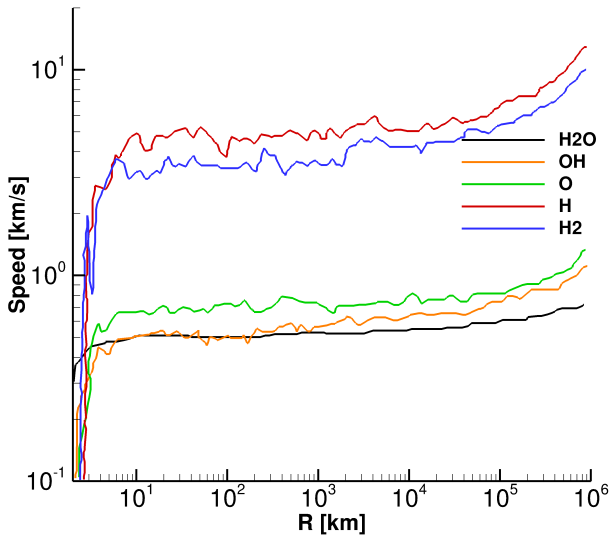

(h)

Figure 6.2: Speeds of modeled species versus distances from the body. Four rows represent results for four heliocentric distances: 1.3 AU, 2.0 AU, 2.7 AU and 3.3 AU. The production rates are 5×10^{27}, 8×10^{26}, 8×10^{25}, and $1\times10^{24}\,\mathrm{s}^{-1}$, respectively. The left column shows our fluid model results and the right column shows the results reproduced from *Tenishev et al.* (2008)

.

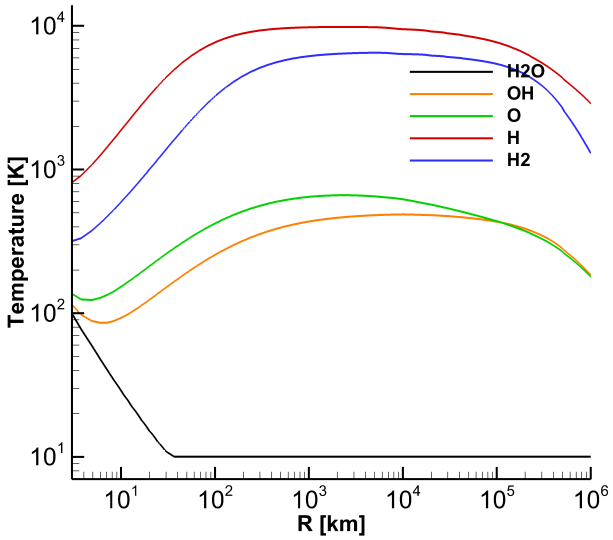
Temperature [K]
R [km]
H2O
OH
O
H
H2

(a)

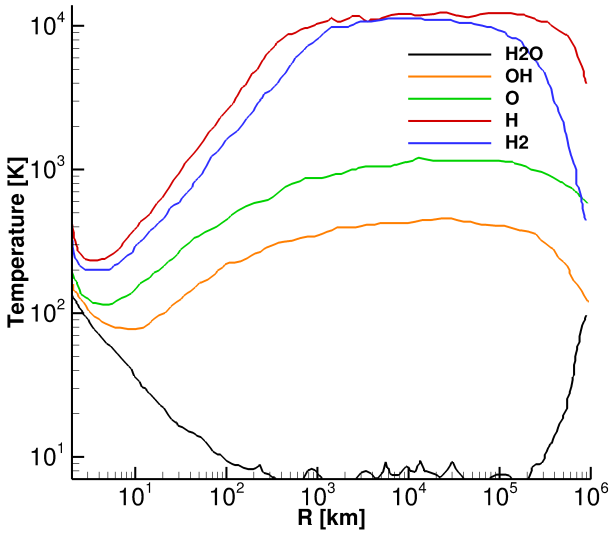
Temperature [K]
R [km]
H2O
OH
O
H
H2

(b)

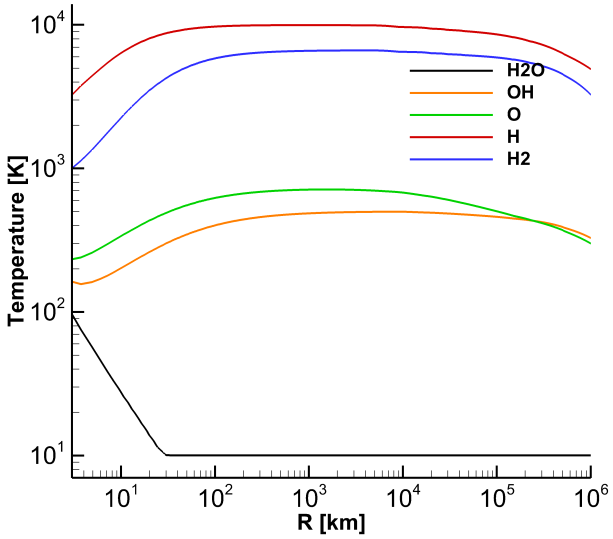
Temperature [K]
R [km]
H2O
OH
O
H
H2

(c)

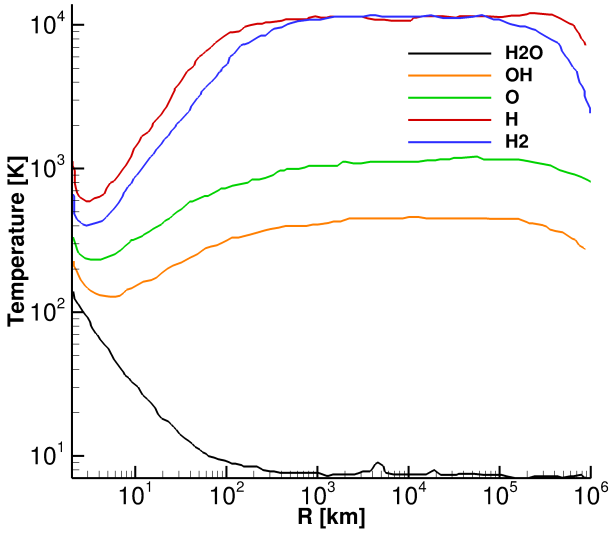
Temperature [K]
R [km]
H2O
OH
O
H
H2

(d)

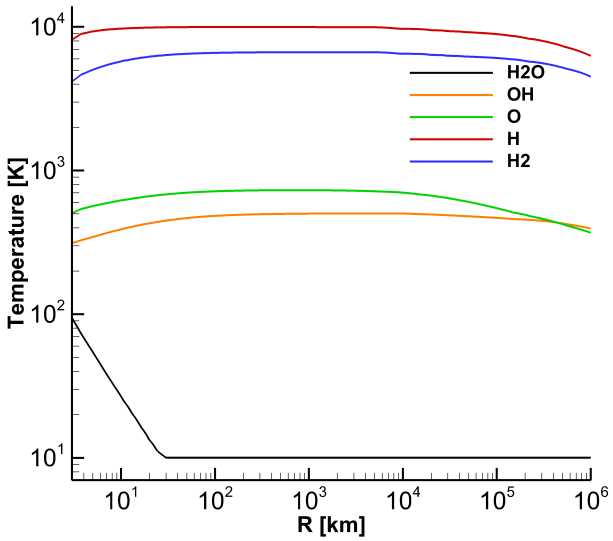

(e)

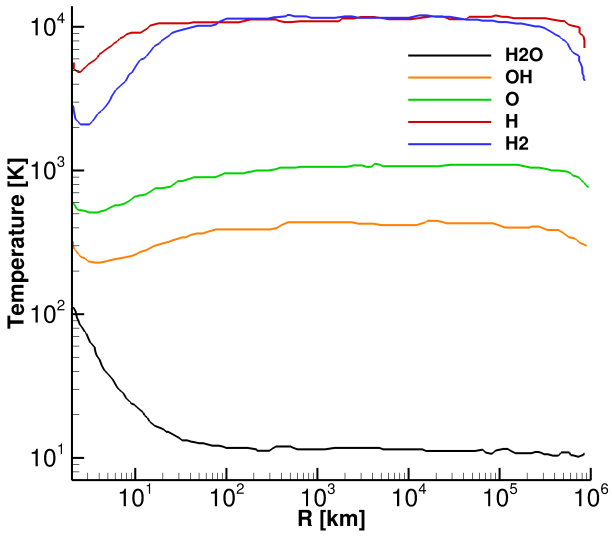

(f)

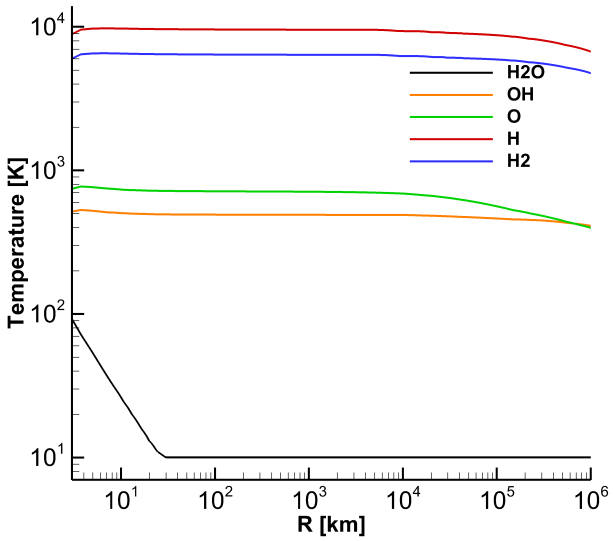

(g)

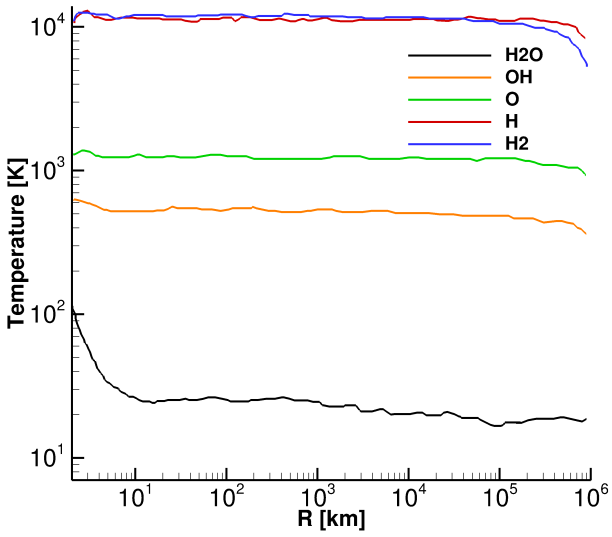

(h)

Figure 6.3: Temperatures of modeled species versus distances from the body. Four rows represent results for four heliocentric distances: 1.3 AU, 2.0 AU, 2.7 AU and 3.3 AU. The production rates are 5×10^{27}, 8×10^{26}, 8×10^{25}, and $1\times10^{24}\,\mathrm{s}^{-1}$, respectively. The left column shows our fluid model results and the right column shows the results reproduced from *Tenishev et al.* (2008)

.

temperature decreases to the minimum temperature of 10 K within 20 km for all four cases. But the slopes in the DSMC results are flatter, especially in the cases of 1.3 AU and 2.0 AU with the minimum temperature reached at 100 km. This may be caused by the fluid model overestimating the self collisions, so adiabatic expansion happens more efficiently than in the DSMC which yields less frequent collisions.

It is interesting to see in the DSMC results that the H_2O temperature jumps to about 100 K near 10^6 km in the 1.3 AU case. According to *Tenishev et al.* (2008), this is caused by the selection effect. Most of the slower H_2O particles have already been destructed by photo-dissociation. We can also see that in the velocity plot, close to 10^6 km the water velocity goes up significantly. Due to the nature of the fluid approximation, our model is not able to include such purely kinetic effects related to distribution functions.

6.3.1.3 Density

Fig. 6.4 presents the densities of all species versus the cometocentric distances. The two columns look similar. H_2O decreases the fastest, since it gets photo-dissociated at a high rate without any new supply. In the cases at 1.3 AU and 2.0 AU, we can see H and OH have the same density near the nucleus and diverge after some distances. The explanation is that they are initially produced by the same chemical reaction and they share the same velocity in the collisional region. Outside the collisional region, freshly produced fast H dominates compared with slower OH. As a result, the H density declines faster. In other cases, where even in the vicinity of the nucleus is collisionless, the H density is lower than OH all the way out. The same reasoning also applies to H_2 and O.

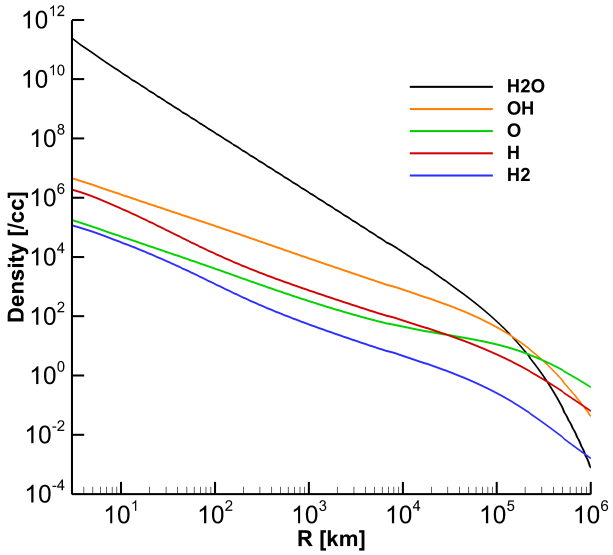
H2O
OH
O
H
H2
Density [/cc]
R [km]

(a)

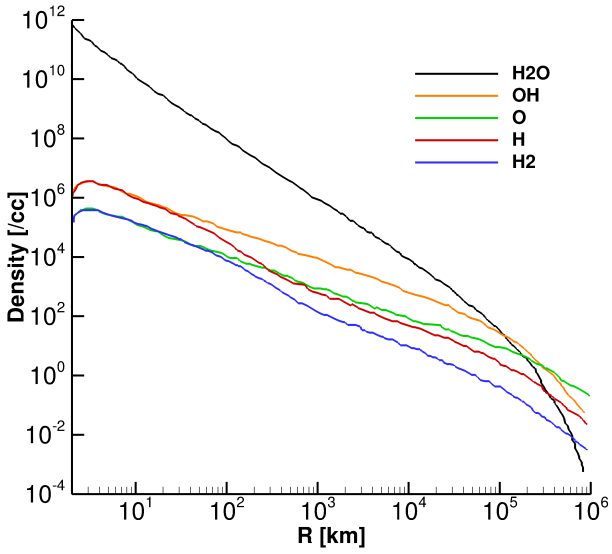
H2O
OH
O
H
H2
Density [/cc]
R [km]

(b)

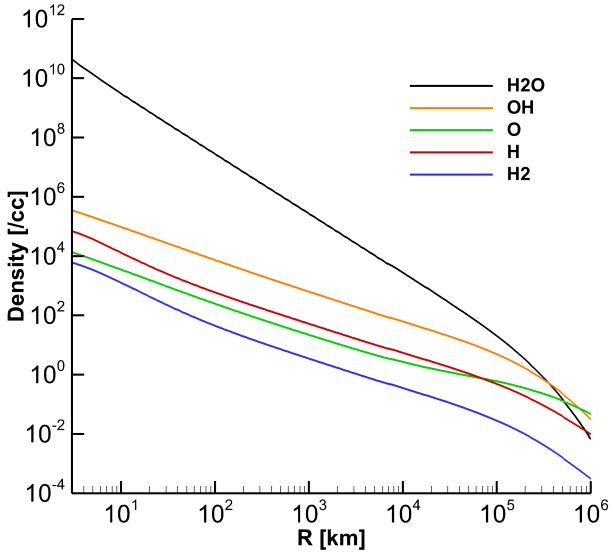
H2O
OH
O
H
H2
Density [/cc]
R [km]

(c)

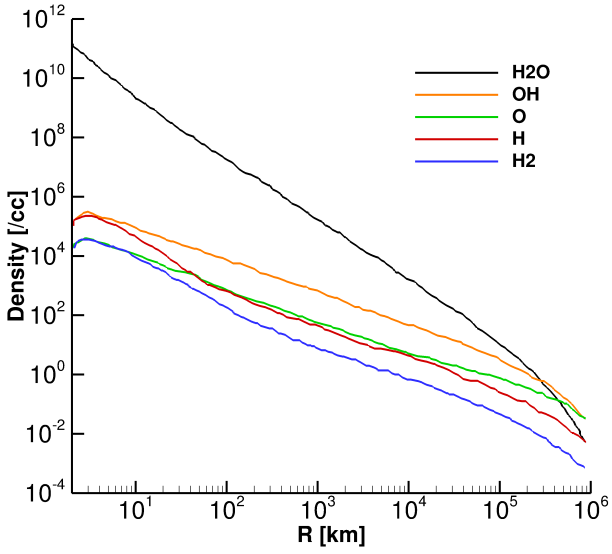
H2O
OH
O
H
H2
Density [/cc]
R [km]

(d)

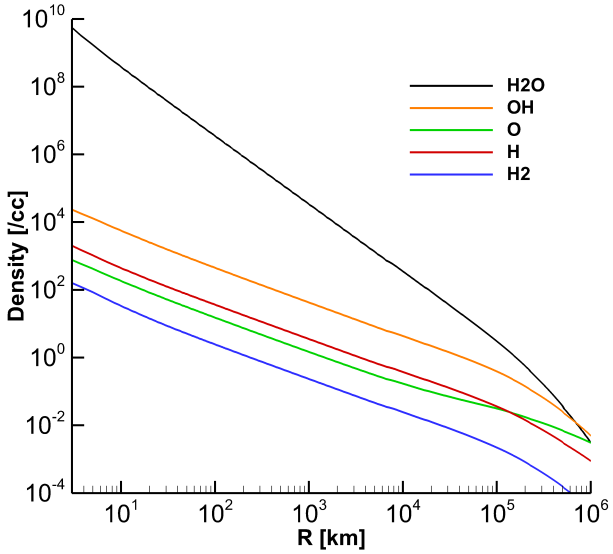

(e)

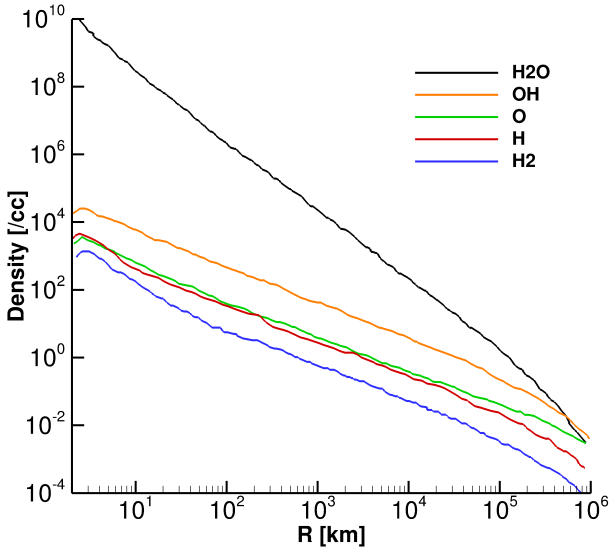

(f)

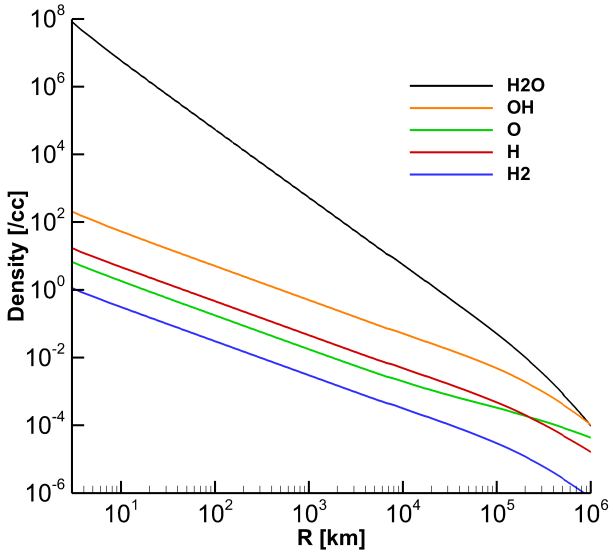

(g)

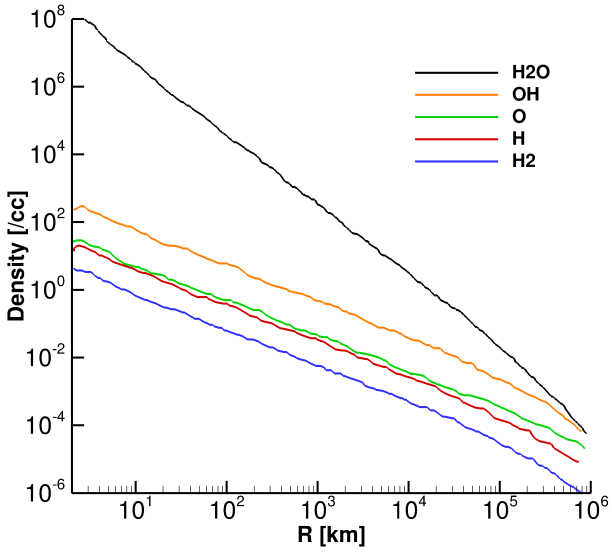

(h)

Figure 6.4: Densities of modeled species versus distances from the body. Four rows represent results for four heliocentric distances: 1.3 AU, 2.0 AU, 2.7 AU and 3.3 AU. The production rates are 5×10^{27}, 8×10^{26}, 8×10^{25}, and $1\times10^{24}\,\mathrm{s}^{-1}$, respectively. The left column shows our fluid model results and the right column shows the results reproduced from *Tenishev et al.* (2008)

.

6.3.2 The effect of production rates

To study the effects of the production rate on coma dynamics, we run the model at 1.0 AU but with four different production rates: 10^{27}, 10^{28}, 10^{29} and $10^{30}\,\mathrm{s}^{-1}$. Fig. 6.5 shows for all four cases the speed of water, the mean speed of the three heavy species (H_2O, OH, O), and the mean speed of all 5 neutral species. The 10^{27} and $10^{28}\,\mathrm{s}^{-1}$ cases are very similar in the speed profile, suggesting the role of collisional heating is negligible with a low production rate or a low density. The water terminal speed in the 10^{27} and $10^{28}\,\mathrm{s}^{-1}$ cases is 0.7 km/s, which is mainly determined by the initial temperature. As the production rate increases, the collisional heating effect kicks in. In the $10^{29}\,\mathrm{s}^{-1}$ case, the water speed at 10^5 km is 0.9 km/s and it rises to about 1.4 km/s in the $10^{30}\,\mathrm{s}^{-1}$ case. This result also agrees well with *Bockelee-Morvan and Crovisier* (1987), who calculated this using a 1D fluid model for water and a Monte Carlo model for the heating from hot H atoms. In the other two plots, we find the mean speed accelerates beyond 10^4 km because of the contributions by the fast species. As a result, the increase of the production rate has more impact on water speed than the bulk speeds of heavy species and all combined species.

Fig. 6.6 shows the temperature of H_2O, the mean temperatures of three heavy species (H_2O, OH, O), and the mean temperatures of all 5 neutral species for the four cases. In the H_2O temperature profile, there is a peak beyond 10^4 km in the cases of 10^{29} and $10^{30}\,\mathrm{s}^{-1}$ production rates. The general trend is similar to that in *Bockelee-Morvan and Crovisier* (1987). But the specific peak values are slightly different between our model and theirs. In the $10^{30}\,\mathrm{s}^{-1}$ case, our peak near 140 K is higher than the peak at 110 K in their model. It may be because their model is single-fluid and treats photo-chemical heating and radiative cooling in a different way than ours. In the $10^{29}\,\mathrm{s}^{-1}$ case, both models have roughly the same peak near 45 K. The temperatures in the other two plots all have dips within 1000 km but then the upward trend remains beyond 1000 km. Though the temperatures of the four cases increase

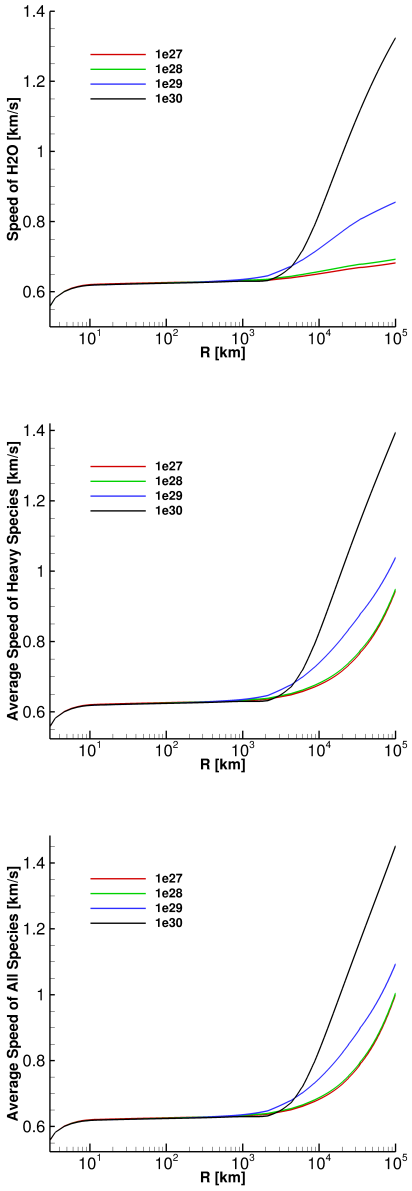

Figure 6.5: The speed profile of H_2O, the mean speed profile of three heavy species (H_2O, OH, O), and the mean speed profile of the 5 neutral species at 1.0 AU. The four different colors denote four production rates: 10^{27}, 10^{28}, 10^{29} and $10^{30}\,s^{-1}$.

at different rates, they are close to each other around 10^5 km. This suggests that, when the cometocentric distance is large enough, the average temperature of all gases may not vary much with the production rate. At large cometocentric distances all species become collisionally decoupled and the secondary species trend to the photo-production temperatures, which are independent of the production rates. Fig. 6.5

and Fig. 6.6 illustrate the radiative cooling effect on the speed and the temperature of water. Within 1000 km, in the $10^{30}\,s^{-1}$ case, because the most significant cooling effect is caused by the highest water density, the speed and temperature are dampened for a larger distance than those in other cases.

Fig. 6.7 shows the mean molecular mass versus the cometocentric distance for varying production rates. Since the comet in this study is kept at a heliocentric distance of 1.0 AU and has H_2O as its only parent species, the four cases yield very similar curves. The difference in the speed profiles is the only factor capable of altering the relative abundances and thus the mean molecular mass. We can expect if all species have fixed speed profiles for each individual species, the four cases should have the same mean molecular mass profile. We also notice that the mean molecular masses at 10^5 km almost converge to a single value of about 15.4 amu.

6.3.3 Comparison with remote observations

In this section, we characterize the cometary H_2O expansion speeds extracted from our multi-fluid gas coma model at a cometocentric distance of 10^5 km for comparison with large field of view velocity resolved radio observations of OH. The model is run with several selected production rates and heliocentric distances. The results are listed in Table 6.3. One can readily see from the table that a larger production rate and a smaller heliocentric distance (i.e., a higher photon flux) lead to a higher expansion speed as expected (*Combi*, 1987).

Tseng et al. (2007) derived the H_2O expansion speeds from the 18-cm line shapes of the OH radicals observed by radio telescopes in over 30 comets, which is reproduced in Fig. 6.8 and serves as benchmark for our model. Our model results, which are denoted by solid diamonds, are superimposed on the observations. We note here the x-axis in Fig. 6.8 represents the OH production rate, which is often obtained by multiplying a factor of 0.86, the photo-dissociation branching ratio of H_2O to OH, with the H_2O

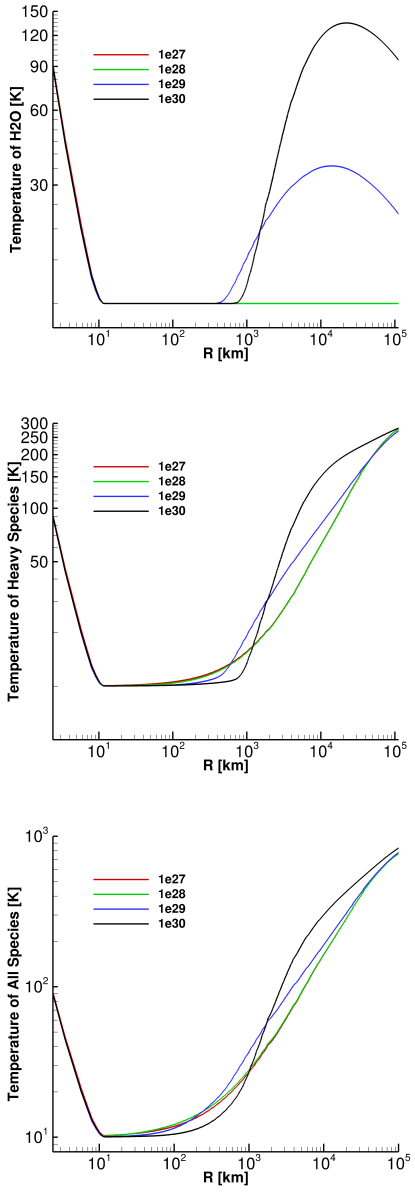

Figure 6.6: The temperature profile of H_2O, the mean temperature profile of three heavy species (H_2O, OH, O), and the mean temperature profile of the 5 neutral species at 1.0 AU.The four different colors denote four production rates: 10^{27}, 10^{28}, 10^{29}, and $10^{30}\,s^{-1}$.

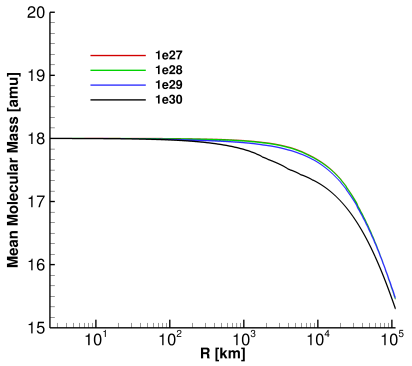

Figure 6.7: The mean molecular mass profiles of four production rates at 1.0 AU. The four colors denote four production rates: 10^{27}, 10^{28}, 10^{29}, and $10^{30}\,\mathrm{s}^{-1}$.

Table 6.3: H_2O expansion speeds

Heliocentric distance(AU)	H_2O production rate (s^{-1})		
	10^{28}	10^{28}	10^{30}
0.5	0.77	1.20	1.92
0.7	0.71	1.00	1.60
1.0	0.69	0.86	1.36
1.2	0.68	0.80	1.18
1.4	0.68	0.76	1.08

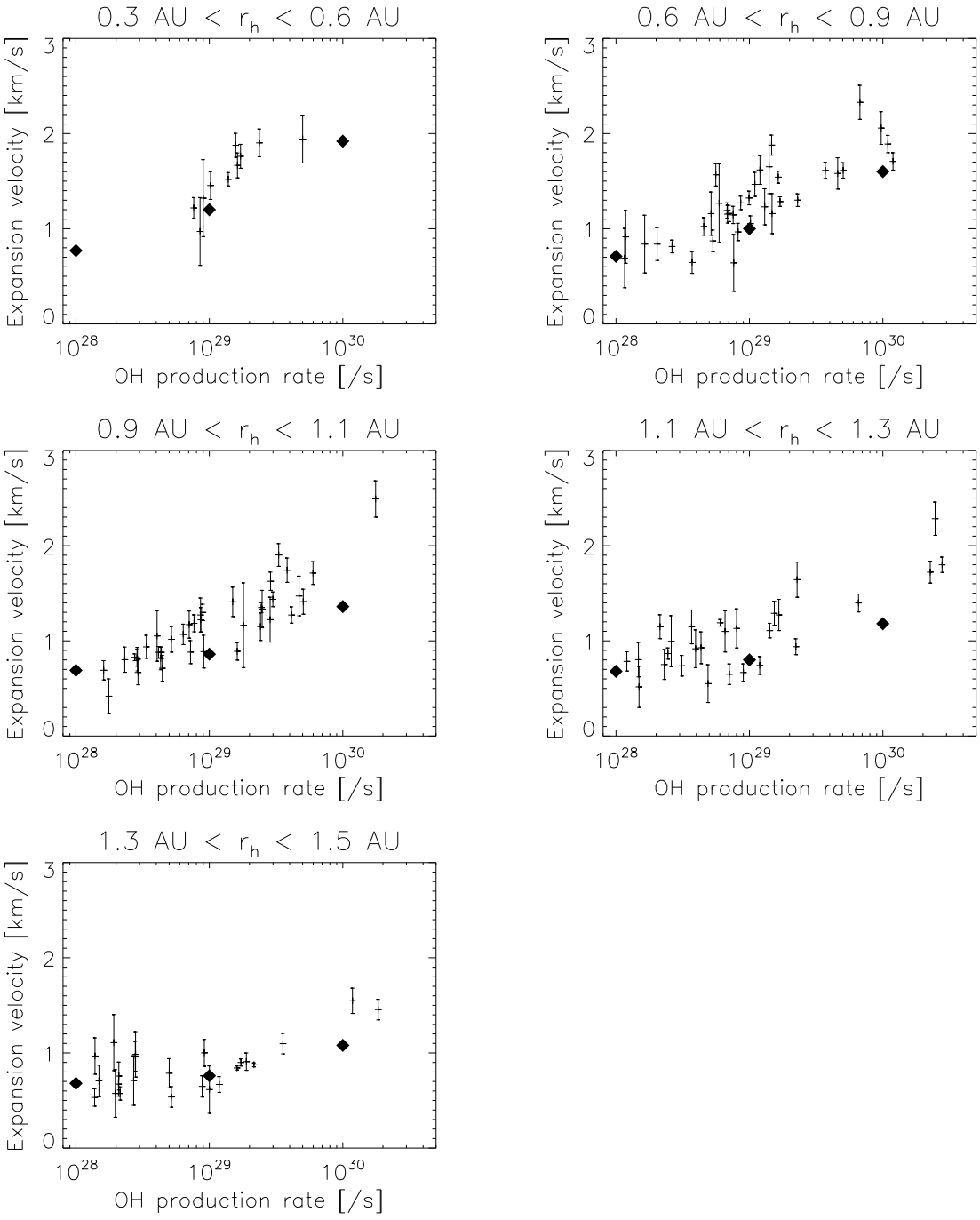

Figure 6.8: H_2O expansion speed retrieved from remote observations and obtained from our model at a cometocentric distance of 10^5 km. The speeds from observations are shown by vertical lines with error bars, which are reproduced from *Tseng et al.* (2007). The solid diamonds represent our model results.

production rate (*Combi et al.*, 2004; *Harris et al.*, 2002). For simplicity, we assume the OH and H_2O production rates are the same. Beyond 0.6 AU, the diamonds in the 10^{28} and $10^{29}\,s^{-1}$ cases are close to each other, while the spread between the 10^{29} and $10^{30}\,s^{-1}$ cases is significantly larger. In the figure where the heliocentric distance is smaller than 0.6 AU, the increase in production rate results in a more evenly increase in water speeds than at other distances. This reflects the nonlinear effect of the production rate and the heliocentric distance on the expansion speed, which is similar to the threshold effect mentioned by *Tseng et al.* (2007). In addition, the model is also applied to comet C/1995 O1 (Hale-Bopp) at the heliocentric distance of 1.0 AU. The radiative cooling effect is neglected within 10^4 km because of the high production rate of 8×10^{30} s. Our model yields similar results to that of the single fluid model in *Combi et al.* (1999) and *Combi* (2002), which matched the observations in *Biver et al.* (2002). It is because the production rate is so large that most heavy species are coupled within a cometocentric distance of 10^5 km and thus the single fluid assumption is still valid. In any case, our multi-fluid model well reproduces the observed variation in coma outflow speeds with different comet gas production rates and heliocentric distances.

CHAPTER VII

The Plasma environment in Comets Over A Wide Range of Heliocentric Distances: Application to Comet C/2006 P1 (McNaught)

In this chapter, the multi-species plasma model introduced in Chapter 3 is applied to a specific comet,i.e. C/2006 P1 (McNaught), to study its cometary plasma environment. On January 12th of 2007, comet C/2006 P1 (McNaught) passed its perihelion at 0.17 AU. Abundant remote observations offer plenty of information on the neutral composition and neutral velocities within 1 million kilometers of the comet nucleus. In early February, the Ulysses spacecraft made an in situ measurement of the ion composition, plasma velocity, and magnetic field when passing through the distant ion tail and the ambient solar wind. The measurement by Ulysses was made when the comet was at $\sim$ 0.8 AU from the sun. With the constraints provided by remote and in situ observations, we simulated the plasma environment of Comet C/2006 P1 (McNaught) using a multi-species comet MHD model over a wide range of heliocentric distances from 0.17 AU to 1.75 AU. The solar wind interaction of the comet at various locations is characterized and typical subsolar standoff distances of bow shock and contact surface are presented and compared to analytic solutions. The comparisons enable us to have a better understanding of the underlying physics of the plasma en-

vironment around comets. We find the variation in the bow shock standoff distances at different heliocentric distances is smaller than that of the contact surface. The ratio between the standoff distances of the bow shock and the contact surface rises as the heliocentric distance increases. In addition, we modified the multi-species model for the case when the comet was at 0.7 AU and achieved comparable water group ion abundances, proton densities, plasma velocities and plasma temperatures to the Ulysses/SWICS and SWOOPS observations. We discuss the dominating chemical reactions throughout the comet-solar wind interaction region and demonstrate the link between the ion composition near the comet and in the distant tail as measured by Ulysses.

7.1 Introduction

Comet C/2006 P1 (McNaught) passed its perihelion at 0.17 AU on January 12th of 2007, ejecting volatile and refractory materials at a rate several times larger than comet Halley during its last apparition in 1986. As usual, many observers monitored the comet and made abundant data available. *Russo et al.* (2009) studied the relative abundances of eight parent volatiles (H_2O, CH_4, C_2H_2, C_2H_6, HCN, CO, NH_3, and H_2CO) and two daughter species (OH and NH_2), which were obtained from high-resolution infrared observations two weeks after the comet's perihelion passage when it was at a heliocentric distance of 0.53-0.55 AU. Since the meters-thick outer layers of the comet's nucleus would have been lost during the pre-perihelion passage, the near and post-perihelion composition of the coma is thought to be representative of the comet's more pristine composition. Such studies constrain the formation region of the comet and its temperature. *Biver et al.* (2011) did a similar study of OH, HCN, HNC, CS, and CH_3OH obtained by spectroscopic radio observations. In addition, *Combi et al.* (2011) applied their inversion method to the SWAN images of the hydrogen coma from 1.05 AU before perihelion to 1.84 AU after passage, to extract the daily water

production rates of the comet. In early February, the Ulysses spacecraft measured the ion composition in situ, serendipitously passing through the distant ion tail while the comet itself was at roughly 0.8 AU and Ulysses at 2.4 AU (*Neugebauer et al.*, 2007).

Most previous studies had modeled the cometary plasma environment for comets at heliocentric distances near 1 AU (see *Ip* (2004) and *Gombosi* (2015) and references therein). Some more recent studies have modeled the cometary plasma environment for weak comets at a range of solar distances, from 0.3 AU (*Jia et al.*, 2009) to 3.2 AU, (*Hansen et al.*, 2007; *Rubin et al.*, 2014a). A recent multi-fluid study has modeled the plasma environment around a sun-grazing comet at 0.005 AU, in novel conditions that are below the solar wind sonic point (*Jia et al.*, 2014).

In this chapter, the multi-species MHD model is applied to comet McNaught, to calculate the cometary plasma distribution throughout its apparition around the Sun including the portion of the orbit near its very small perihelion distance of only 0.17 AU and during the Ulysses encounter with its very distant ion tail to constrain the modeled ion abundances by the available Ulysses measurements (*Neugebauer et al.*, 2007).

Models and model input parameters are briefly described in the following Methodology section. In the Results and Discussion section, modeled bow shock standoff distances and contact surface standoff distances of comet McNaught over a wide range of heliocentric distances are presented. The modeled results are also compared with analytic solutions. Furthermore the underlying assumptions of the analytic solutions are discussed to better understand the physics of the solar wind-comet interaction. In addition, results of water group ion abundances, proton density, plasma velocity, and plasma temperature from the multi-species comet MHD model are shown and compared with the Ulysses observations. Along with the chemical composition results, the dominant chemical reactions near the nucleus and in the tail are discussed.

Table 7.1: Comet & Solar wind Parameters (compiled from *Biver et al.* (2011), *Combi et al.* (2011), and *Neugebauer et al.* (2007))

Case	r(AU)	Q_{H_2O} (1/s)	$U_{neutral}$ (km/s)	n_{sw}(/cm^3)	Bx (nT)	By (nT)	Date (2007)
1	0.17	5.5×10^{31}	2.5	69	78	6.8	Jan 13
2	0.3	6.4×10^{30}	2.0	22	25	2.3	Jan 19
3	0.5	5.5×10^{30}	1.5	8	9	0.5	Jan 26
4	0.75	1.1×10^{30}	1.0	3.5	4	0.4	Feb 5
5	1.0	5.8×10^{29}	0.9	2	2.3	0.4	Feb 15
6	1.25	3.5×10^{29}	0.8	1.3	1.5	0.4	Feb 27
7	1.5	1.4×10^{29}	0.7	0.9	1.0	0.4	Mar 12
8	1.75	7.5×10^{28}	0.7	0.65	0.7	0.35	Mar 26

7.2 Methodology

7.2.1 Parameters used in modeling the comet-solar wind interaction

In our model, the solar wind flows through the coma, which can be ionized and loaded into the solar wind stream, and plasma structures (i.e. bow shock, contact surface, magnetic tail, etc,) are formed around the comet as a result of this interaction (*Gombosi*, 2015). For simplicity, the incoming solar wind flow does not change with time in our model so that a steady state solution can be reached. According to the Ulysses observations (from February 2006), we assume that the solar wind speed is 780 km/s and temperature is 10^5 K as the upstream solar wind condition for all cases and the magnetic field follows a Parker spiral. We pick a typical fast solar wind value for the solar wind density, which varies as $1/r^2$, where r is the heliocentric distance. Parameters for the solar wind conditions are listed in Table 7.1.

In addition to the solar wind conditions, the cometary neutral gas production rates and ionization rates, which control the rate by which cometary ions are loaded into the solar wind, play a major role in the interaction. The H_2O production rates and neutral velocities obtained from the radio, IR, and the SOHO/SWAN observations are also listed in Table 7.1. In a single-species model, only one single rate is used

to describe the neutral density decay and cometary ion productions. However, a multi-species model is able to take the density distributions of various neutrals (e.g. H_2O, OH, O, H, CO, CO_2) calculated by the Haser model as the neutral background, which supplies ions to the solar wind flow via photo-ionization and charge exchange. The production rates of parent species CO and CO_2 are obtained from observations and estimates from this and other comets. *Russo et al.* (2009) reported the CO/H_2O ratio was 1.8% while radio observations by *Biver et al.* (2011) yielded 3% ± 1%. *Ootsubo et al.* (2012) estimated the CO_2/H_2O ratio, which can range from 4% to 20%. According to some arguments by *A'Hearn et al.* (2012) regarding chemical evolution in the early solar nebula, CO and CO_2 could be somewhat anti-correlated. So if the CO fraction is low then CO_2 could be somewhat higher. Therefore, we use 3.5% as the CO/H_2O ratio to calculate the CO production rate and 10% as an estimate for CO_2/H_2O in the multi-species model. In previous single species models, the ionization rate and the total destruction rate of neutrals were assumed to be 10^{-6} s^{-1} at 1 AU, and this single number was then used in the Haser model to provide the neutral density distribution. The multi-species model applies all major photo-ionization and photo-dissociation rates into the Haser model to provide the density distributions of various neutral species. The reference reaction rates at 1 AU are listed in Table 7.2.

7.2.2 Multi-species MHD model description

Developed from a single fluid MHD model (*Jia et al.*, 2007; *Rubin et al.*, 2009), our multi-species model is based on the BATS-R-US (Block Adaptive Tree Solar-wind Roe Upwind Scheme) code (*Powell et al.*, 1999; *Tóth et al.*, 2012), but allows each of the ion species to have its own density, while the velocities and temperatures are averaged assuming the ion species are tightly coupled. The case of comet C/2008 P1 (McNaught), a productive comet at moderate and small heliocentric distances,

Table 7.2: Photo-chemical reactions and rates included in the multi-species model from *Huebner et al.* (1992) and *Rubin et al.* (2009)

Reaction	Reaction rate at 1 AU
$H_2O + h\nu \rightarrow H_2O^+ + e$	5.4×10^{-7}
$H_2O + h\nu \rightarrow H^+$	2×10^{-8}
$H_2O + h\nu \rightarrow H + OH$	1.0×10^{-5}
$H_2O + h\nu \rightarrow OH^+$	9×10^{-8}
$H_2O + h\nu \rightarrow O^+$	9.5×10^{-9}
$H_2O + h\nu \rightarrow O + H_2$	1.35×10^{-6}
$H + h\nu \rightarrow H^+ + e$	1.2×10^{-7}
$OH + h\nu \rightarrow H^+$	6×10^{-8}
$OH + h\nu \rightarrow OH^+ + e$	3.94×10^{-7}
$OH + h\nu \rightarrow O^+$	5.3×10^{-8}
$OH + h\nu \rightarrow O + H$	6.56×10^{-6}
$O + h\nu \rightarrow O^+ + e$	3.45×10^{-7}
$CO + h\nu \rightarrow O^+$	4×10^{-8}
$CO + h\nu \rightarrow CO^+ + e$	6.25×10^{-7}
$CO + h\nu \rightarrow C + O$	3.14×10^{-7}
$CO_2 + h\nu \rightarrow CO + O$	1.2×10^{-6}
$CO_2 + h\nu \rightarrow CO_2^+$	6.6×10^{-7}
$CO_2 + h\nu \rightarrow CO^+$	5×10^{-8}
$CO_2 + h\nu \rightarrow O^+$	6.4×10^{-8}
Total Photo-destruction of H_2O	1.2×10^{-5}
Total Photo-destruction of OH	7.42×10^{-6}
Total Photo-destruction of CO	1.3×10^{-6}
Total Photo-destruction of CO_2	2.0×10^{-6}
Total Photo-destruction of O	3.45×10^{-7}

is in contrast to those studied by *Rubin et al.* (2014a) that have addressed a weak comet 67P/Churyumov-Gerasimenko at larger heliocentric distances where a multi-fluid model is more appropriate. Previous separated chemical-MHD models used by *Häberli et al.* (1997) and *Rubin et al.* (2009), first computed a single-species MHD solution and then subsequently, based on the obtained flow field, solved the chemical reaction network along each individual plasma flow line. Our model has integrated MHD and chemistry into one set of controlling equations, although fewer minor species are included. Such multi-species models have been applied to the Mars' atmosphere (*Ma et al.*, 2004) and to comet Halley at 1 AU (*Jia*, 2007). The H_2O^+ abundance within 1 million kilometers (Mkm) has been studied by *Häberli et al.* (1997). In contrast, we modeled water group ions in the long tail which extends to a distance of more than 200 Mkm.

The multi-species MHD equations have been described in Chapter 3. Following *Jia* (2007), we include the 7 most abundant ion species: H^+, O^+, OH^+, H_2O^+, H_3O^+, CO^+ and CO_2^+. The Haser model is used to provide a steady state background for various neutral species, in which the neutrals have constant radial speed. The multi-species model is able to track several ion species and various chemical reactions for a more accurate solution than a single species model. The reactions of charge-exchange and (dissociative) ion-electron recombination and their rate constant coefficients are included in Tables 7.3 and 7.4. Most charge exchange reactions lead to changes in ion densities, plasma momentum, and plasma pressure. We would like to point out that symmetric charge exchange reactions similar to H_2O+H_2O^+ do not contribute to the continuity equation, but the pick-up ion still plays a role in decelerating the solar wind and heating the plasma, which can be seen from above equations.

The Cometocentric Solar Ecliptic coordinate system is adopted in the model with the x-axis pointing to the Sun. The simulation volume ranges from -16 to 16 Mkm for all cases except that at 0.75 AU as explained below. The y-axis lies in the plane

Table 7.3: Charge-exchange reactions and rate constant coefficients from *Häberli et al.* (1997) and by estimation

Reaction	Rate constant coefficient m^3s^{-1}
$H_2O^+ + H_2O \rightarrow H_3O^+ + OH$	2×10^{-15}
$H_2O^+ + CO \rightarrow CO^+ + H_2O$	4.3×10^{-16}
$H^+ + H \rightarrow H + H^+$	2×10^{-15}
$H^+ + H_2O \rightarrow H_2O^+ + H$	8.2×10^{-15}
$H^+ + OH \rightarrow OH^+ + H$	4.4×10^{-15}
$H^+ + O \rightarrow O^+ + H$	3.8×10^{-16}
$H^+ + CO_2 \rightarrow CO_2^+ + H$	2×10^{-15}
$OH^+ + H_2O \rightarrow H_3O^+ + O$	1.3×10^{-15}
$OH^+ + H_2O \rightarrow H_2O^+ + OH$	1.6×10^{-15}
$OH^+ + CO \rightarrow CO^+ + OH$	8×10^{-16}
$O^+ + H_2O \rightarrow H_2O^+ + O$	3.2×10^{-15}
$O^+ + OH \rightarrow OH^+ + O$	3.2×10^{-15}
$CO^+ + H_2O \rightarrow H_2O^+ + CO$	1.6×10^{-15}
$CO^+ + OH \rightarrow OH^+ + CO$	3×10^{-16}
$CO^+ + CO_2 \rightarrow CO_2^+ + CO$	1.1×10^{-15}

Table 7.4: Dissociative recombination reactions and rate constant coefficient from *Schunk and Nagy* (2009) (Te is electron temperature in unit of (K)).

Reaction	Rate constant coefficient cm^3s^{-1}
H_2O^+ and H_3O^+	$1.57 \times 10^{-5}T_e^{-0.569}$ for $T_e <$ 800 K $4.73 \times 10^{-5}T_e^{-0.74}$ for 800 K $< T_e <$ 4000K $1.03 \times 10^{-3}T_e^{-1.111}$ for $T_e >$ 4000K
OH^+	$3.75 \times 10^{-8}(300/T_e)^{0.5}$
CO^+	$2.75 \times 10^{-7}(300/T_e)^{0.55}$
CO_2^+	$4.2 \times 10^{-7}(300/T_e)^{0.75}$

containing magnetic field, and the z-axis completes the right-handed system pointing to the north of the ecliptic plane. The comet is a point source sitting at the origin. An adaptive mesh, featured by the BATS-R-US code, is applied in all simulations to model the bow shock and the contact surface, because length scales can differ by several orders of magnitude. The highest grid resolution of 50 km is applied to the region near the contact surface and the inner shock. The cell size near the bow shock

is on the order of 1000 km.

7.2.3 Special treatment to model the long tail

To compare with the Ulysses observations in the distant tail, we extend the computing domain to 256 Mkm (1.7 AU) downstream along the comet-sun line with a cell size of about 0.05 Mkm. We impose a spherical wave-like inflow boundary condition so that the inflow velocity realistically diverges radially from the Sun over large distances.

Although the Ulysses/SWICS observations provide the abundance ratios along the crossing trajectory, its relative location to the comet tail cross section is not known. Values along several reasonably spaced lines are extracted from the model output, attempting to find the best agreement to the observations,and are discussed below in section 7.3.4.

7.3 Results and discussion

7.3.1 Bow shock standoff distances

We ran the multi-species model and reached the steady state for each of the heliocentric distances with the basic input parameters listed in Tables 7.1-7.4. Model results show a bow shock exists at comet McNaught in all eight cases, while the subsolar standoff distances of the bow shocks vary. We also find the bow shock standoff distances are at least two orders of magnitude larger than the gyro-radius of the cometary pick-up ions, which validates our fluid approach. The model results, with analytic solutions, are listed in Table 7.5 and are also shown in Fig. 7.1.

The multi-species model results show that the bow shock standoff distances for all cases are on the order of 0.1 Mkm. The variation is not as significant as that in the production rates or solar wind densities. We can see the general trend from

Table 7.5: Comparison of calculated bow shock subsolar standoff distances. The bow shock standoff distances from multi-species are listed under the column multi-species. BS1 column lists bow shock standoff distances calculated from analytic solution. All are in units of Mkm.

Case	r(AU)	Multi-species model	BS1	β	B_x/B_y
1	0.17	0.63	0.30	0.04	11.4
2	0.3	0.44	0.41	0.12	10.9
3	0.5	0.66	0.70	0.34	18.0
4	0.75	0.37	0.62	0.75	10.0
5	1.0	0.31	0.64	1.27	5.7
6	1.25	0.27	0.62	1.87	3.75
7	1.5	0.16	0.43	2.7	2.5
8	1.75	0.1	0.30	3.7	2.0

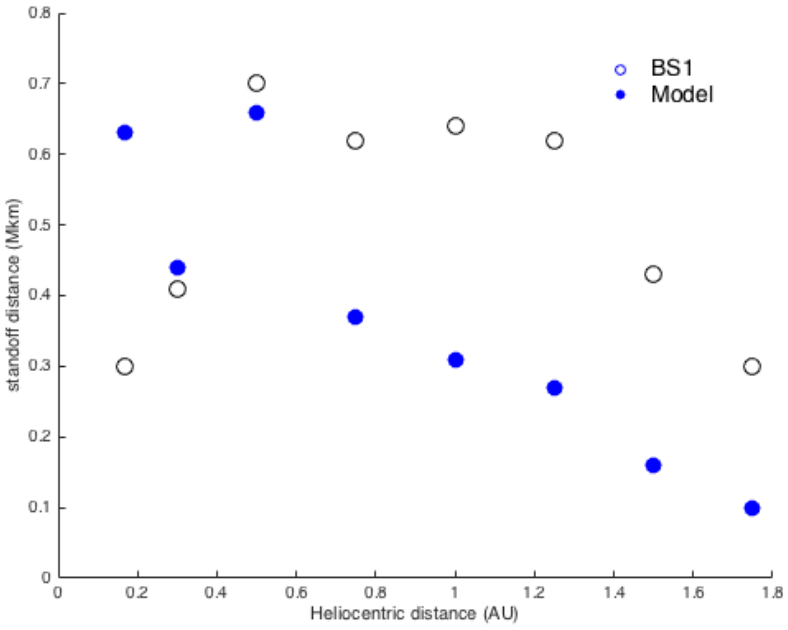

Figure 7.1: The subsolar standoff distances at various heliocentric distances calculated by the analytic solution BS1 (black circles) and extracted from our model (solid blue circle).

Table 7.5 that for cases with a comet heliocentric distance larger than 0.5 AU, the standoff distance decreases as the heliocentric distance increases. However, the cases at 0.3 AU and 0.17 AU are not following the trend and a local minimum exists at 0.3 AU. It may reflect that there are competing factors in determining the bow shock standoff distance. Higher production rates, ionization rates, and dissociation rates can increase the distance, while higher solar wind fluxes can push the bow shock closer to the comet nucleus. *Koenders et al.* (2013) also discussed the influences of different parameters on the bow shock distance on a weak comet. Cometary bow shocks are formed because of the pickup ions, i.e. the mass-loading effect, which is quite different from the bow shocks at Earth or other magnetized planets. The following comparison between the model results and analytic solutions can shed light upon the differences.

The analytic solution is based on the characteristics of mass loading produced shocks which form where the mass flux ratio reaches a critical number. The ratio can be expressed as

$$\hat{\rho}\hat{u} = \frac{\rho_i u_i + \rho_{sw} u_{sw}}{\rho_{sw} u_{sw}},$$

where ρ_i and ρ_{sw} are cometary and solar wind ion mass densities, u_i and u_{sw} are cometary and solar wind ion velocities, respectively. The theoretical limit of the mass flux ratio first derived by *Biermann et al.* (1967) under the hydrodynamic assumption was $\frac{\gamma^2}{\gamma^2-1}$, where γ is the ratio of specific heats. Later *Huddleston et al.* (1992) applied this method with 6/5 as the critical ratio to predict the bow shock standoff distance of comet Grigg-Skjellerup, claiming it is a good estimation to mass flux ratios often observed by spacecraft. We used 6/5 as well to calculate the analytic solutions. Following *Huddleston et al.* (1992), we assume the cometary ion flux at one point (x_0, y_0) is the ion production rate integrated along mass-loaded streamlines of the upstream solar wind. For simplicity of calculation, the integral is taken from infinity.

Then it can be written as

$$n_i u_i = \frac{Q}{4\pi\lambda} \int_{x_0}^{\infty} \frac{\exp\left[-(x^2+y_0^2)^{\frac{1}{2}}\right]}{x^2+y_0^2} dx,$$

where n_i and u_i are cometary ion number density and velocity respectively, λ is the ionization length scale and neutral decay length scale and can be calculated as $\lambda = u_n/\nu$, where ν is the ionization frequency. x_0 and y_0 are in units of λ. Since we are looking for the point where the mass flux ratio arrives at its critical number on the comet-sun line, y0 is set to 0 and the solar wind flux is known, which leads to

$$\int_{x_0}^{\infty} \frac{\exp(-|x|)}{x^2} dx = \frac{4\pi\lambda^2 \rho_{sw} u_{sw}}{Q m_i} [(\hat{\rho}\hat{u})_c - 1], \tag{7.1}$$

where m_i is the cometary ion mass and $(\hat{\rho}\hat{u})_c$ is the critical mass flux ratio. We are then able to solve for x_0, the lower bound of the integral. Following this approach, the shock standoff distance is obtained. The results are listed in the BS1 column in Table 7.5.

They vary within one order of magnitude and ratios among the cases agree well with model results, indicating the results from the analytic solution reflect the same trend as the model results. It also should be noted that the BS1 results at distances farther than 0.75 AU are larger than the model by a factor of 2 or 3. And BS1 at 0.17 AU is only about half of the model result. The difference is probably caused by magnetic field, since BS1 method is mainly based on an hydrodynamic assumption. The plasma beta of the upstream solar wind, which is the ratio of thermal pressure to magnetic pressure ($n_{sw} k_B T/(B^2/2\mu_0)$) and the ratio of the radial component of the magnetic field to tangential component (B_x/B_y) are listed in Table 7.5. When β is extremely small or the tangential component is relatively large, the condition

is far from a hydrodynamic case. Otherwise, a hydrodynamic assumption is a good approximation, as in the cases at 0.3 and 0.5 AU. The other factor that might contribute to the discrepancy between BS1 and the multi-species model is the parameters used to calculate the background neutral density and the production rate of cometary ions. In BS1 method, the decay rate of neutral density and the ionization rate are assumed to be the same and both use 10^{-6} s^{-1}. But in the multi-species model, we use various ionization rates and neutral dissociation rates (see Table 7.2). Since the single-species MHD model inherits the same assumption, single-species MHD cases that we do not show here give closer bow shock standoff distances to BS1 results than the multi-species model.

We have also tested other analytic solutions but none of them are closer to the model results than BS1. If x in Equation 7.1 is much smaller than 1, $exp(-|x|)$ in the integral can be replaced by 1 and we can obtain

$$BS2 = \frac{Qm_i}{4\pi\lambda\rho_{sw}u_{sw}[(\hat{\rho}\hat{u})_c - 1]}.$$

It is given by **?** as an approximation to BS1 when the bow shock standoff distance is much less than the ionization length scale. If the critical mass flux ratio is a constant, we can see that BS2 is proportional to $Q/((\rho_{sw}u_n r_H^2)$, where r_H is the heliocentric distance. For the same parameters as in Table 7.1, one can find the variation in BS2 is more than two orders of magnitudes. However, correction to the critical mass flux ratio can improve the performance.

Flammer and Mendis (1991) followed a magnetohydrodynamic approach and presented an analytic solution for the critical mass flux ratio, which is a function of thermal pressure, magnetic pressure, and dynamic pressure of the undisturbed solar wind. *Koenders et al.* (2013) applied this solution and BS2 to predict the bow shock positions of comet Churyumov-Gerasimenko. The results agreed with their hybrid

model results fairly well and produced a better fit than a constant critical mass flux ratio. It may be because the assumption holds well for weak comets, while when it comes to comets with high production rates and smaller ionization length scales, especially for the case at 0.17 AU, the assumption breaks down. We do not include the complicated equations in *Flammer and Mendis* (1991) to take into account the effect of magnetic field for simplicity. Since BS1 solution without the correction can still produce a good fit to the model results, we think it is likely that this solution captures the essential physics underlying the formation of a mass-loading bow shock at comets.

7.3.2 Contact surface standoff distances

The contact surface is a unique feature of the cometary plasma environment. It is usually located just outside the ion-neutral coupling region where the ions are subject to ion-neutral collisions. Inside the contact surface the cometary heavy ions are expanding radially outward at the velocity of the neutrals, while the heavily contaminated solar wind almost stagnates outside of the contact surface. As the boundary of the mass-loaded solar wind and the cometary ionosphere, the contact surface also prevents the solar wind magnetic field from penetrating into the cometary ionosphere. Therefore, the magnetic field piles up and the magnetic field lines drape around the contact surface. Inside the field becomes zero, thus creating a diamagnetic cavity. Because of the discontinuity in the almost stagnating solar wind and the radially supersonic cometary outflow, an inner shock exists near the inner boundary of the contact surface to terminate and divert the cometary ions toward the tail.

We tabulate the contact surface's subsolar standoff distances from the multi-species model together with analytic solutions in Table 7.6 and in Fig.7.2. The modeled distance almost decreases monotonically as the heliocentric distance increases with the exception at 0.3 AU that has a standoff distance smaller than that at 0.5

Table 7.6: Comparison of contact surface standoff distances. The contact surface standoff distances from multi-species are listed in the column multi-species. CS1 is contact surface standoff distances calculated from the analytic solution. They are in units of 10^3 km.

Case	r(AU)	Multi-species	CS1	β
1	0.17	84.2	22.7	0.04
2	0.3	14.5	6.4	0.12
3	0.5	20.4	7.9	0.34
4	0.75	5.9	3.2	0.75
5	1.0	4.1	2.3	1.27
6	1.25	2.4	1.83	1.87
7	1.5	1.3	1.0	2.7
8	1.75	0.72	0.71	3.7

AU. The trend is similar to that found for bow shock results. The variation is larger than that of the bow shock subsolar standoff distances. The length scale of the cavity at 0.17 AU is more than 100 times of that at 1.75 AU. This indicates that the standoff distance of the contact surface is more sensitive to the changes of the production rate and the neutral velocity than the bow shock.

The analytic solution was first derived by *Cravens* (1986) and improved by *Gombosi* (2015). It can be written as

$$r_{cs} = \sqrt{\frac{m_i}{m_{sw}} \frac{k_{in}}{4\pi n_{sw} u_{sw}^2} \sqrt{\frac{\nu_0 / r_H^2}{4\pi \alpha u_n}} Q^{3/4}},$$

where ν_0 is the ionization rate at 1 AU and r_H is the heliocentric distance in the unit of AU. k_{in} and α are ion-neutral collision and ion-electron dissociative recombination rate coefficients, respectively. Here we take the same form for the coefficients as in *Cravens* (1986) k_{in}=1.1×10^{-9} cm^3/s and α=1.21×10$^{-5}/\sqrt{T_e}$ cm^3/s. The underlying physics is that the $\mathbf{J} \times \mathbf{B}$ force and the ion-neutral friction balance each other at the contact surface. Since the formation of H_3O^+ has a smaller chemical reaction time scale than the transportation time scale inside the contact surface, chemical equi-

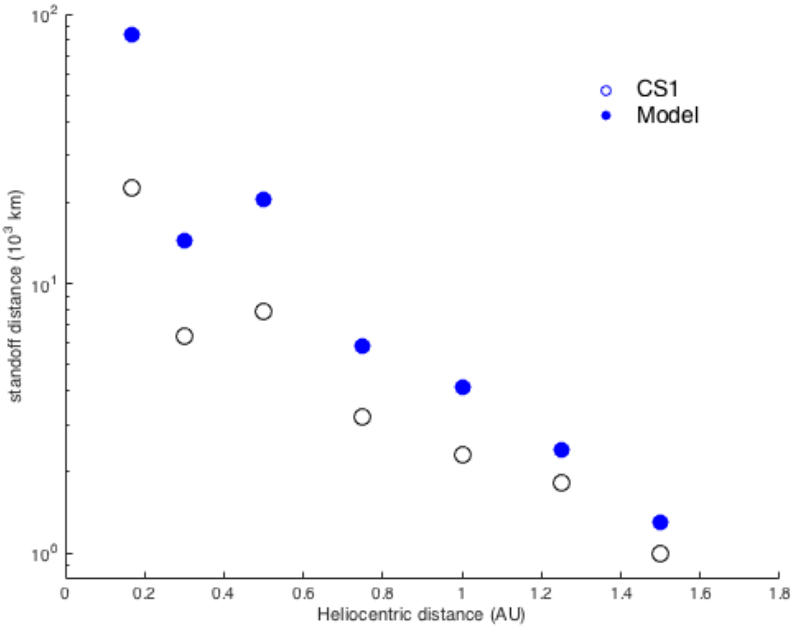

Figure 7.2: The subsolar standoff distances of the contact surface at various heliocentric distances calculated by the analytic solution CS1 (black circles) and extracted from our model (solid blue circle).

librium is assumed to calculate the ion and electron densities. A constant electron temperature of 200 K, which is a typical electron temperature near contact surface (*Häberli et al.*, 1996), is used in the calculation. One can also notice that the analytic solution does not consider the magnetic field, because the original derivation assumes that the magnetic pressure in front of the contact surface is equal to the solar wind dynamic pressure. In addition, the ion pile-up region in front of cavity is neglected (*Häberli et al.*, 1995). From Table 7.6, we can see that the analytic solution results (CS1) are able to produce the same trend for all cases. They are in good agreement with our model results for cases at distances larger than 0.75 AU. The better agreement at larger heliocentric distances can be explained by the assumption in the derivation, which does not include the magnetic field of the solar wind and the pile-up in front of the cavity. However, the general agreement between the analytic solution and the model also indicates that most assumptions and approximations made above

Table 7.7: Comparison of the ratios between bow shock and contact surface standoff distances.

Case	r(AU)	Multi-species	BS1/CS1
1	0.17	7.5	13.2
2	0.3	30.3	64.1
3	0.5	32.35	88.6
4	0.75	62.7	193.8
5	1.0	75.6	278.3
6	1.25	112.5	338.8
7	1.5	123.1	430.0
8	1.75	138.9	428.6

are reasonable.

We list the ratios of the bow shock standoff distance to the contact surface standoff distance in Table 7.7 from the multi-species model and the analytic solutions. There is a clear trend in both model and the analytic solutions that the contact surface standoff distance relative to the bow shock standoff distance decreases, as the heliocentric distance of comet increases. This is also consistent with the model results of weak comets at very large heliocentric distances. *Hansen et al.* (2007) shows no contact surface is formed at comet 67P/Churyumov-Gerasimenko at 3.25 AU in either single-species MHD or Hybrid simulations. The ratios from the analytic solutions are at most 3 times larger than those from the model, which indicates the analytic solutions can be used to provide an upper bound of the ratio between the distances of the contact surface and the bow shock.

7.3.3 Water group ion abundance ratios

To model the composition and dynamics of the extremely long comet tail, two special treatments are made for the 0.7 AU case as mentioned in the Methodology section: (1) elongate the computation domain; (2) apply a "spherical wave" boundary condition to allow for the realistic divergence of the solar wind over large distances.

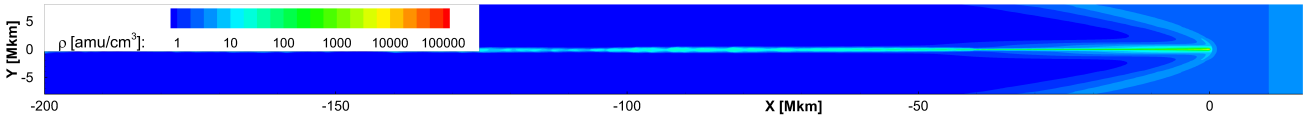

Figure 7.3: Modeled total ion density contour in the magnetic field plane. The computing domain is larger than the region shown in the figure. The comet nucleus is at the origin which corresponds to 0.75 AU from the Sun.

In Fig.7.3, we present the global view of the total ion density, which highlights the extremely long ion tail. In the results we find the density of the background solar wind does drop with $1/r^2$, as it should. With this modified boundary condition, the angle between the bow shock flank and the comet-sun line spreads wider than that without the spherical expansion treatment.

In this section, we focus on the abundance ratios of water group ions close to the nucleus and in the distant tail. Fig. 7.4 shows the modeled water group ion abundance ratios close to the nucleus. It can be easily seen that H_3O^+ ions dominate inside and near the contact surface. Farther away, H_2O^+, OH^+ ,and O^+ take their turns to be the major ion species in that order. It can be readily explained by where they are born. H_2O^+, OH^+, and O^+ are mainly generated by photo-ionization, so they have highest densities if their parent neutral species is most abundant in that region. Fig 7.5 shows densities of neutral species as functions of cometocentric distances. We find H_2O density to be highest near the nucleus but decaying fastest, therefore H_2O^+ is only concentrated in a relatively small region, as is H_3O^+ because it is mostly produced by proton exchange reactions between H_2O^+ and water molecules. In contrast, atomic O is decaying the slowest and constantly gets ionized to O^+, so we can expect O^+ to have a very broad distribution and be dominant at distances far away from the comet.

Fig. 7.6 shows the modeled water group ion abundance ratios in the distant tail. H_3O^+ and H_2O^+ are concentrated in the center of the tail, while O^+ has highest relative abundance in the outer part. This is a natural outcome of the scale lengths of

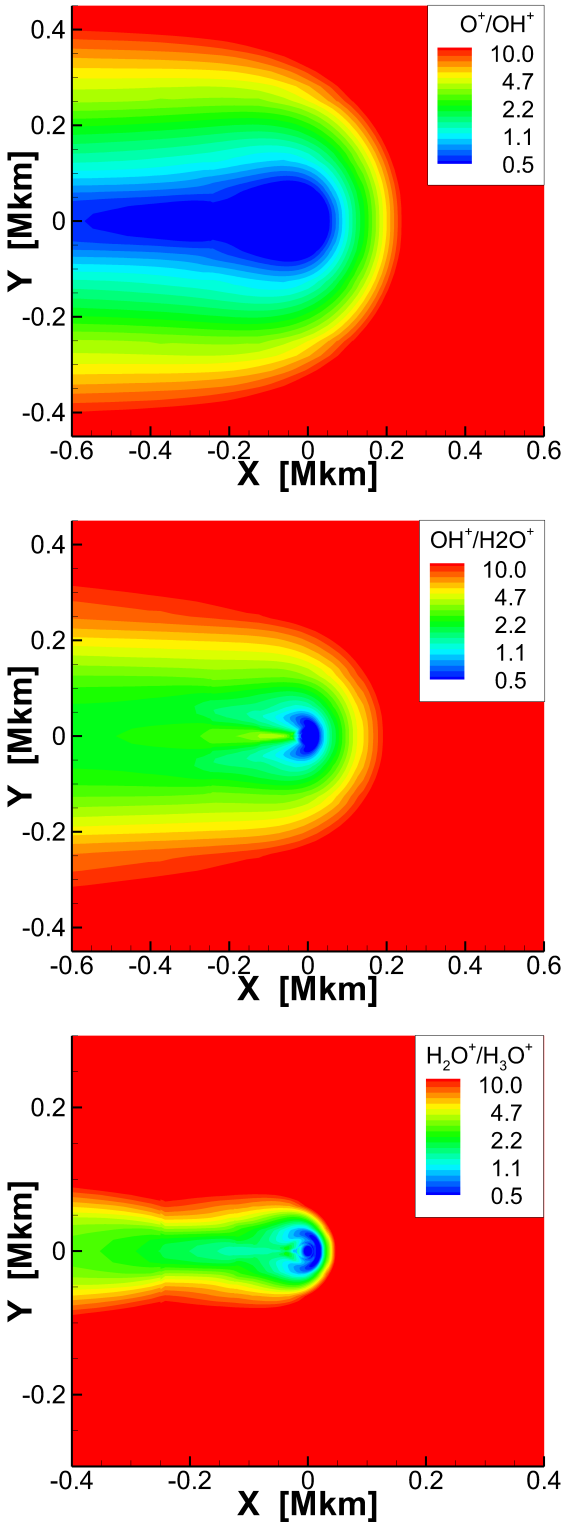

Figure 7.4: Abundance ratios of water group ions near the nucleus.

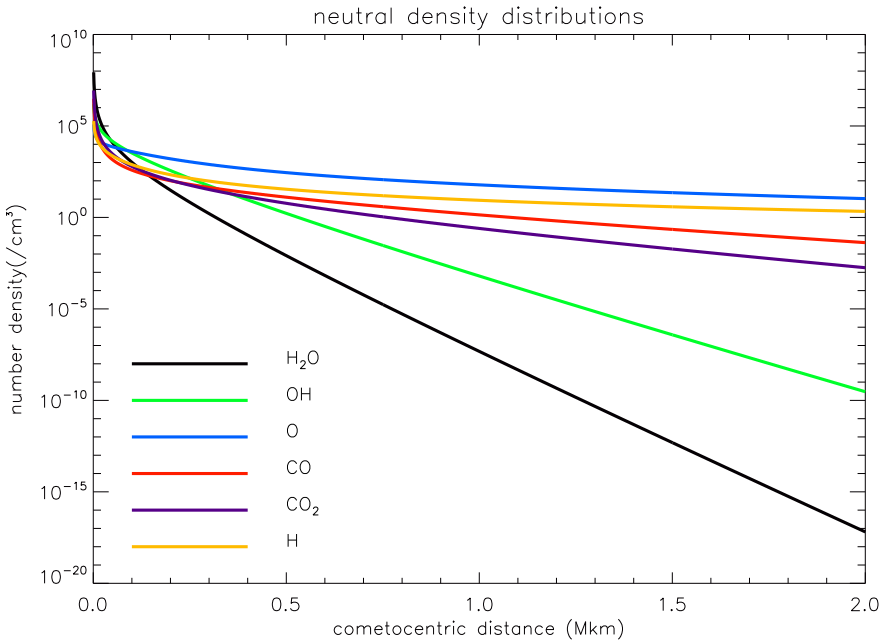

Figure 7.5: Density distributions of neutrals following a Haser-type distribution for comet McNaught at 0.75 AU. This neutral density is then used as a background input for the MHD model.

the original neutrals. The similarity of the abundance ratios between the near nucleus region and the distant tail implies that in this model each streamline preserves some information upstream that one can obtain downstream.

Next we examine the evolution of water group ions in different regions and try to establish the link between ions near the nucleus and far down the tail. As neutral densities decay exponentially due to the photo-chemical destruction and expand spherically with $1/r^2$, they become very depleted at some distance away from the comet nucleus. For example, H_2O, OH, and CO densities drop below $1/cm^3$ around 1 Mkm. This can be seen from Fig.7.5. The neutral-related reactions such as photo-ionization and charge-exchange are important within this distance. Here we define the area where all chemical reactions are active as the chemistry-active region. Beyond that distance down the tail, only electron recombination is significant. This region is defined as a chemistry-quiet region. Less complicated by other processes, it is easier to analyze the asymptotic behavior in this region. From Table 7.4, we

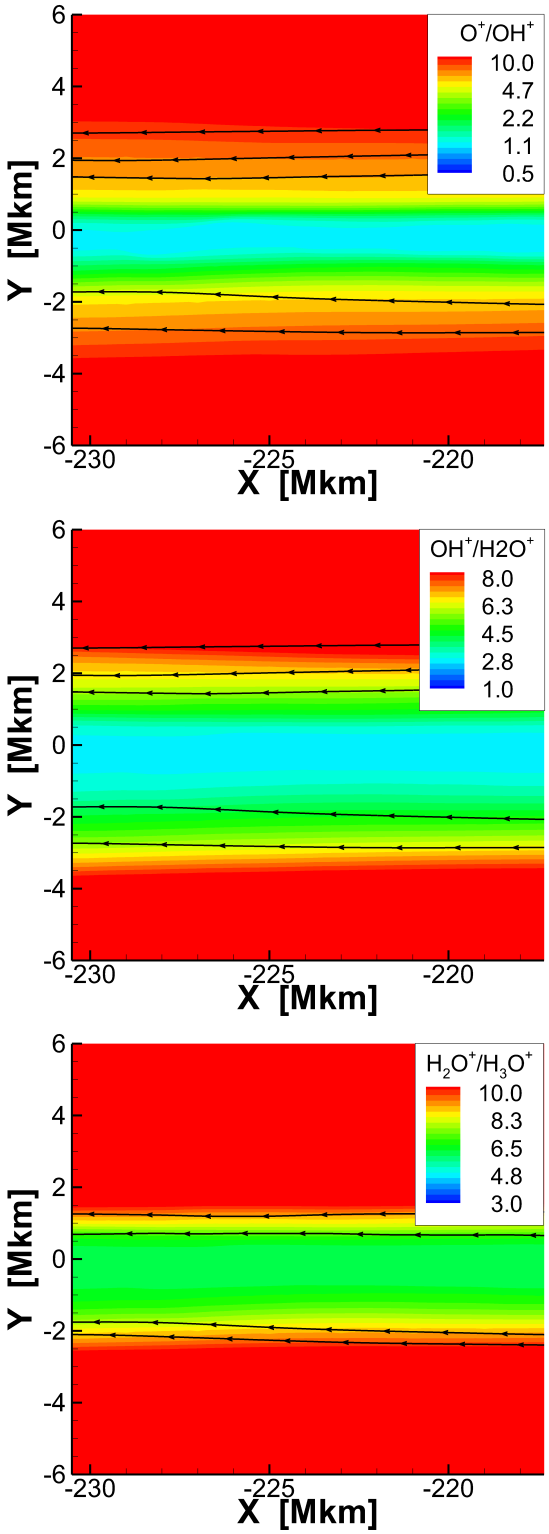

Figure 7.6: Abundance ratios of water group ions in the distant tail (about 1.6 AU from the nucleus). The black solid lines with arrows represent streamlines.

notice that the recombination coefficient constants for H_2O^+ and H_3O^+ are the same. In the chemistry-quiet region, the continuity equations of H_2O^+ and H_3O^+ in a one dimensional steady state case, can be written as

$$u_x \frac{\partial n_{H_2O^+}}{\partial x} = -(\alpha n_e) n_{H_2O^+},$$
$$u_x \frac{\partial n_{H_3O^+}}{\partial x} = -(\alpha n_e) n_{H_3O^+}.$$

We also have

$$\frac{\partial n_{H_2O^+}/n_{H_3O^+}}{\partial x} = \frac{\frac{\partial n_{H_2O^+}}{\partial x} n_{H_3O^+} - \frac{\partial n_{H_3O^+}}{\partial x} n_{H_2O^+}}{n^2_{H_3O^+}}.$$

The above equations yield

$$\frac{\partial (n_{H_2O^+}/n_{H_3O^+})}{\partial x} = 0.$$

This observation indicates if one parcel of H_2O^+ and one parcel of H_3O^+ are travelling together along the same streamline at a same speed, they will have the same fraction of ions convert to neutrals and thus the abundance ratio will remain the same under the assumption that $\alpha(H_2O^+)$ equals $\alpha(H_3O^+)$. Therefore, given one point with a specific H_2O^+/H_3O^+ down the tail in the chemistry-quiet region, one is able to trace upstream along the streamline and locate a point with the same ratio at the outer boundary of the chemistry-active region. It also implies the possibility to extrapolate the relative abundances at very large cometocentric distances if the chemical composition in the chemically active region is known. Here we should note that that streamline's ability to preserve the abundance ratio requires that streamlines do not interact with each other. But realistic solar wind conditions can change rapidly and there are turbulence and various wave activities, all of which are capable of twisting the streamlines and potentially mixing the chemical compositions.

Table 7.8: Comparison of abundance ratios from model and observation.

	Model	Observation
O^+/OH^+	7.3	10
OH^+/H_2O^+	3.1	3.3
H_2O^+/H_3O^+	5.9	3

7.3.4 Comparison with Ulysses observations

To make an accurate comparison, we need to determine where the comet was, when the observed water group ions were produced at the comet. Since there is a great uncertainty in the ion speed, our simple calculation shows the comet might be at 0.5 AU to roughly 0.8 AU, if the ion speed ranges from 200 km/s to 800 km/s. Here we choose 0.7 AU, which can give the best match. The abundance ratios from the model and from the observed results published by *Neugebauer et al.* (2007) are listed in Table 7.8. It can be seen that the species densities in our model are of the same order as those of the observations. The modeled abundance ratios are also close to the observational data.

We have also performed a simple calculation to approximate the relative abundance ratios that considers only one parent species, water, and neglects all charge exchange reactions. With the reaction rates for different products, we are able to calculate ratios between them. For instance, the ionization rate for H_2O to produce H_2O^+ is 5.4×10^{-7}/s and the dissociation rate to produce OH is 10^{-5}/s. From this follows the ratio of H_2O^+ to OH of $5.4\times10^{-7}/10^{-5}$=0.054. The simple calculation shows O^+/OH^+=16.5 and OH^+/H_2O^+=1.2. However, if proton exchange reactions of H_2O^+ are involved, some H_2O^+ ions will be transformed to H_3O^+. The number density of H_2O^+ without undergoing charge exchange reactions is higher than the resulting number density of H_2O^+ with charge exchange reactions included. It is reasonable to increase the ratio of OH^+ to H_2O^+ by a factor of two or three to ac-

count for this effect. Similarly, O^+/OH^+ can also be modified by some other charge exchange reactions listed in Table 7.3. Hence, we can see from this analysis that both our model results and the observational data are consistent with this expectation. However, we notice the ratio between H_2O^+ and H_3O^+ is not as favorable as other two. The difference may come from the uncertainty of the chemical reaction coefficients especially if in reality recombination rates for H_2O^+ and H_3O^+ are different, or there is numerical diffusion in the MHD model. We get the ratio of 5.2 from model results at 10 Mkm tailward from the nucleus, where the grid resolution is higher and the streamlines with different origins are not mixed.

In addition, we show the 1-D profile of proton density, plasma velocity, and plasma temperature along a vertical line cutting across the ion tail at x= -240 Mkm in Fig.7.7. The modeled proton density in the tail is lower than the ambient solar wind, which results from the bow shock's shielding effect. We attribute the bump in the center to the concentration of ions, which are originating from near the contact surface and following the draped magnetic field. The modeled proton density is larger than the observation by a factor of 2. The modeled ion temperature is in the same range as obtained by Ulysses/SWOOPS. Our model results of the plasma velocity show the center of the tail has the lowest velocity of about 200 km/s, which is lower than the 350 km/s observed by Ulysses. This would be the case if Ulysses did not fly exactly across the center of the tail but about 1 Mkm away from the center (cf. Fig.7.7).

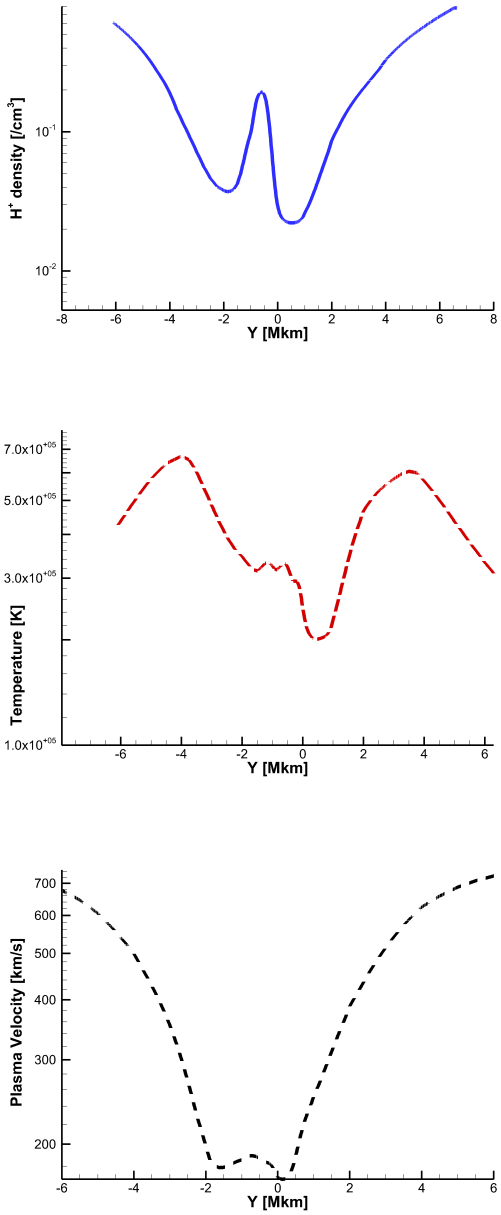

Figure 7.7: Plasma temperature, velocity, and proton density along a vertical line across the tail.

CHAPTER VIII

A study of the effects of activity and nucleus rotation on dust grain behavior in comet 67P/Churyumov-Gerasimenko

In this chapter, we will apply the dust model introduced in Chapter 4 to study the Rosetta target comet 67P/Churyumov-Gerasimenko. Since we limit our study to the vicinity of comet 67P, the radiation pressure and the sublimation of dust grains are not considered. We will first compare our model with the DSMC approach and then study the effects of the cometary rotation and activity on dust grains' behavior using a real-shaped nucleus. In addition, interpretations of some dust observations of the Rosetta target comet 67P/Churyumov-Gerasimenko are also provided.

8.1 Boundary conditions

In the first study we do a comparison with DSMC model and we use a spherical nucleus with a radius of 2 km and run the model in the inertial frame at four heliocentric distances. We also assume the body are not rotating and the solar illumination does not change. The gas flux and temperature are fixed at the surface of the body. The inner boundary conditions of the four cases are compatible with those in *Tenishev et al.* (2011). The surface temperature profile and the water flux distribution

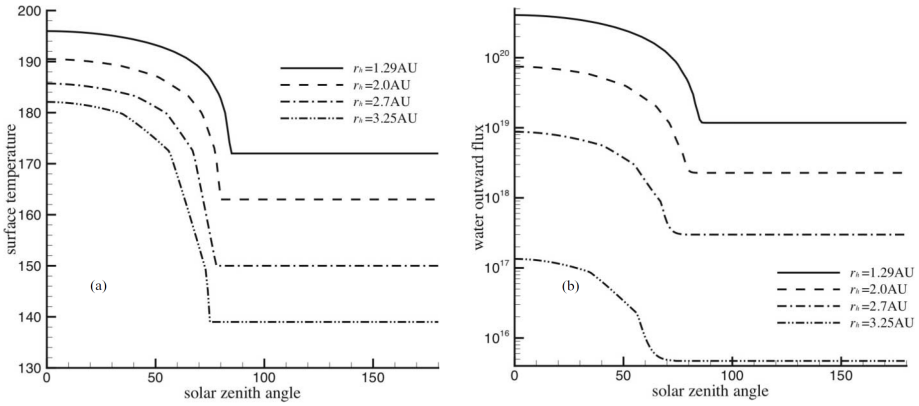

Figure 8.1: Surface temperature profiles (left) and water flux distributions (right) at four heliocentric distances: 1.3, 2.0, 2.7, and 3.3 AU, which is reproduced from *Tenishev et al.* (2011).

are shown in Fig. 8.1. The dust flux is assumed to be proportional to the H_2O flux and the multiplier is given by the ratio of dust-to-gas production rate. The initial velocities of all dust grains are set to be 10^{-4} times of the H_2O gas velocity and the gas drag is then allowed to lift and accelerate the dust. The number density of dust grains follows the power of law, with an exponent of -3: $n(a) \sim a^{-3}$, where a is the radius of the dust grain. Since by definition all particles are initially started at the same small velocity the local density distribution as well as the normally used dust production flux distribution have the same power law at the surface. The gas-dust physics then naturally produces the appropriate dust fluxes as a function of particle size. All of the steady state runs are performed on a spherical grid. The highest resolution is applied to the place close to the nucleus, where it is about 0.02 km in the radial direction and 2.8 and 1.4 degrees in polar and azimuthal directions. Floating boundary conditions are applied to the outer boundaries, where the resolution in radial direction is about 2.5 km.

In section 8.2.2 the actual shape of the nucleus of comet 67P/Churyumov-Gerasimenko is used to study the effects of a rotating nucleus on dust grain behavior. The geometry of the nucleus affects not only the gravity near the nucleus, but also the surface area that can be illuminated by the sun. The activity map obtained in *Fougere et al.*

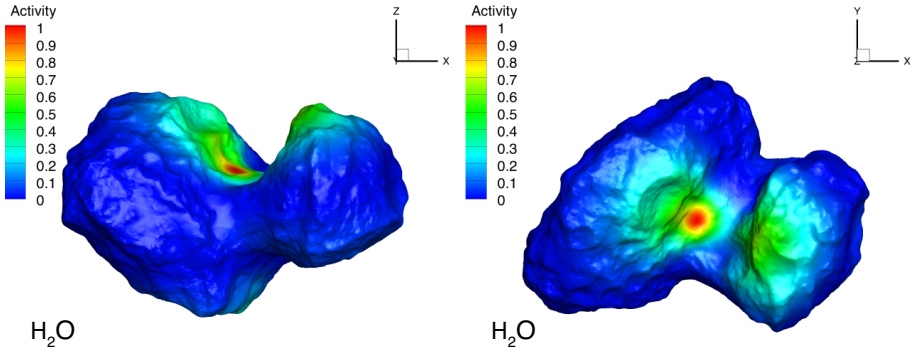

Figure 8.2: The activity map on the nucleus surface of comet 67P from *Fougere et al.* (2016).

(2016), combined with the changing solar zenith angle, provides the boundary condition on the surface, which is shown in Fig. 8.2. At some regions on the nucleus, the surface normal can be perpendicular to the direction of the gravity, which allows very large dust grains to leave the surface. At other locations where the gas flux is low and the gravity is large, heavy dust grains cannot be lifted by the gas. The maximum size of liftable dust grains can be calculated by the local flux and the gravity force in the normal direction of the surface, which is expressed as $a_{max} = \frac{3}{8}\frac{C_d z u_{out}}{\rho_g g_{normal}}$, where z is the local gas mass production rate, u_{out} is the normal velocity of gas, ρ_g is the bulk density of dust grains ($1\,\mathrm{g/cm^3}$ in this work) and g_{normal} is the normal component of the gravitational acceleration. If one dust fluid has a size larger than the local maximum liftable size, the density of that fluid is set to a small number and the velocity is set to zero. In addition, the model is run in the co-rotating frame of the comet to fully account for the rotational effects. Case 1 applies an imaginary condition when the sun is rotating with the comet at the same rate, to illustrate the effect of a fixed boundary condition. Case 2 is more realistic, with a revolving sun in the rotating frame, which results in a time-varying boundary condition. Our setup may be still different from the real solar and cometary condition, but it is enough for our purpose of a theoretical study.

8.1.1 Treatment of returning dust grains

Because of the varying surface boundary conditions, there are dust grains of the same size that can be lifted in some regions on the comet but cannot in other regions. Some of the lifted grains are carried away by the gas from the nucleus forever, but some on different trajectories may be lifted first and then at some point in space are subjected to more gravity than the dust drag force. These latter ones are called returning dust grains and will end up resting on the surface region unless the boundary condition changes to lift them again.

The returning dust grains can be treated in a straightforward way with the DSMC approach, but require special considerations in a fluid model. As vacuum is not allowed in fluid models, every dust fluid has to have a density at every point in the computational domain, even if it can never be lifted at the inner boundary. If no measure is taken, the very small amount of dust in the whole domain will be attracted to the nucleus and accelerated by the gravity, resulting in a density pile-up and a relatively high speed near the inner boundary. To minimize the numerical artificial effects, we prescribe a "free falling zone", which is a small zone compared to the whole domain. Inside the "free falling zone", returning dust grains or grains of unlifable sizes are allowed to fall back to the comet. Outside of that zone, if dust grains there cannot be dragged away by the gas, they will stay fixed at where they are. The "free falling zone" is within 15 km from the nucleus in this work.

8.2 Results and discussion

8.2.1 Comparison with the DSMC model

This section studies the differences and similarities between the results from our model and the DSMC model in *Tenishev et al.* (2011). Fig.8.3 shows the number densities of gas and dust grains in the vicinity of the nucleus and at a larger scale

obtained by our fluid model. We can spot density spikes in both dust number density figures, but not in figures of gas. The spike exists near the surface and grows bigger and more significant at a larger distance. Similar spikes can also be found in Fig. 8.4 from *Tenishev et al.* (2011), and are regarded as a signature of dust grains. It appears where sharp gradients in the water flux and temperature take place. The spike region has a lower velocity than the lower solar zenith angle (SZA) region and a resulting higher density than the higher SZA region. The velocity difference caused by the boundary condition is relatively large compared to the low dust velocity. Therefore, the spike cannot be found in gas figures and is also contributed by slower dust particles that drift from the higher gas flux to the lower gas flux region.

Fig.8.5 offers an example of returning dust grains close to the comet. The results are similar to those in Fig. 13 of Tenishev et al. (2011), which is reproduced in Fig. 8.6. Differences are due to the fluid nature of these calculations and the particle nature of the DSMC models. The sun is in the negative x-axis direction. Near x=0 km, the once lifted dust grains fall back to the nucleus. At the higher SZA region, dust grains that are originally in space get accelerated by gravity and are drawn toward the nucleus. The dust speed at the higher SZA region is comparable to that in the lower SZA region, but the density of accumulated dust grains on the night side is much lower than the day side. We also want to point out that our returning dust grains are fewer and travel a much shorter distance along the ground than those in the DSMC model. Our explanation is that the dust grains in the DMSC model can go in various directions at one point in space and those with a tangential velocity are more likely to return. In addition, the cells in DSMC model are much smaller than the fluid model near the surface. With individual dust particles there is more opportunity for small scale structures in the DSMC. However, in the fluid model, all dust grains of the same size are treated as one fluid and share a single bulk velocity. In our case, most of the lifted dust grains only have a radial velocity, which make it

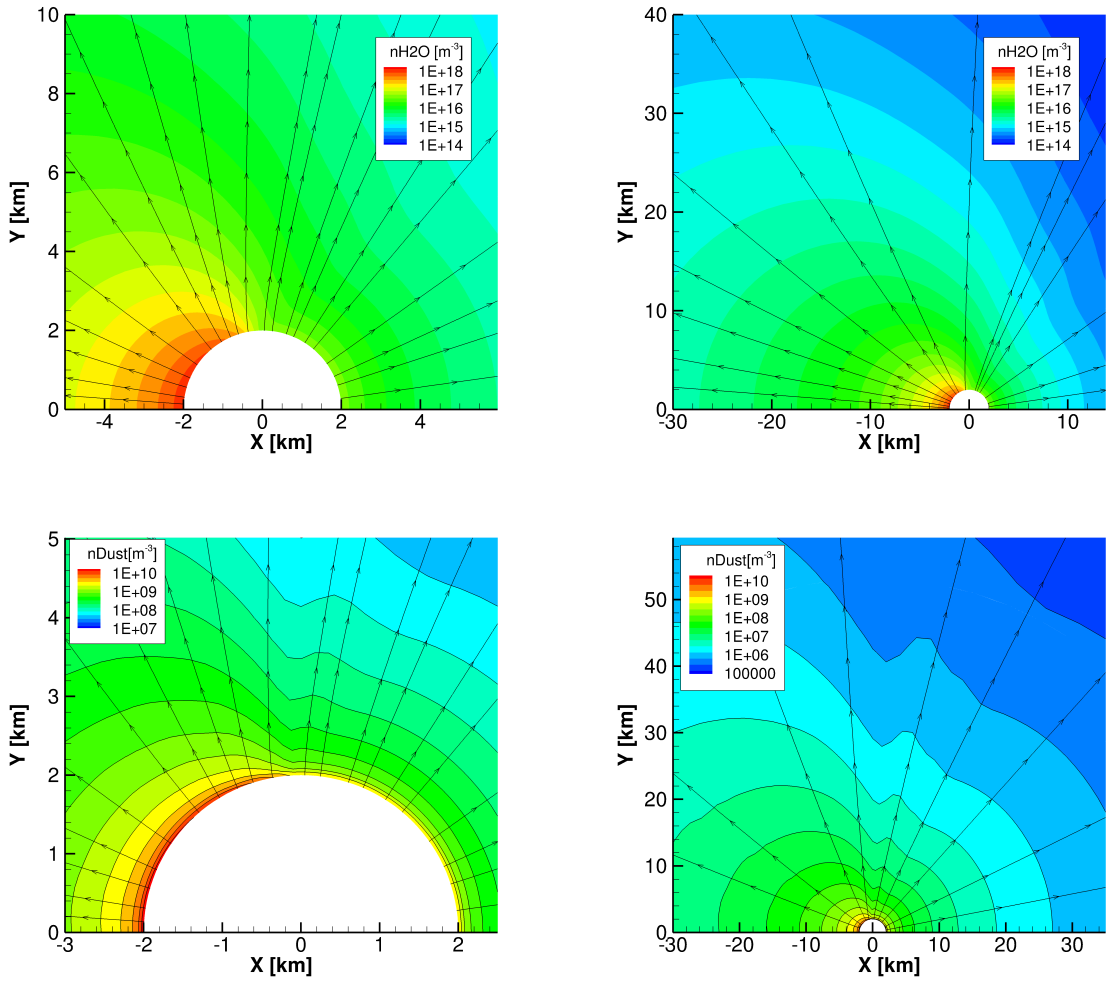

Figure 8.3: The number of densities of H_2O (upper panel) and all dust grains (lower panel) in the vicinity of the nucleus (left) and at a larger distance over 30 km (right) at a heliocentric distance of 1.3 AU. The solid black lines are contour lines and the solid black lines with arrows are streamlines of H_2O and dust velocities.

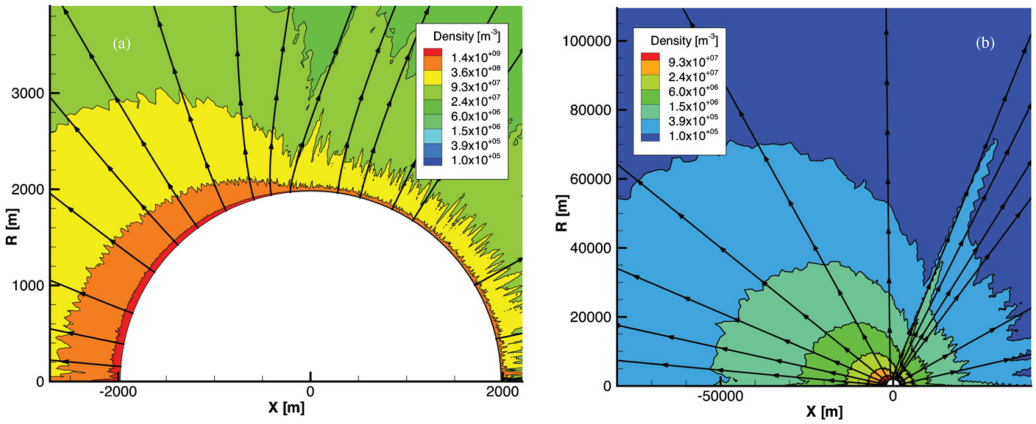

Figure 8.4: The total dust number density in the vicinity of the nucleus (left) and at a distance of up to 80$\tilde{\text{k}}$m from the nucleus (right) for the heliocentric distance of 1.3 AU, extracted from *Tenishev et al.* (2011).

difficult for them to return to the nucleus.

Figs.8.7-8.8 show the total dust number densities and the the mean dust speeds extracted from radial lines at several SZAs. The left column represents our model results and the right are the DSMC model results reproduced from *Tenishev et al.* (2011). The four rows represent four cases at different heliocentric distances: 1.3, 2.0, 2.7, and 3.3 AU, respectively.

In Fig.8.7, two columns show similar trends: densities drop more sharply within 20 km than beyond that distance; lines at a lower SZA tend to have a larger density. We also notice that the dust number densities in our model are about 2$\sim$3 times of that in the DSMC model. The major reason for the difference is the number of bins used to group dust grains by the radius or the resolution of dust particle. Since the dust number distribution follows the power law with an index of -3, i.e., $n(a) \sim a^{-3}$, the lower end of the spectrum has a higher number density. If the same amounts of dust mass are distributed into different bins of sizes by the same power law, each bin should have the same amount of mass, since the mass of the dust grain $m(a) \sim a^3$ and the mass density distribution is not dependent on size, $n(a)m(a) \sim 1$. Therefore, if the same amount of mass is distributed in fewer bins, the bins of the smaller size

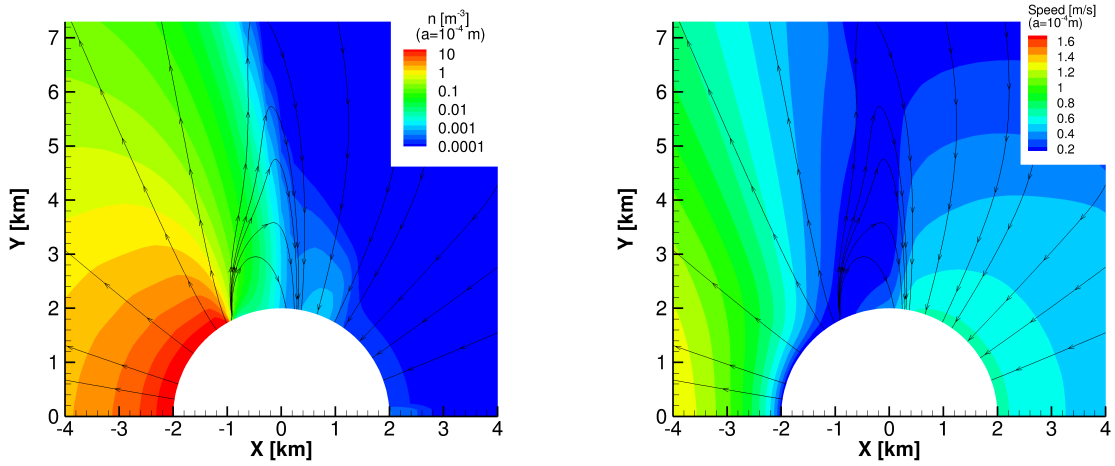

Figure 8.5: The number density and the speed of the dust grains with a radius of 10^{-4}m near the nucleus at a heliocentric distance of 2.7 AU.

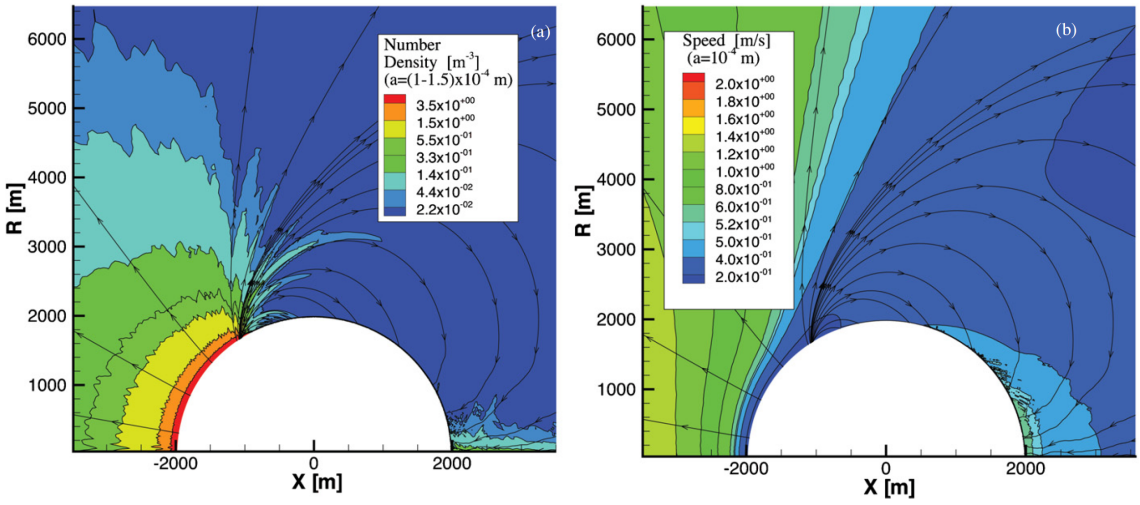

Figure 8.6: The total number density of dust grains integrated over the radius interval of (1-1.5)$\times 10^{-4}$ m and the speed of dust grains with radius of 10^{-4} m, reproduced from *Tenishev et al.* (2011).

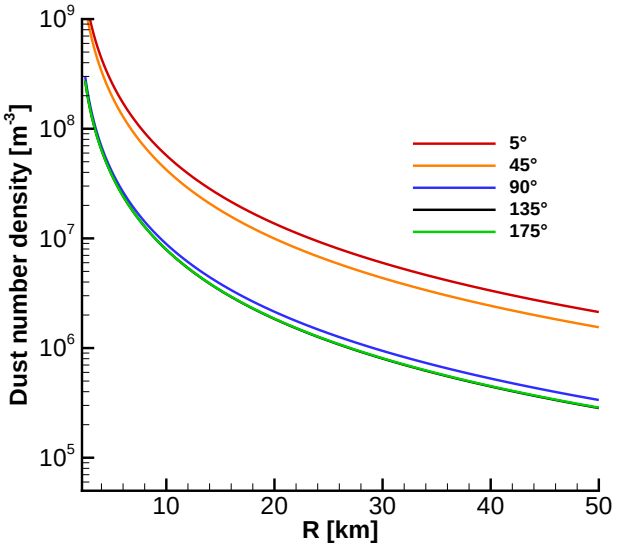
Dust number density [m^{-3}]
R [km]
5°
45°
90°
135°
175°

(a)

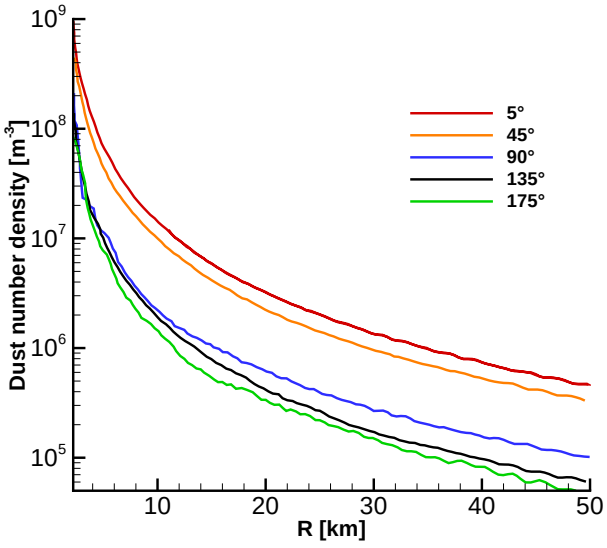
Dust number density [m^{-3}]
R [km]
5°
45°
90°
135°
175°

(b)

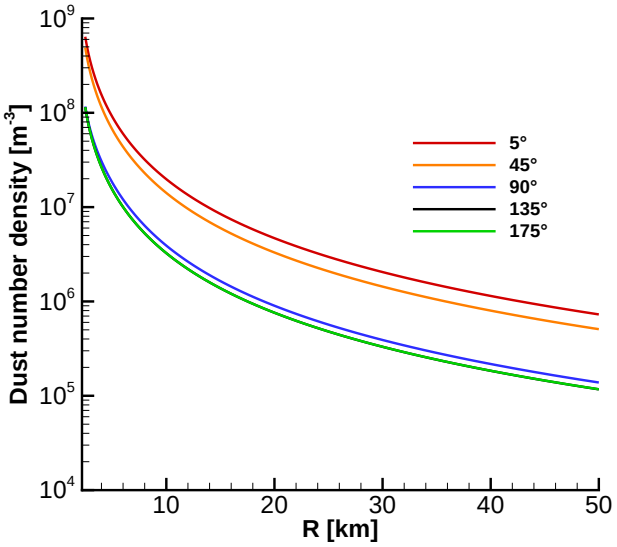
Dust number density [m^{-3}]
R [km]
5°
45°
90°
135°
175°

(c)

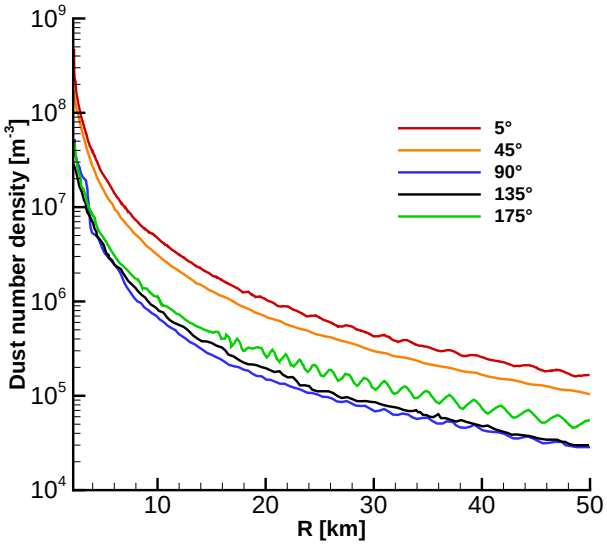
Dust number density [m^{-3}]
R [km]
5°
45°
90°
135°
175°

(d)

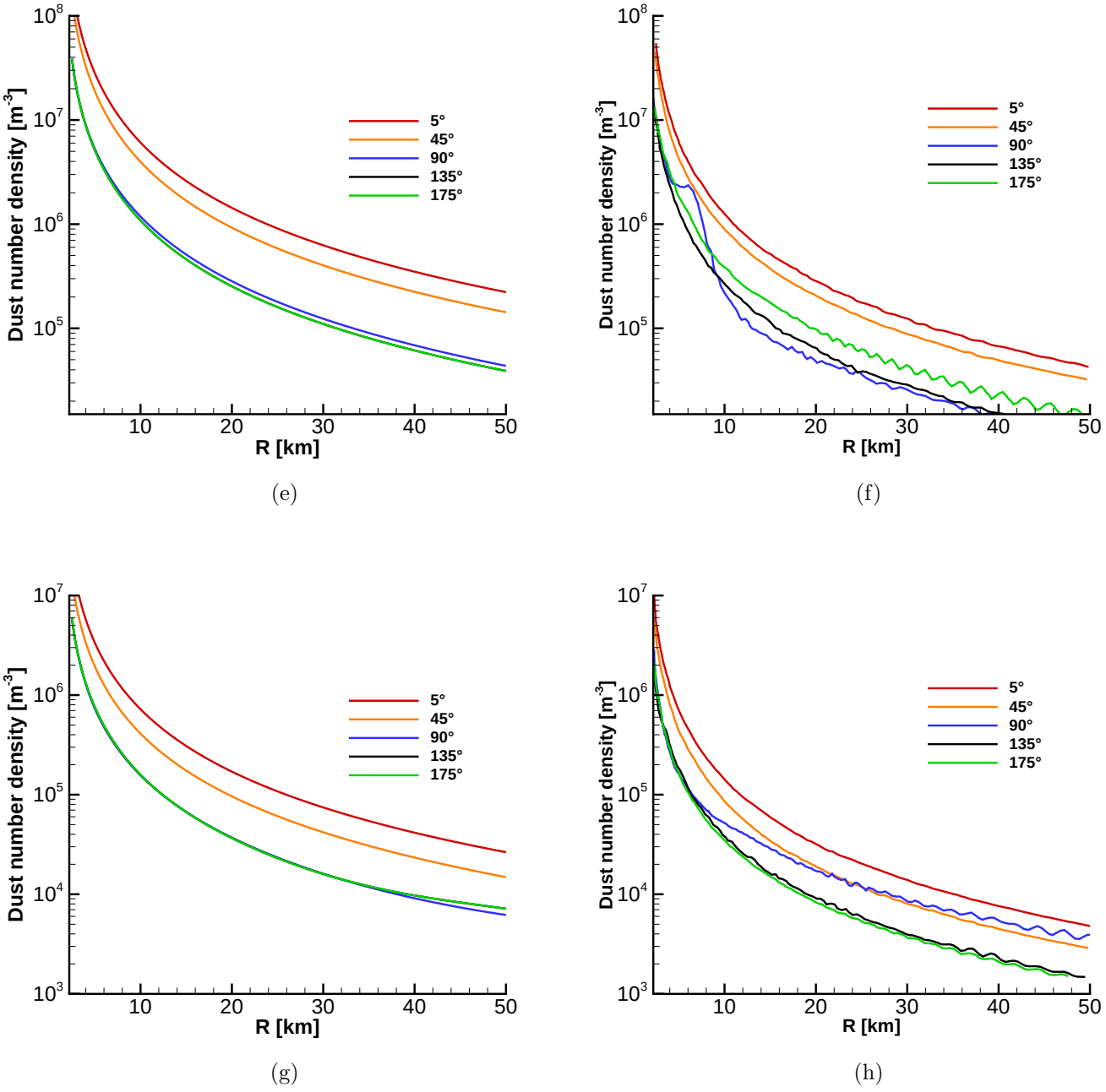

Figure 8.7: Dust number densities along radial lines at several subsolar angle as functions of cometocentric distance. The four rows represent four heliocentric distances of 1.3, 2.0, 2.7, and 3.3 AU respectively. The left column show our model results and the right column are reproduced from *Tenishev et al.* (2011).

receive more mass. For example, in the case of 6 bins, the 10^{-7}m sized grains have 1/6 of the total mass. Using the distribution function and increasing the number of logarithmically spaced discrete dust sizes to 40, now the 1/6 of the total mass will be distributed among bins of sizes ranging from $10^{-7}\tilde{\text{m}}$ to $10^{-6.25}\tilde{\text{m}}$. As a result, the same amount of mass creates fewer dust grains in the case of 40 bins than in the case of 6 bins. Our model has 6 logarithmically spaced discrete dust sizes, while the DSMC model has about 50 bins and has a continuous distribution of sizes within each bin rather than one size per bin. Following the reasoning above, we expect our model with fewer bins overestimates the total number density. One can also find that in the left column, the number density at the SZA of 90 degrees is higher than that at 135 and 175 degrees in almost all cases, while the most cases in the right column do not show the same pattern. It may be caused by the dust grains, which are ejected at the lower SZA region but fall back to the surface at the higher SZA region.

In Fig.8.8, the speeds in all plots increase sharply within 20 km, before reaching their terminal speeds. Similar to the behavior in the density plots, the speeds at lower SZAs are higher than those at larger angles, which are the results of the boundary condition on the nucleus surface and the almost radial expansion of the dust grains and gas. In the fluid model, the speeds at the SZAs of 135 and 175 degrees are very close, while the DSMC model has a higher speed at 135 degrees, which may indicate a more diffusive coma in the DSMC model, consistent with observations in other model comparison papers (*Bieler et al.*, 2015). In addition, there are probably more odd particles coming from various original locations in the DSMC returning onto the nightside in different orientations, compared with the fluid model. We also notice that the terminal speeds in the DSMC model are about 10% higher in most cases. It is likely to be caused by the dust grain's drag effect on H_2O, which is included in our model but not in the DSMC model.

Figs.8.9-8.10 show number densities and speeds of different sized dust grains at a

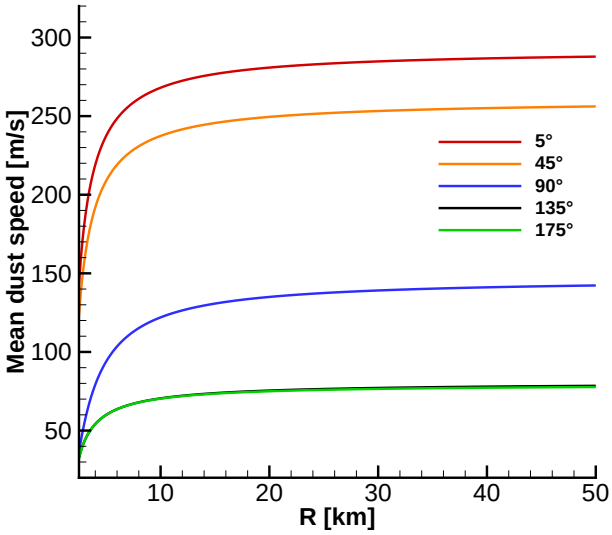
Mean dust speed [m/s]
R [km]
5°
45°
90°
135°
175°

(a)

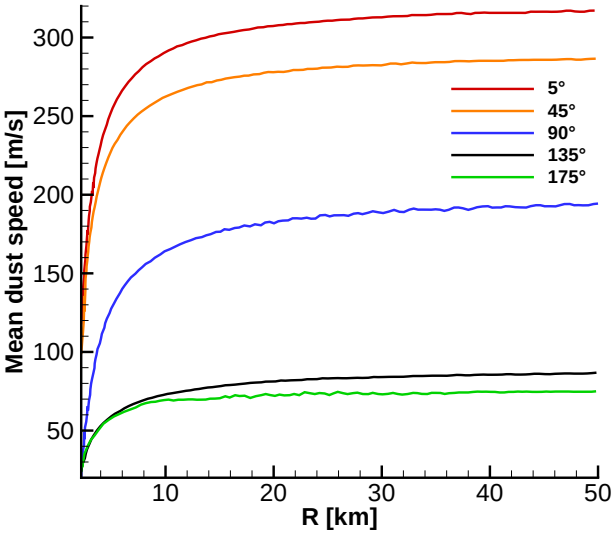
Mean dust speed [m/s]
R [km]
5°
45°
90°
135°
175°

(b)

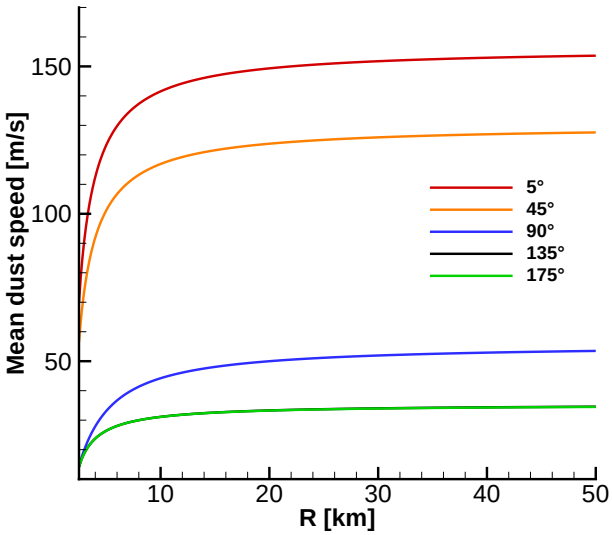
Mean dust speed [m/s]
R [km]
5°
45°
90°
135°
175°

(c)

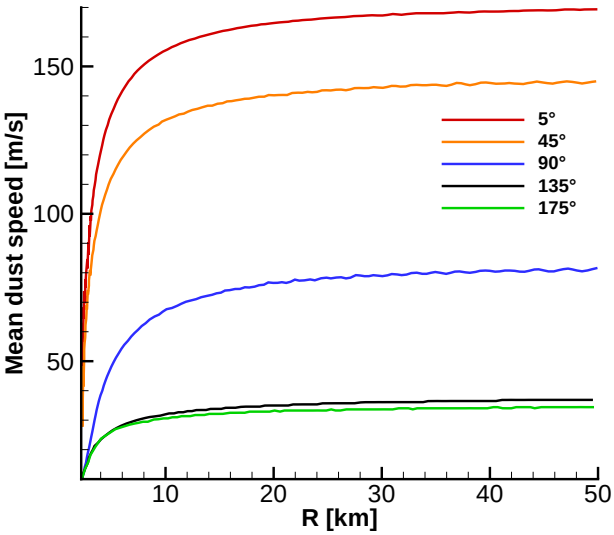
Mean dust speed [m/s]
R [km]
5°
45°
90°
135°
175°

(d)

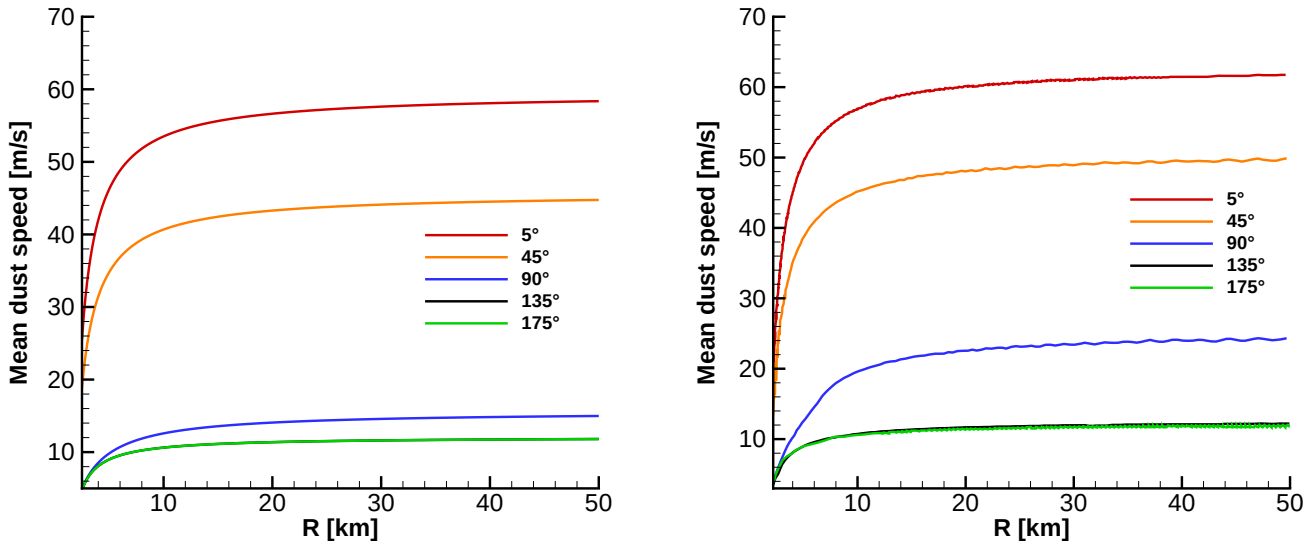

(e)

(f)

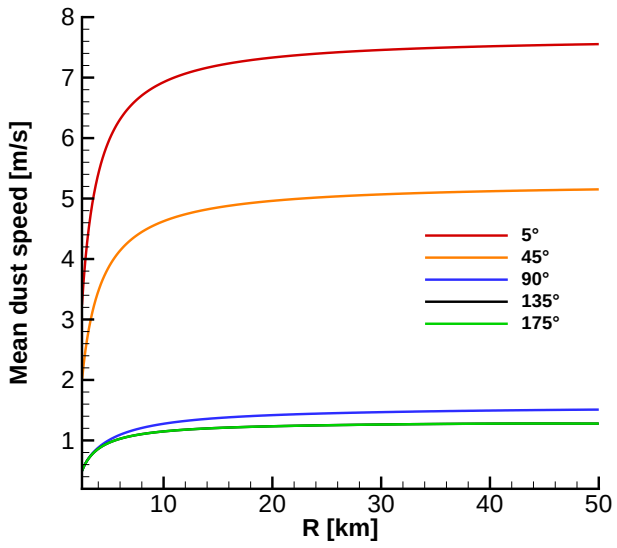

(g)

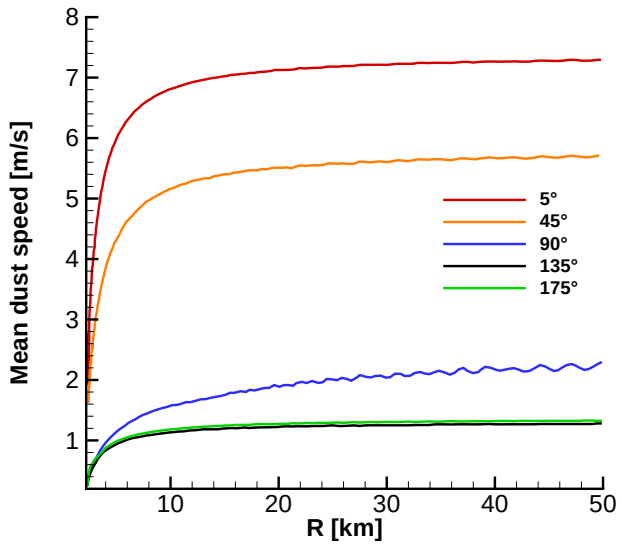

(h)

Figure 8.8: Mean dust speeds along radial lines at several subsolar angle as functions of cometocentric distance. The four rows represent four heliocentric distances of 1.3, 2.0, 2.7, and 3.3 AU respectively. The left column show our model results and the right column are reproduced from *Tenishev et al.* (2011).

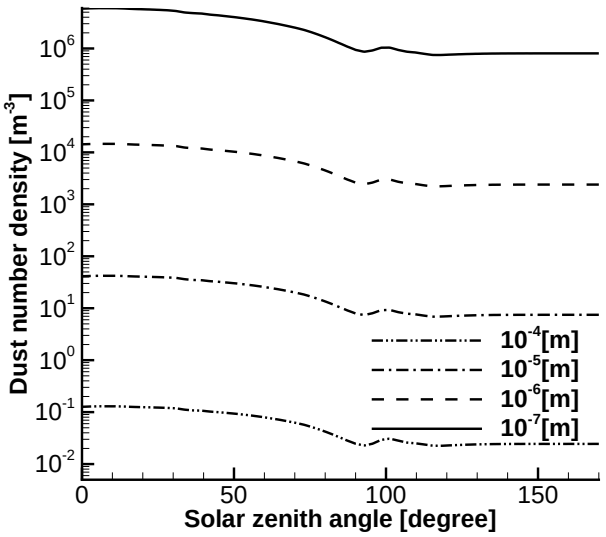
Dust number density [m-3]
Solar zenith angle [degree]
10-4[m]
10-5[m]
10-6[m]
10-7[m]

(a)

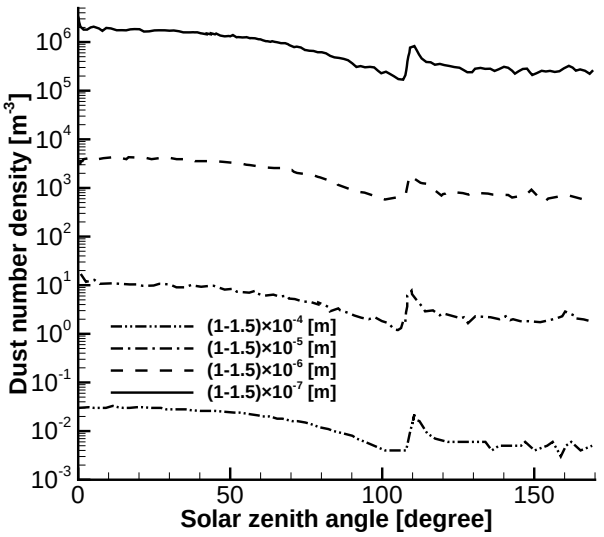
Dust number density [m-3]
Solar zenith angle [degree]
(1-1.5)×10-4 [m]
(1-1.5)×10-5 [m]
(1-1.5)×10-6 [m]
(1-1.5)×10-7 [m]

(b)

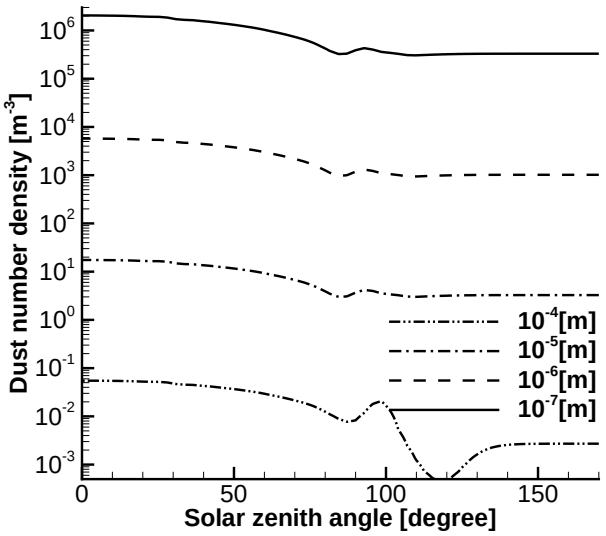
Dust number density [m-3]
Solar zenith angle [degree]
10-4[m]
10-5[m]
10-6[m]
10-7[m]

(c)

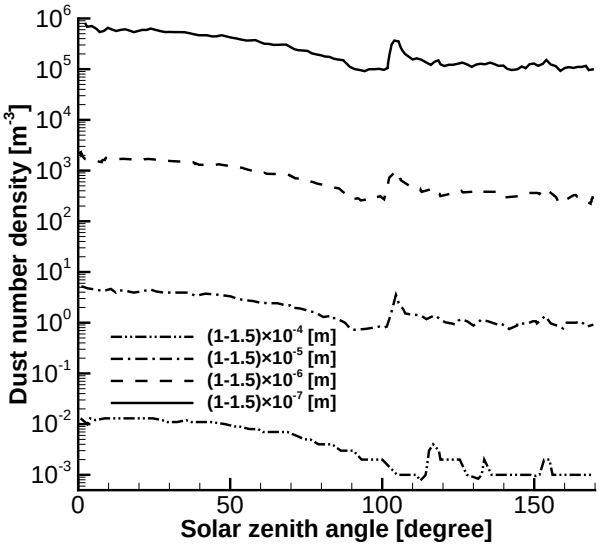
Dust number density [m-3]
Solar zenith angle [degree]
(1-1.5)×10-4 [m]
(1-1.5)×10-5 [m]
(1-1.5)×10-6 [m]
(1-1.5)×10-7 [m]

(d)

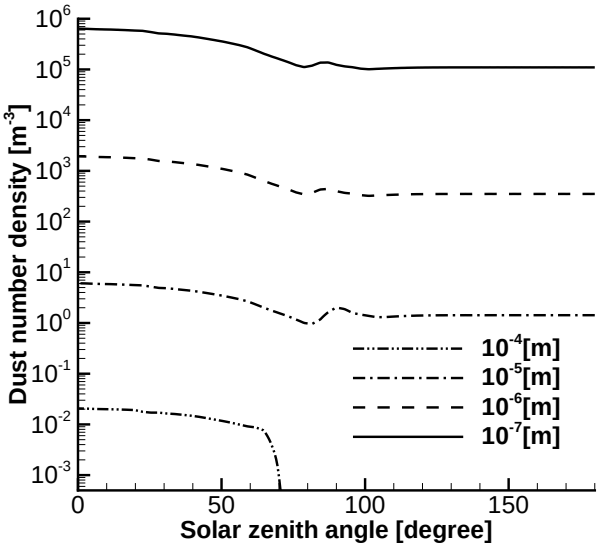

(e)

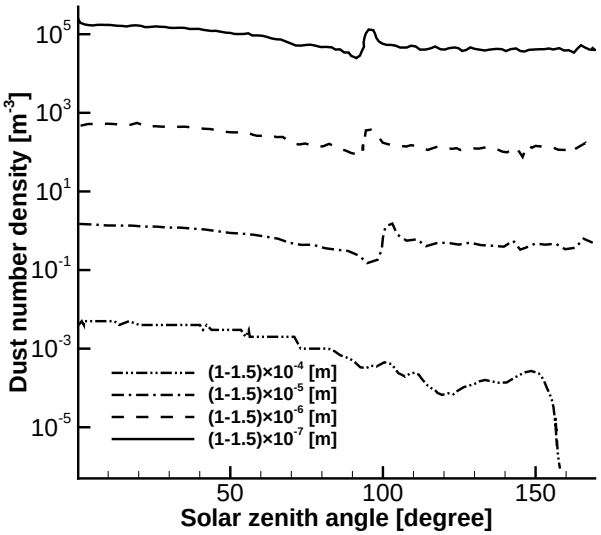

(f)

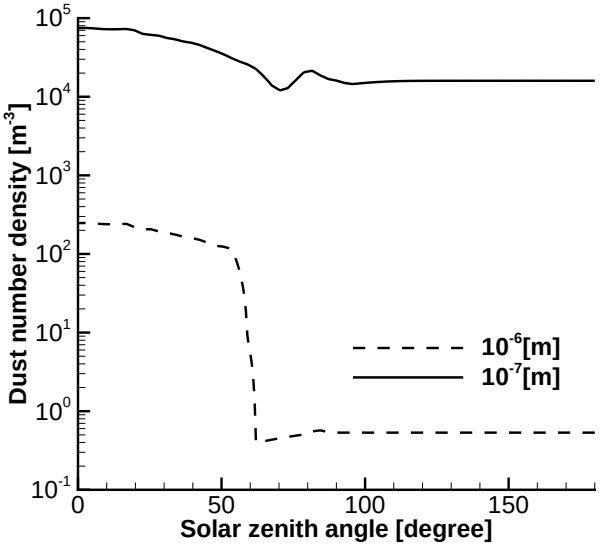

(g)

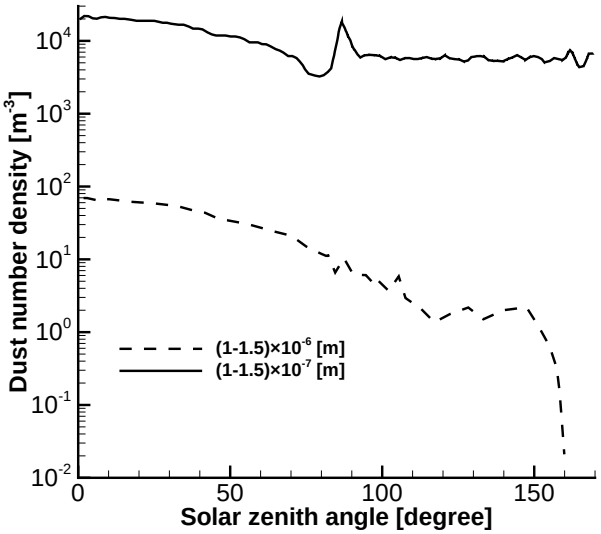

(h)

Figure 8.9: Dust number densities at a cometocentric distance of 30 km as functions of the solar zenith angle. The four rows represent four heliocentric distances of 1.3, 2.0, 2.7, and 3.3 AU respectively. The left column show our model results and the right column are reproduced from *Tenishev et al.* (2011).

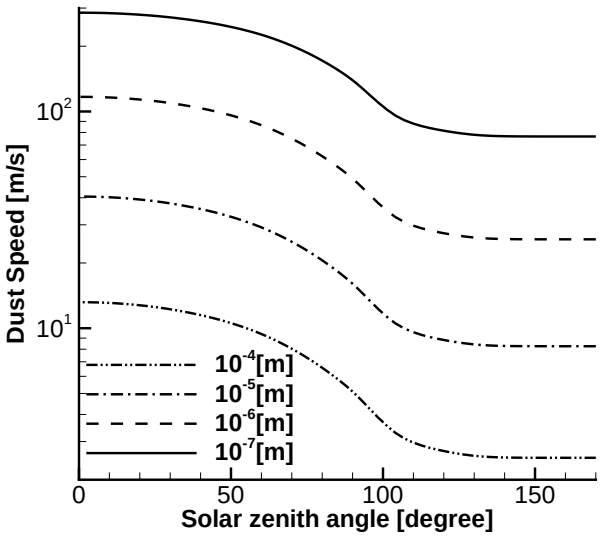
Dust Speed [m/s]
10^2
10^1
10^{-4}[m]
10^{-5}[m]
10^{-6}[m]
10^{-7}[m]
0
50
100
150
Solar zenith angle [degree]

(a)

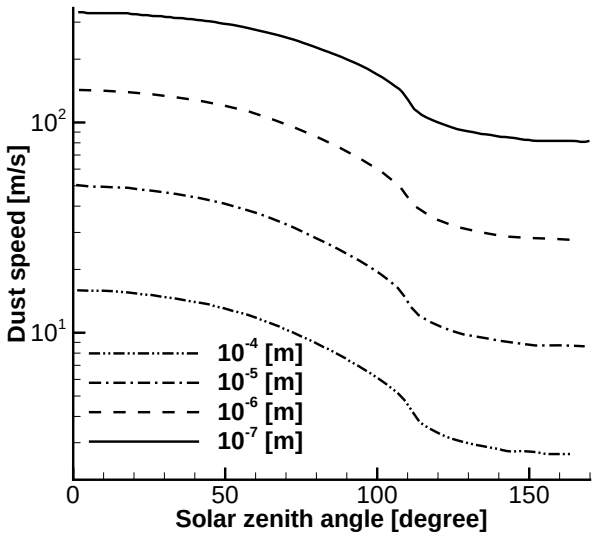
Dust speed [m/s]
10^2
10^1
10^{-4} [m]
10^{-5} [m]
10^{-6} [m]
10^{-7} [m]
0
50
100
150
Solar zenith angle [degree]

(b)

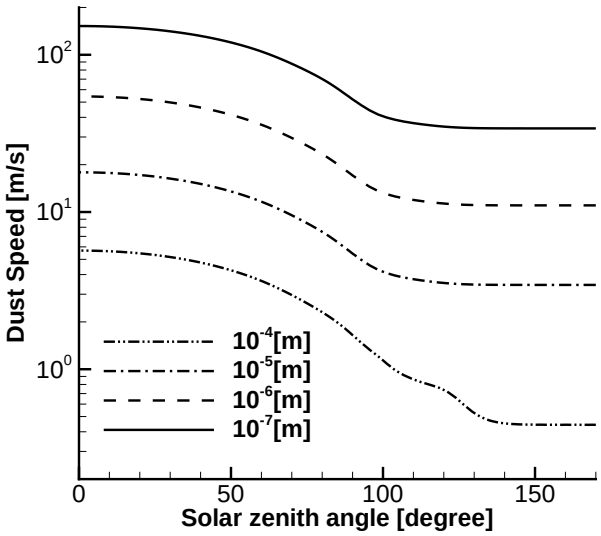
Dust Speed [m/s]
10^2
10^1
10^0
10^{-4}[m]
10^{-5}[m]
10^{-6}[m]
10^{-7}[m]
0
50
100
150
Solar zenith angle [degree]

(c)

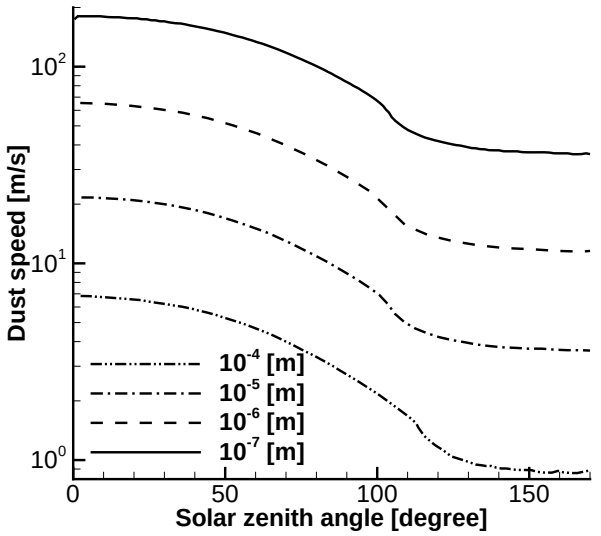
Dust speed [m/s]
10^2
10^1
10^0
10^{-4} [m]
10^{-5} [m]
10^{-6} [m]
10^{-7} [m]
0
50
100
150
Solar zenith angle [degree]

(d)

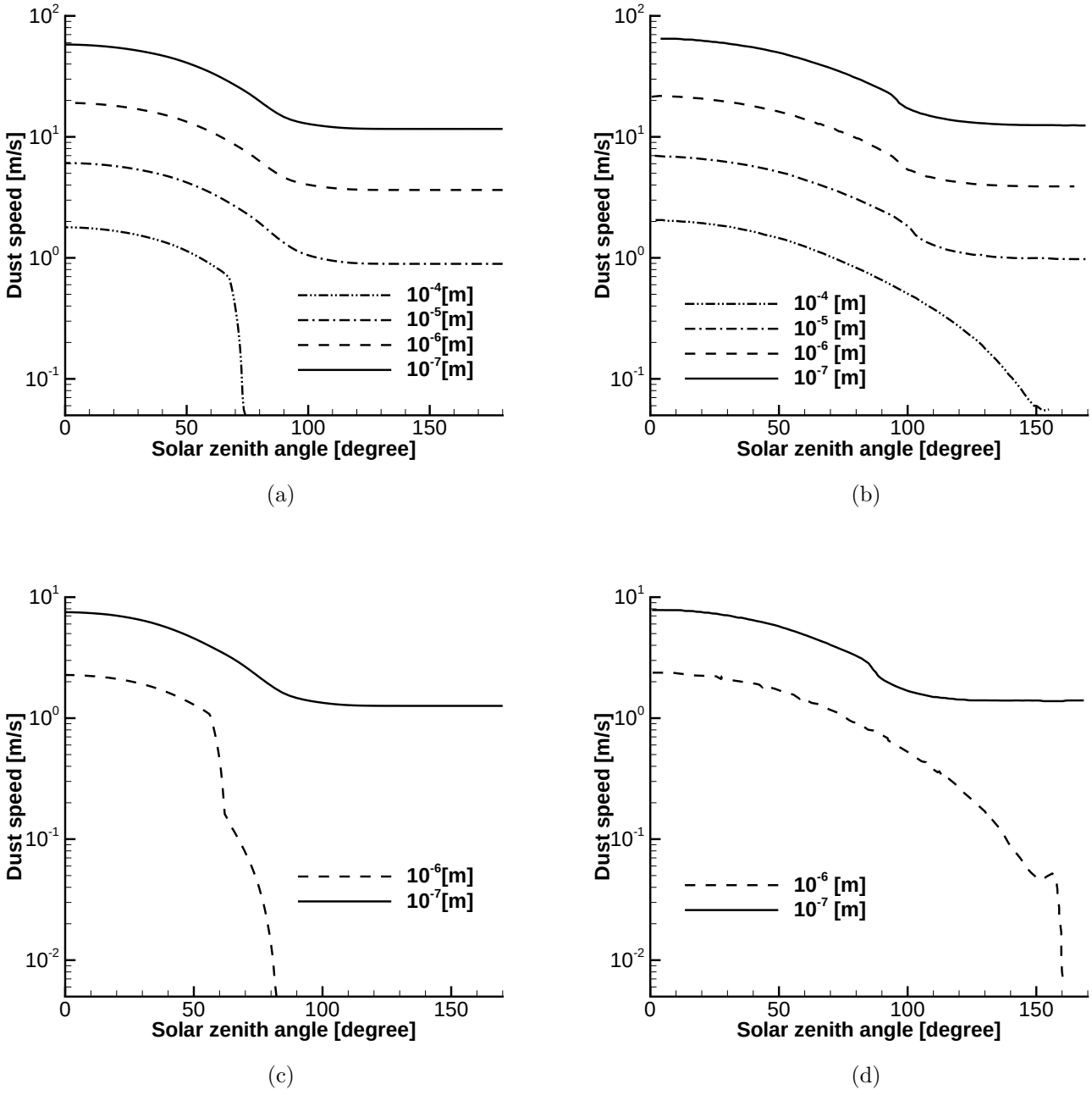

Figure 8.10: Dust number densities at a cometocentric distance of 30 km as functions of the solar zenith angle. The four rows represent four heliocentric distances of 1.3, 2.0, 2.7, and 3.3 AU respectively. The left column show our model results and the right column are reproduced from *Tenishev et al.* (2011).

distance of 30 km to the nucleus as a function of the SZA. Similar to the previous figures, the left column represents our model results and the right are from the DSMC model. The four rows represent four cases at four heliocentric distances: 1.3, 2.0, 2.7, and 3.3 AU, respectively. The expected difference in the dust number densities of neighboring sizes is about 3 orders of magnitude, according to the number distribution at the surface. Because of the difference in the velocities, the results have a difference in the number dust densities of neighboring sizes smaller than the expected value, indicating the number distribution in space is flatter than that at the boundary. In addition, both models display the classical dust speed's dependence on size, $v \sim a^{-0.5}$. If one group of dust grains have sizes 10 times than another group, the dust speed of the larger dust grains is about 1/3 of the smaller ones' speed.

From Figs.8.9-8.10, we can see that both models have quite similar profiles of dust densities and speeds, which in general have higher values at higher SZAs. Local maxima or spikes, corresponding to the spikes in the previous 2-D plot, are also spotted in the line plots of dust number densities from both models. The spikes in our model occur at a slightly lower SZA and appear less prominent than those in the DSMC model. For the dust grains that can be lifted, the variations in densities and speeds at different SZAs are less than one order of magnitude. Some large dust grains cannot be lifted on the nucleus surface beyond certain certain critical SZA, because their sizes exceeds the local maximum liftable size. As a result of the boundary condition, the densities and speeds of the large-sized dust grains are much lower beyond that critical SZA. The plots also show at 30 km from the comet, such critical SZAs exist in both model results as well. For example, in the 2.7 AU case, the critical SZA for 10^{-4} m dust grains at the inner boundary is about 70 degrees. Our fluid model shows at 30 km from the comet, the density and speed of 10^{-4} m sized dust grains appear to be cut off beyond 70 degree, while in the DSMC model, the cut-off occurs near 150 degree, with a less abrupt change in the speed profile. The difference

is likely to be caused by the limitation of the fluid model in treating the returning dust grains as we discussed before. The observation above indicates once again that dust grains in the DSMC model are more diffusive than those in our model, which we already mentioned in the previous discussion.

8.2.2 The effects of the cometary activity and rotation

This section studies the effects of the cometary activity and rotation on dust grain's behavior. Fig.8.11 shows the dust densities of 10^{-6}m and 10^{-3}m size at T=20 hours under different conditions of Case 1 (left)and Case 2 (right). We also want to restate here that in Case 1 the sun's subsolar point is fixed on the big end of the nucleus, while in Case 2 the sun is rotating around the nucleus with a period of 12.4 hours in the comet's reference frame.

In Fig.8.11 we can find that the density of 10^{-3}m sized dust grain shows a clear spiral pattern. In contrast, light and fast 10^{-3}m sized dust grains are not affected significantly by the cometary rotation, because their dust speed are much larger than the co-rotating speed of about 5 m/s at a distance of 40 km. We can also see the spiral pattern in Case 1 is much more prominent than Case 2. Case 2 has more spirals and more uniformly distributed dust grains. These results may suggest that if there is one dominant jet or activity independent of the solar illumination, a clear spiral pattern is highly probable to exist in the plane perpendicular to the rotating axis. The combination of the solar illumination and the nucleus rotation is also able to produce spirals, which may be more difficult to observe.

Fig.8.12 shows the speeds of different sized dust grains at distances of 30 km (left) and 50 km (right) from Case 2 as a function of the azimuthal angle ϕ. We find the 10^{-5}m-sized dust grains are consistently faster than the other two groups. Because of the cometary activity and rotation, the speeds of 10^{-3}m-sized and 10^{-4}m-sized dust grains are close to each other and do not reveal clear dependence on size as

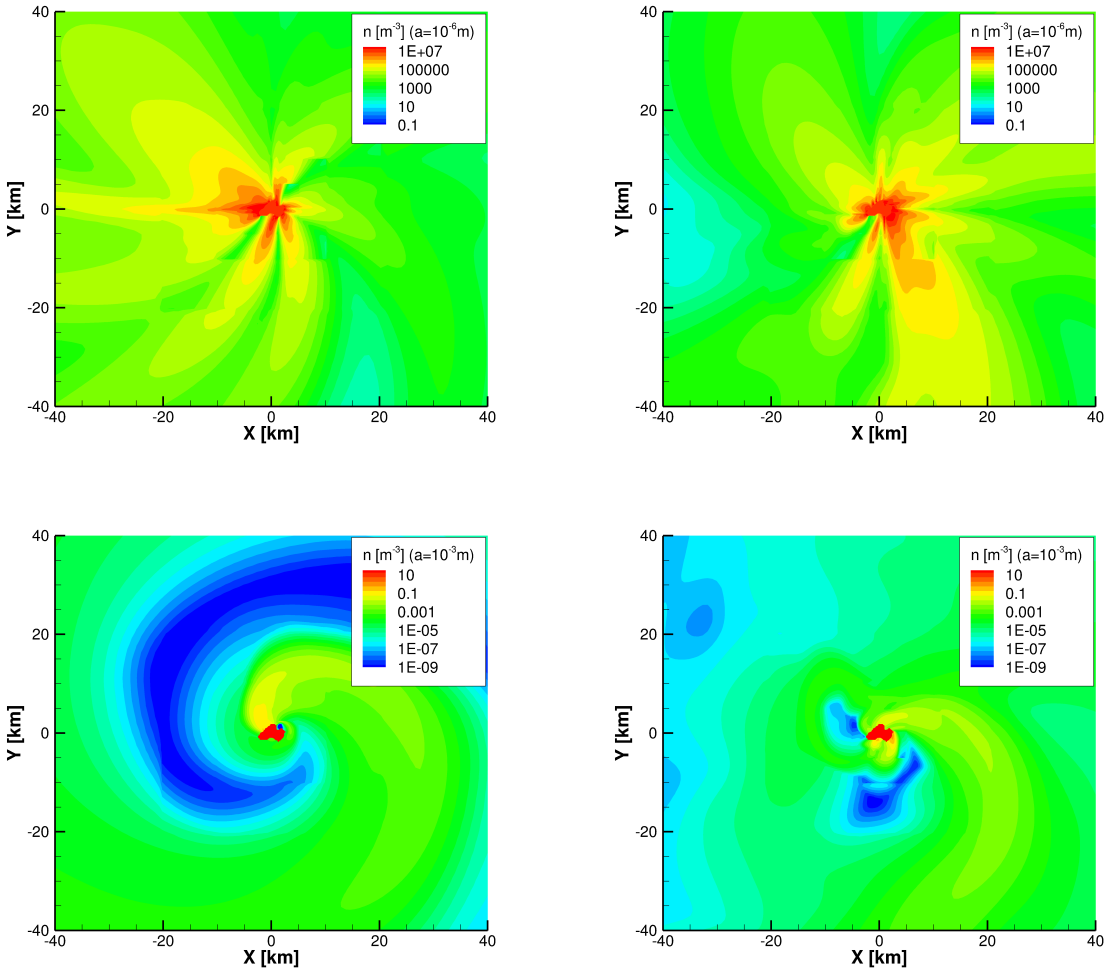

Figure 8.11: Number densities of dust grains with radii of 10^{-6}m (upper panel) and 10^{-3}m (lower panel) from Case 1 (left) and Case 2 (right).

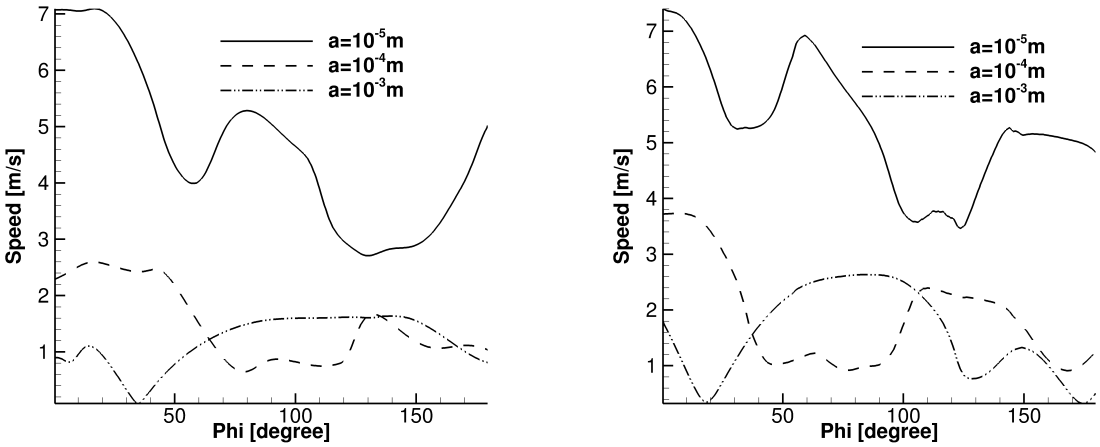

Figure 8.12: Speeds of 10^{-3} to 10^{-5}m sized dust grains at cometocentric distances of 30 km and 50 km from Case 2.

runs in section 8.2.1 do. A similar conclusion is also reached by dust measurements (*Rotundi et al.*, 2015). Some measurements were made in the coma of comet 67P by the impact sensor (IS) and the grain detection system (GDS) on GIADA, and are listed in Table 1 of their paper, which is reproduced here in Table 8.1. The GDS is able to detect dust grains when they pass through a laser curtain near the spacecraft, when the IS can measure the momentum of dust grains impacted on the plate of the sensor. GDS alone provides the speeds and optical cross-sections of grains. When it is combined with the IS momentum measurement, the dynamics of dust grains can be more accurately characterized than by one instrument. The measured dust grains have sizes within 10^{-4}m and 10^{-3}m and most of them are detected at cometocentric distances between 30 and 50 km. Our model may offer an interpretation as to why there is no clear dust speed dependence on size, as shown by the GIADA observations.

Table 8.1: GIADA GDS and IS observations made at heliocentric distances between 3.6 and 3.4 AU, reproduced from Table 1 of *Rotundi et al.* (2015). The event number, detected dust velocity and cross section, and the detection distance are listed.

Event number	dust velocity (m/s)	cross section (m^2)	cometocentric distance (km)
5	3.2	$5.6\pm1.9\times10^{-8}$	92.9
16	2.6	$1.4\pm0.4\times10^{-7}$	61.7
21	4.7	$2.3\pm1.2\times10^{-8}$	54.0
23	2.6	$9.2\pm3.0\times10^{-8}$	57.4
26	2.9	$2.7\pm1.9\times10^{-8}$	53.2
27	2.8	$7.4\pm2.3\times10^{-8}$	51.8
33	3.0	$3.1\pm0.3\times10^{-8}$	29.7
34	2.8	$7.4\pm0.6\times10^{-8}$	29.7
35	3.6	$3.1\pm1.6\times10^{-8}$	30.1

CHAPTER IX

Conclusion

In this thesis, we have introduced the complicated cometary environment that results from the interactions among neutral gases, plasma, and dust grains. The current understanding of the physical and chemical processes underlying the interactions are also revisited. As technologies advance and accurate observations accumulate, more mysterious phenomena tend to emerge, challenging our current understandings. Numerical models powered by supercomputers are in demand to interpret the observational data and test hypotheses proposed by new theories. Therefore, numerical models are indispensable in deepening our understanding despite being built on current knowledge.

Three models all using a fluid approach have been developed to study the plasma, neutral gas, and the dust grains, respectively. Many important and relevant physical and chemical processes are incorporated into the models. Tailored to specific needs, the three models have been applied to studying the problems arising in observations.

The plasma environment of comet C/2006 P1 (McNaught) is simulated using a multi-species MHD model over a wide range of heliocentric distances from 0.17 AU to 1.75 AU. The model input parameters are taken from various published observations, which should lead to reasonably realistic model results. The solar wind interaction of the comet at various locations is characterized and typical subsolar standoff dis-

tances of the bow shock and the contact surface are presented. Analytic solutions of bow shock and contact surface positions are also compared with the model results and show good agreement in general. These comparisons enable us to improve our understanding of the underlying physics of the plasma environment of the comet. In addition, we modified the computational mesh of the multi-species model for the case when the comet is at 0.7 AU so it can be compared with the measured water group ion abundances from the Ulysses/SWICS 1.7 AU down-tail from the comet and modeled velocity and temperature compared with the observations by Ulysses/SWOOPS. The model results show reasonable agreement with the observed water group ion abundances as well as the specific species abundance ratios. The similarity of the SWOOPS data across the tail and the model results is also displayed.

The multi-fluid neutral gas coma model is applied to comet 67P at various heliocentric distances and demonstrated that it produces comparable results as the DSMC model, which is based on a kinetic approach and physically correct in all collisional regimes encountered at the comet. Therefore, our model may serve as a powerful alternative to the particle-based model, especially for computationally intensive 3D and/or time dependent simulations.

As the model is capable of simulating the photochemical reactions and the redistribution of the excess energies via collisions in all collisional regimes, we are able to show the nonlinear relationship of production rate and heliocentric distance on the water expansion speeds. For the case at 1.0 AU, when the production rate is lower than $10^{28}\,\mathrm{s}^{-1}$, the increase in production rate will not make much difference. If the production rate is equal to or larger than $10^{29}\,\mathrm{s}^{-1}$, H_2O is accelerated and heated significantly by the photochemically produced hot daughter species, mostly atomic hydrogen. The variations in temperature and mean molecular mass along the cometocentric distances are also discussed. In addition, our results are comparable to previous model results and remote observations, suggesting validity and applicability

of the model to interpret cometary observations over a wide variety of production rates and heliocentric distances.

The new 3-D cometary dust model, which takes into account the major physics characterizing the dust-gas interaction, is compared with the DSMC model, which has been successfully applied to studying various cometary problems. The comparison shows a good agreement, and also illustrates the limitation of the fluid model in modeling the returning dust grains. In order to study the effects of the cometary activity and rotation, time-dependent simulations are run on a newly developed "roundcube" mesh in the rotating cometary reference frame. Our results reveal that a spiral pattern can be found for heavy and large dust grains. If a dominant jet persists on the comet, the spiral can be more prominent. Dust spirals can be an indicator of the particle size and the particle velocity, which may also give information about the local gas flux. In addition, the effect of rotation offers one explanation to the question why there is no clear dust speed dependence on size in some of the dust observations.

9.1 Future Work

Our models' capability of solving complex and time-dependent problems is demonstrated, showing the promising future applications to more complicated problems. In the future, the multi-fluid ion and the multi-fluid neutral models can be coupled together to treat the different scales of spatially extended OH^+, H_2O^+, O^+ and H^+ pickup effects on the solar-wind interaction with the comet. Combined with the roundcube mesh for rotation and the dust fluid model including sublimation, the multi-fluid neutral gas model can be used to study wide-scale ground-based images of daughter species. Charged dust models can be developed based on the neutral dust model and can also be coupled with multi-fluid ion model, in order to study the effect of charged dust on the cometary plasma environment.

As all of the three models are based on the BATSRUS code of the Space Weather

Modeling Framework (SWMF), coupling between them can be implemented easily. In addition, the powerful framework can also make challenging numerical simulation feasible and efficient. For example, it is difficult to couple the heavy dust grains moving at 10 m/s with the normal solar wind plasma, which has a speed of 400 km/s. As in time-dependent simulations the global time step is determined by the fastest fluid, a huge computational inefficiency is introduced by the large differences in speeds of different fluids. However, in the SWMF the plasma and the dust grains can run in two separate codes with their own time steps but on the same grid. The two codes can exchange information with each other to calculate the coupling terms at a certain frequency. Therefore, the model coupling can be done in a physical and efficient way in the SWMF.

APPENDIX

APPENDIX A

Selected Publications

1. Shou, Y., et al. (2016), A New 3D Multi-fluid Model: A Study of Kinetic Effects and Variations of Physical Conditions in the Cometary Coma, *ApJ*, *833*, 160, doi: 10.3847/1538-4357/833/2/160

2. Shou, Y., M. Combi, Y.-D. Jia, T. Gombosi, G. Toth, and M. Rubin (2015), The Plasma Environment in Comets over a Wide Range of Heliocentric Distances: Application to Comet C/2006 P1 (McNaught), *ApJ*, *809*, 156, doi: 10.1088/0004-637X/809/2/156

3. Huang, Z., et al. (2016), Four-fluid MHD simulations of the plasma and neutral gas environment of comet 67P/Churyumov-Gerasimenko near perihelion, *Journal of Geophysical Research (Space Physics)*, *121*, 4247–4268, doi: 10.1002/2015JA022333

4. Jia, Y.-D., C. Russell, W. Liu, and Y. Shou (2014), Multi-fluid model of a sun-grazing comet in the rapidly ionizing, magnetized low corona, *The Astrophysical Journal*, *796*(1), 42

5. Rubin, M., et al. (2014a), Comet 1P/Halley Multifluid MHD Model for the Giotto Fly-by, *ApJ*, *781*, 86, doi: 10.1088/0004-637X/781/2/86

BIBLIOGRAPHY

BIBLIOGRAPHY

A'Hearn, M. F., et al. (2012), Cometary volatiles and the origin of comets, *The Astrophysical Journal*, *758*(1), 29.

Alfvén, H. (1957), On the theory of comet tails., *Tellus*, *9*.

Bagdonat, T., and U. Motschmann (2002), 3d hybrid simulation code using curvilinear coordinates, *Journal of Computational Physics*, *183*(2), 470 – 485, doi: http://dx.doi.org/10.1006/jcph.2002.7203.

Bame, S. J., et al. (1986), Comet Giacobini-Zinner - Plasma description, *Science*, *232*, 356–361, doi: 10.1126/science.232.4748.356.

Bieler, A., et al. (2015), Comparison of 3D kinetic and hydrodynamic models to ROSINA-COPS measurements of the neutral coma of 67P/Churyumov-Gerasimenko, *A&A*, *583*, A7, doi: 10.1051/0004-6361/201526178.

Biermann, L. (1951), Kometenschweife und solare Korpuskularstrahlung, *ZAp*, *29*, 274.

Biermann, L., B. Brosowski, and H. U. Schmidt (1967), The interactions of the solar wind with a comet, *Sol. Phys.*, *1*, 254–284, doi: 10.1007/BF00150860.

Bird, G. (1994), *Molecular Gas Dynamics and the Direct Simulation of Gas Flows*, no. v. 1 in Molecular Gas Dynamics and the Direct Simulation of Gas Flows, Clarendon Press.

Biver, N., D. Bockelée-Morvan, P. Colom, J. Crovisier, G. Paubert, A. Weiss, and H. Wiesemeyer (2011), Molecular investigations of comets c/2002 x5 (kudo-fujikawa), c/2002 v1 (neat), and c/2006 p1 (mcnaught) at small heliocentric distances, *Astronomy & Astrophysics*, *528*, A142.

Biver, N., et al. (2002), The 1995 2002 Long-Term Monitoring of Comet C/1995 O1 (HALE BOPP) at Radio Wavelength, *Earth Moon and Planets*, *90*, 5–14, doi: 10.1023/A:1021599915018.

Bockelee-Morvan, D., and J. Crovisier (1987), The role of water in the thermal balance of the coma, in *Diversity and Similarity of Comets*, *ESA Special Publication*, vol. 278, edited by E. J. Rolfe and B. Battrick.

Bockelee-Morvan, D., J. Crovisier, and E. Gerard (1990), Retrieving the coma gas expansion velocity in P/Halley, Wilson (1987 VII) and several other comets from the 18-cm OH line shapes, *A&A*, *238*, 382–400.

Burns, J. A., P. L. Lamy, and S. Soter (1979), Radiation forces on small particles in the solar system, *icarus*, *40*, 1–48, doi: 10.1016/0019-1035(79)90050-2.

Calhoun, D. A., C. Helzel, and R. J. LeVeque (2008), Logically rectangular grids and finite volume methods for pdes in circular and spherical domains, *SIAM review*, *50*(4), 723–752.

Capaccioni, F., et al. (2015), The organic-rich surface of comet 67p/churyumov-gerasimenko as seen by virtis/rosetta, *Science*, *347*(6220), doi: 10.1126/science.aaa0628.

Combi, M. (2002), Hale-Bopp: What Makes a Big Comet Different? Coma Dynamics: Observations and Theory, *Earth Moon and Planets*, *89*, 73–90, doi: 10.1023/A:1021534117319.

Combi, M. R. (1987), Sources of cometary radicals and their jets - Gases or grains, *icarus*, *71*, 178–191, doi: 10.1016/0019-1035(87)90171-0.

Combi, M. R. (1996), Time-Dependent Gas Kinetics in Tenuous Planetary Atmospheres: The Cometary Coma, *icarus*, *123*, 207–226, doi: 10.1006/icar.1996.0150.

Combi, M. R., and A. H. Delsemme (1980), Neutral cometary atmospheres. I - an average random walk model for photodissociation in comets, *ApJ*, *237*, 633–640, doi: 10.1086/157909.

Combi, M. R., K. Kabin, D. L. Dezeeuw, T. I. Gombosi, and K. G. Powell (1999), Dust-Gas Interrelations In Comets: Observations And Theory, *Earth Moon and Planets*, *79*, 275–306, doi: 10.1023/A:1006257922294.

Combi, M. R., W. M. Harris, and W. H. Smyth (2004), *Gas dynamics and kinetics in the cometary coma: theory and observations*, pp. 523–552, University of Arizona Press.

Combi, M. R., Z. Boyd, Y. Lee, T. S. Patel, J.-L. Bertaux, E. Quémerais, and J. T. T. Mäkinen (2011), SOHO/SWAN observations of comets with small perihelia: C/2002 V1 (NEAT), C/2002 X5 (Kudo-Fujikawa), 2006 P1 (McNaught) and 96P/Machholz 1, *icarus*, *216*, 449–461, doi: 10.1016/j.icarus.2011.09.019.

Cravens, T. E. (1986), The physics of the cometary contact surface, in *ESLAB Symposium on the Exploration of Halley's Comet*, vol. 250, pp. 241–246.

Crifo, J. F. (1995), A general physicochemical model of the inner coma of active comets. 1: Implications of spatially distributed gas and dust production, *ApJ*, *445*, 470–488, doi: 10.1086/175712.

Crifo, J. F., G. A. Loukianov, A. V. Rodionov, and V. V. Zakharov (2003), Navier-Stokes and direct Monte Carlo simulations of the circumnuclear coma II. Homogeneous, aspherical sources, *icarus*, *163*, 479–503, doi: 10.1016/S0019-1035(03)00041-1.

Crifo, J.-F., G. A. Loukianov, A. V. Rodionov, and V. V. Zakharov (2005), Direct Monte Carlo and multifluid modeling of the circumnuclear dust coma. Spherical grain dynamics revisited, *icarus*, *176*, 192–219, doi: 10.1016/j.icarus.2005.01.003.

Crovisier, J. (1984), The Water Molecule in Comets: Fluorescence Mechanisms and Thermodynamics of the Inner Coma, *A&A*, *135*.

Davidsson, B. J. R., and P. J. Gutiérrez (2005), Nucleus properties of Comet 67P/Churyumov Gerasimenko estimated from non-gravitational force modeling, *icarus*, *176*, 453–477, doi: 10.1016/j.icarus.2005.02.006.

Davidsson, B. J. R., and P. J. Gutiérrez (2006), Non-gravitational force modeling of Comet 81P/Wild 2. I. A nucleus bulk density estimate, *icarus*, *180*, 224–242, doi: 10.1016/j.icarus.2005.07.023.

Festou, M. C. (1981), The density distribution of neutral compounds in cometary atmospheres. I - Models and equations, *A&A*, *95*, 69–79.

Flammer, K. R., and D. A. Mendis (1991), A note on the mass-loaded MHD flow of the solar wind towards a cometary nucleus, *Ap&SS*, *182*, 155–162, doi: 10.1007/BF00646450.

Fougere, N., M. R. Combi, V. Tenishev, M. Rubin, B. P. Bonev, and M. J. Mumma (2012), Understanding measured water rotational temperatures and column densities in the very innermost coma of Comet 73P/Schwassmann-Wachmann 3 B, *icarus*, *221*, 174–185, doi: 10.1016/j.icarus.2012.07.019.

Fougere, N., et al. (2016), Three-dimensional direct simulation Monte-Carlo modeling of the coma of comet 67P/Churyumov-Gerasimenko observed by the VIRTIS and ROSINA instruments on board Rosetta, *A&A*, *588*, A134, doi: 10.1051/0004-6361/201527889.

Galeev, A., T. Cravens, and T. Gombosi (1985), Solar wind stagnation near comets, *The Astrophysical Journal*, *289*, 807–819.

Gloeckler, G., J. Geiss, N. A. Schwadron, L. A. Fisk, T. H. Zurbuchen, F. M. Ipavich, R. von Steiger, H. Balsiger, and B. Wilken (2000), Interception of comet Hyakutake's ion tail at a distance of 500 million kilometres, *Nature*, *404*, 576–578.

Gombosi, T. I. (1999), *Physics of the Space Environment*, Cambridge University Press.

Gombosi, T. I. (2015), *Physics of Cometary Magnetospheres*, pp. 169–188, John Wiley & Sons, Inc, doi: 10.1002/9781118842324.ch10.

Gombosi, T. I., T. E. Cravens, and A. F. Nagy (1985), Time-dependent dusty gas-dynamical flow near cometary nuclei, *ApJ*, *293*, 328–341, doi: 10.1086/163240.

Gombosi, T. I., A. F. Nagy, and T. E. Cravens (1986), Dust and neutral gas modeling of the inner atmospheres of comets, *Reviews of Geophysics*, *24*, 667–700, doi: 10.1029/RG024i003p00667.

Gombosi, T. I., D. L. De Zeeuw, R. M. Häberli, and K. G. Powell (1996), Three-dimensional multiscale MHD model of cometary plasma environments, *J. Geophys. Res.*, *101*, 15,233–15,252, doi: 10.1029/96JA01075.

Grad, H. (1949), On the kinetic theory of rarefied gases, *Communications on Pure and Applied Mathematics*, *2*(4), 331–407, doi: 10.1002/cpa.3160020403.

Häberli, R. M., K. Altwegg, H. Balsiger, and J. Geiss (1995), Physics and chemistry of ions in the pile-up region of comet P/Halley., *A&A*, *297*, 881.

Häberli, R. M., K. Altwegg, H. Balsiger, and J. Geiss (1996), Heating of the thermal electrons in the coma of comet p/halley, *Journal of Geophysical Research: Space Physics*, *101*(A7), 15,579–15,589, doi: 10.1029/96JA01191.

Häberli, R. M., M. R. Combi, T. I. Gombosi, D. L. De Zeeuw, and K. G. Powell (1997), Quantitative analysis of h 2 o+ coma images using a multiscale mhd model with detailed ion chemistry, *Icarus*, *130*(2), 373–386.

Hansen, K., T. Bagdonat, U. Motschmann, C. Alexander, M. Combi, T. Cravens, T. Gombosi, Y.-D. Jia, and I. Robertson (2007), The plasma environment of comet 67p/churyumov-gerasimenko throughout the rosetta main mission, *Space Science Reviews*, *128*(1-4), 133–166.

Harris, W. M., F. Scherb, E. Mierkiewicz, R. Oliversen, and J. Morgenthaler (2002), Production, Outflow Velocity, and Radial Distribution of H_2O and OH in the Coma of Comet C/1995 O1 (Hale-Bopp) from Wide-Field Imaging of OH, *ApJ*, *578*, 996–1008, doi: 10.1086/342648.

Haser, L. (1957), Distribution d'intensité dans la tête d'une comète, *Bulletin de la Societe Royale des Sciences de Liege*, *43*, 740–750.

Huang, Z., et al. (2016), Four-fluid MHD simulations of the plasma and neutral gas environment of comet 67P/Churyumov-Gerasimenko near perihelion, *Journal of Geophysical Research (Space Physics)*, *121*, 4247–4268, doi: 10.1002/2015JA022333.

Huddleston, D. E., A. J. Coates, and A. D. Johnstone (1992), Predictions of the solar wind interaction with Comet Grigg-Skjellerup, *Geophys. Res. Lett.*, *19*, 837–840, doi: 10.1029/92GL00639.

Huebner, W. F., and W. J. Markiewicz (2000), NOTE: The Temperature and Bulk Flow Speed of a Gas Effusing or Evaporating from a Surface into a Void after Reestablishment of Collisional Equilibrium, *icarus*, *148*, 594–596, doi: 10.1006/icar.2000.6522.

Huebner, W. F., J. J. Keady, and S. Lyon (1992), Solar photo rates for planetary atmospheres and atmospheric pollutants, *Astrophysics and Space Science*, *195*(1), 1–294.

Hynds, R. J., S. W. H. Cowley, T. R. Sanderson, K.-P. Wenzel, and J. J. van Rooijen (1986), Observations of energetic ions from comet Giacobini-Zinner, *Science*, *232*, 361–365, doi: 10.1126/science.232.4748.361.

Ip, W.-H. (2004), *Global solar wind interaction and ionospheric dynamics*, pp. 605–629, University of Arizona Press.

Ip, W.-H., and W. I. Axford (1982), *Theories of physical processes in the cometary comae and ion tails*, pp. 588–634.

Ip, W.-H., and W. I. Axford (1987), The formation of a magnetic-field-free cavity at Comet Halley, *Nature*, *325*, 418, doi: 10.1038/325418a0.

Jia, Y.-D. (2007), *The magnetohydrodynamics of cometary plasma*, University of Michigan.

Jia, Y.-D., M. R. Combi, K. C. Hansen, and T. I. Gombosi (2007), A global model of cometary tail disconnection events triggered by solar wind magnetic variations, *Journal of Geophysical Research: Space Physics (1978–2012)*, *112*(A5).

Jia, Y. D., C. T. Russell, L. K. Jian, W. B. Manchester, O. Cohen, A. Vourlidas, K. C. Hansen, M. R. Combi, and T. I. Gombosi (2009), Study of the 2007 April 20 CME-Comet Interaction Event with an MHD Model, *ApJ*, *696*, L56–L60, doi: 10.1088/0004-637X/696/1/L56.

Jia, Y.-D., C. Russell, W. Liu, and Y. Shou (2014), Multi-fluid model of a sun-grazing comet in the rapidly ionizing, magnetized low corona, *The Astrophysical Journal*, *796*(1), 42.

Jones, G. H., A. Balogh, and T. S. Horbury (2000), Identification of comet Hyakutake's extremely long ion tail from magnetic field signatures, *Nature*, *404*, 574–576.

Kitamura, Y. (1986), Axisymmetric dusty gas jet in the inner coma of a comet, *icarus*, *66*, 241–257, doi: 10.1016/0019-1035(86)90155-7.

Koenders, C., K.-H. Glassmeier, I. Richter, U. Motschmann, and M. Rubin (2013), Revisiting cometary bow shock positions, *Planetary and Space Science*, *87*, 85–95.

Lee, M. A. (1989), Ultra-low frequency waves at comets, *Washington DC American Geophysical Union Geophysical Monograph Series*, *53*, 13–29, doi: 10.1029/GM053p0013.

Ma, Y., A. F. Nagy, I. V. Sokolov, and K. C. Hansen (2004), Three-dimensional, multispecies, high spatial resolution mhd studies of the solar wind interaction with mars, *Journal of Geophysical Research: Space Physics (1978–2012)*, *109*(A7).

Marconi, M. L., and D. A. Mendis (1983), The atmosphere of a dirty-clathrate cometary nucleus - A two-phase, multifluid model, *ApJ*, *273*, 381–396, doi: 10.1086/161377.

Marconi, M. L., L. Dagum, and W. H. Smyth (1996), Hybrid Fluid/Kinetic Approach to Planetary Atmospheres: an Example of an Intermediate-Mass Body, *ApJ*, *469*, 393, doi: 10.1086/177789.

Marschall, R., et al. (2016), Modelling observations of the inner gas and dust coma of comet 67P/Churyumov-Gerasimenko using ROSINA/COPS and OSIRIS data: First results, *A&A*, *589*, A90, doi: 10.1051/0004-6361/201628085.

Mukai, T., W. Miyake, T. Terasawa, M. Kitayama, and K. Hirao (1986), Plasma observation by Suisei of solar-wind interaction with comet Halley, *Nature*, *321*, 299–303, doi: 10.1038/321299a0.

Mukai, T., H. Fechtig, E. Grun, and R. H. Giese (1989), Icy particles from comets, *icarus*, *80*, 254–266, doi: 10.1016/0019-1035(89)90137-1.

Neubauer, F. M., et al. (1986), First results from the Giotto magnetometer experiment at comet Halley, *Nature*, *321*, 352–355, doi: 10.1038/321352a0.

Neugebauer, M., B. E. Goldstein, R. Goldstein, A. J. Lazarus, K. Altwegg, and H. Balsiger (1987), The pick-up of cometary protons by the solar wind, *A&A*, *187*, 21–24.

Neugebauer, M., et al. (2007), Encounter of the ulysses spacecraft with the ion tail of comet mcnaught, *The Astrophysical Journal*, *667*(2), 1262.

Omidi, N., and D. Winske (1991), Theory and simulation of cometary shocks, *Washington DC American Geophysical Union Geophysical Monograph Series*, *61*, 37–47.

Ootsubo, T., et al. (2012), Akari near-infrared spectroscopic survey for co2 in 18 comets, *The Astrophysical Journal*, *752*(1), 15.

Patashnick, H., and G. Rupprecht (1975), The size dependence of sublimation rates for interplanetary ice particles, *ApJ*, *197*, L79–L82, doi: 10.1086/181783.

Powell, K. G., P. L. Roe, T. J. Linde, T. I. Gombosi, and D. L. De Zeeuw (1999), A Solution-Adaptive Upwind Scheme for Ideal Magnetohydrodynamics, *Journal of Computational Physics*, *154*, 284–309, doi: 10.1006/jcph.1999.6299.

Rotundi, A., et al. (2015), Dust measurements in the coma of comet 67P/Churyumov-Gerasimenko inbound to the Sun, *Science*, *347*(1), aaa3905, doi: 10.1126/science.aaa3905.

Rubin, M., K. C. Hansen, T. I. Gombosi, M. R. Combi, K. Altwegg, and H. Balsiger (2009), Ion composition and chemistry in the coma of comet 1p/halley:a comparison between giotto's ion mass spectrometer and our ion-chemical network, *Icarus*, *199*(2), 505–519.

Rubin, M., et al. (2014a), Comet 1P/Halley Multifluid MHD Model for the Giotto Fly-by, *ApJ*, *781*, 86, doi: 10.1088/0004-637X/781/2/86.

Rubin, M., et al. (2014b), Plasma environment of a weak comet - Predictions for Comet 67P/Churyumov-Gerasimenko from multifluid-MHD and Hybrid models, *icarus*, *242*, 38–49, doi: 10.1016/j.icarus.2014.07.021.

Russo, N. D., R. Vervack Jr, H. Weaver, H. Kawakita, H. Kobayashi, N. Biver, D. Bockelée-Morvan, and J. Crovisier (2009), The parent volatile composition of 6p/d'arrest and a chemical comparison of jupiter-family comets measured at infrared wavelengths, *The Astrophysical Journal*, *703*(1), 187.

Schunk, R., and A. Nagy (2009), *Ionospheres: Physics, Plasma Physics, and Chemistry*, 2 ed., Cambridge University Press, Cambridge, doi: 10.1017/CBO9780511635342.

Schwamb, M. E. (2014), Solar System: Stranded in no-man's-land, *Nature*, *507*, 435–436, doi: 10.1038/507435a.

Shimizu, M. (1976), The structure of cometary atmospheres. I - Temperature distribution, *Ap&SS*, *40*, 149–155, doi: 10.1007/BF00651195.

Shou, Y., M. Combi, Y.-D. Jia, T. Gombosi, G. Toth, and M. Rubin (2015), The Plasma Environment in Comets over a Wide Range of Heliocentric Distances: Application to Comet C/2006 P1 (McNaught), *ApJ*, *809*, 156, doi: 10.1088/0004-637X/809/2/156.

Shou, Y., et al. (2016), A New 3D Multi-fluid Model: A Study of Kinetic Effects and Variations of Physical Conditions in the Cometary Coma, *ApJ*, *833*, 160, doi: 10.3847/1538-4357/833/2/160.

Smith, E. J., B. T. Tsurutani, J. A. Slavin, D. E. Jones, G. L. Siscoe, and D. A. Mendis (1986), International Cometary Explorer encounter with Giacobini-Zinner - Magnetic field observations, *Science*, *232*, 382–385, doi: 10.1126/science.232.4748.382.

Szegö, K., et al. (2000), Physics of Mass Loaded Plasmas, *Space Sci. Rev.*, *94*, 429–671.

Tenishev, V., M. Combi, and B. Davidsson (2008), A Global Kinetic Model for Cometary Comae: The Evolution of the Coma of the Rosetta Target Comet Churyumov-Gerasimenko throughout the Mission, *ApJ*, *685*, 659-677, doi: 10.1086/590376.

Tenishev, V., M. R. Combi, and M. Rubin (2011), Numerical Simulation of Dust in a Cometary Coma: Application to Comet 67P/Churyumov-Gerasimenko, *ApJ*, *732*, 104, doi: 10.1088/0004-637X/732/2/104.

Tóth, G. (1996), A General Code for Modeling MHD Flows on Parallel Computers: Versatile Advection Code, *Astrophysical Letters and Communications*, *34*, 245.

Tóth, G., et al. (2005), Space Weather Modeling Framework: A new tool for the space science community, *Journal of Geophysical Research (Space Physics)*, *110*, A12226, doi: 10.1029/2005JA011126.

Tóth, G., et al. (2012), Adaptive numerical algorithms in space weather modeling, *Journal of Computational Physics*, *231*, 870–903, doi: 10.1016/j.jcp.2011.02.006.

Tseng, W.-L., D. Bockelée-Morvan, J. Crovisier, P. Colom, and W.-H. Ip (2007), Cometary water expansion velocity from OH line shapes, *A&A*, *467*, 729–735, doi: 10.1051/0004-6361:20066666.

Wallis, M. K., and M. Dryer (1976), Sun and comets as sources in an external flow, *ApJ*, *205*, 895–899, doi: 10.1086/154345.

Weigert, A. (1959), Halo production in Comet 1925 II, *Astronomische Nachrichten*, *285*, 117–128, doi: 10.1002/asna.19592850304.

Whipple, F. L. (1950), A comet model. I. The acceleration of Comet Encke, *ApJ*, *111*, 375–394, doi: 10.1086/145272.